

# **Examination of the radionuclide inventory and chemical interactions on the interface between nuclear fuel and Zircaloy-4 cladding in irradiated LWR-fuel samples**

Zur Erlangung des akademischen Grades eines

DOKTORS DER NATURWISSENSCHAFTEN

(Dr. rer. nat.)

von der KIT-Fakultät für Chemie und Biowissenschaften  
des Karlsruher Instituts für Technologie (KIT)

genehmigte

DISSERTATION

von

M. Sc. Tobias König

aus

Achern, Deutschland

KIT-Dekan:	Prof. Dr. Hans-Achim Wagenknecht
Referent:	Prof. Dr. Horst Geckeis
Korreferent:	Prof. Dr. Petra Panak
Tag der mündlichen Prüfung:	26.04.2022



## Statement of originality / Erklärung

Hiermit versichere ich, dass die vorliegende Arbeit selbstständig angefertigt und keine anderen Hilfsmittel sowie Quellen als die angegebenen verwendet wurden. Des Weiteren versichere ich, dass alle Stellen der vorliegenden Arbeit, welche wörtlich oder inhaltlich aus anderen Quellen übernommen wurden als eben solche kenntlich gemacht sind und die Regeln zur Sicherung guter wissenschaftlicher Praxis am Karlsruher Institut für Technologie (KIT) in der jeweils gültigen Fassung beachtet wurden. Darüber hinaus versichere ich, dass die Arbeit in ähnlicher oder gleicher Form noch keiner Prüfungskommission vorgelegt wurde.

Eggenstein-Leopoldshafen, 07.03.2022

.....

(place and date / Ort und Datum)

.....

(signature / Unterschrift)



## Acknowledgements / Danksagung

Zunächst gilt mein Dank Herrn Prof. Dr. Horst Geckeis für die Bereitstellung dieses interessanten und auch gesellschaftlich viel diskutierten Themengebiets der Zwischen- und Endlagerung von hochradioaktiven Materialien, der wissenschaftlichen Betreuung und den fachlichen Diskussionen innerhalb der Thematik der nuklearen Entsorgung. Vielen Dank, dass ich diese Arbeit hier am Institut für Nukleare Entsorgung (INE) des Karlsruher Instituts für Technologie (KIT) habe anfertigen dürfen.

Besonderer Dank gilt auch Dr. Michel Herm, Dr. Volker Metz (beide KIT-INE) und Dr. Ernesto González-Robles Corrales (Fundació d'Investigació Sanitària Illes Balears (IdISBa), ehemals KIT-INE) für die stetige Hilfsbereitschaft, exzellente Betreuung und wissenschaftliche Einführung in die einzelnen Teilaspekte der Handhabung, Radiochemie und Entsorgung von abgebrannten Kernbrennstoffen. Mit ihrer langjährigen Expertise und außerordentlichen Fachwissen im Bereich hochradioaktiver Abfälle und deren Entsorgung haben sie wesentlich zum Erfolg der vorliegenden Arbeit beigetragen.

Des Weiteren möchte ich an dieser Stelle Herrn Arndt Walschburger (KIT-INE) danken, durch dessen eiserne Geduld, exzellentes Training und beispiellose Hilfsbereitschaft an den Manipulatoren und Infrastruktur der heißen Zellen ein erfolgreiches Gelingen dieser Arbeit nicht möglich gewesen wäre – Arndt, dir hierfür ein ewiges Dankeschön.

Darüber hinaus möchte ich mich bei Frau Elke Bohnert für ihre Hilfsbereitschaft, technische Expertise und die Spaltgasmessungen bedanken. Ich bedanke mich bei Dr. Dieter Schild und Frau Eva Soballa für unzählige SEM-EDS / -WDS und XPS Messungen an Zircaloy Proben, sowie Prof. Dr. Ron Dagan für die exzellenten Berechnungen mittels MCNP / CINDER und webKORIGEN (alle KIT-INE).

Dr. Kathy Dardenne, Dr. Jörg Rothe, Dr. Tim Prüßmann und Dr. Nicolas Finck möchte ich für die Einführung und die Unterstützung bei XAS Messungen danken (alle KIT-INE).

Außerdem möchte ich mich bei Herrn Volker Krepper und Herrn Stefan Schmitt (beide KIT-INE) für die unschätzbare Hilfe bei der Konstruktion von Versuchsgefäßen und der Instandhaltung der heißen Zellen bedanken.

Ebenso bedanken möchte ich mich bei Frau Annika Fried, Frau Cornelia Walschburger, Frau Elvira Rolgejzer und Herrn Frank Geyer für unzählige ICP-MS Messungen, sowie Frau Stefanie Kuschel für ebenso unzählige IC Messungen. Mein weiterer Dank gilt Frau Melanie Böttle und Herrn Markus Fuss für LSC- und  $\gamma$ -Messungen (alle KIT-INE).

Herr Gerhard Christill, Frau Ilonca Bachmann und Herr Thorsten Hoffmann (alle KIT-SUM) möchte ich danken für ihre Unterstützung bei der Durchführung dieser Arbeit im Rahmen von Strahlenschutzaktivitäten.

Dr. Nese Çevirim-Papaioannou, Dr. Pelin Çakir-Wuttke und Herrn Bernd Bummel (alle KIT-INE) möchte ich herzlich für die vielen, kleinen Raucherpausen danken.

Darüber hinaus möchte ich mich auch bei Herrn Dr. Dimitrios Papaioannou (JRC-Karlsruhe) für wissenschaftliche Denkanstöße zum Thema abgebrannter Kernbrennstoff und Hüllrohrintegrität, sowie Herrn Dr. Tim Platte und Herrn Daniel Glückman (beide KIT-INE) für das Korrekturlesen der vorliegenden Arbeit, bedanken.

Ebenso bedanken möchte ich mich bei Frau Dr. Sarah Duckworth (KIT-INE) für ihren ständigen Beistand, ihre endlose Liebe und Geduld während des Anfertigens dieser Arbeit.

Zuletzt möchte ich meinen Eltern und meinen Schwestern danken die immer für mich da waren.

## Abstract

In several countries utilising nuclear power plants as energy source, e.g. Finland, Germany and Sweden, the concept of direct geological disposal of spent nuclear fuel (SNF) is considered. This suggests to store SNF after discharge from the nuclear reactor for few years under water in reactor-site storing pools until transfer out of the reactor building to an interim storage facility. In case of dry interim storage, the irradiated fuel assemblies are emplaced in multi-purpose transport and storage casks, such as the CASTOR<sup>®</sup> of Gesellschaft für Nuklear-Service. Eventually, the SNF is transferred to a deep geological repository. For instance in Germany, Spain and the United States of America, multi-purpose casks with SNF are stored in dry interim storage facilities, mostly located in close vicinity to the nuclear power plants, where the SNF was discharged from. It is foreseen to keep the SNF in transport and storage casks until a final repository for high-level waste (HLW) will be in operation. Begin of operation of final repositories for HLW are expected in the next years (Finland and Sweden), respectively decades (e.g. Switzerland and other European countries). Since transport and storage casks are not licensed for final disposal, the SNF needs to be transferred into a suitable final disposal container. The integrity of the fuel claddings during the transfer from transport and storage casks to final disposal containers is of utter importance, to ensure that radionuclides (RN) will not be released by failure of the cladding tube.

Already during reactor operation, the Zircaloy cladding tubes undergo different processes, such as transient elongation of the fuel rod, oxidation of the fuel- and the water-faced sides, formation of zirconium hydrides, as well as mechanical stress, which correlates with the fuel pellet swelling at higher burn-ups.

Furthermore, in case of long-term safety analyses for final repositories, the contact of groundwater with the stored nuclear waste is considered. Depending on the classification of the national waste management organisations of the individual countries, at this, the cladding tube is considered as a technical barrier whose failure leads to a release of radionuclides, in particular activation products from the cladding as well as RNs from the

fuel following the water penetration through the breached cladding to the SNF. In this context, various activation and fission products, such as, for example C-14, Cl-36, Cs-135 and I-129 are of significant interest due to their long half-lives, expected rapid release from the waste and high mobility in a repository system.

This Ph.D. thesis addresses the occurrence of the beta and gamma radiation-emitting radionuclides Cl-36, Cs-137 and I-129, which are segregated to some extent from the fuel to the pellet-cladding interface during reactor operation. As part of these investigations, the inventory of radionuclides at the interface, respectively the inventory of the irradiated fuel and the Zircaloy cladding tube will be determined experimentally and compared to activation calculations obtained by Monte Carlo N-particle code and CINDER as well as webKORIGEN calculations. For the precise identification of the Cl-36 and I-129 inventory, it is necessary to develop a radiochemical separation process, which allows a quantitative analysis of both of the nuclides. Since Cl-36 has no and I-129 very low energy gamma-lines, an experimental inventory determination is only possible by a complex separation of these two isotopes from other radionuclides. The method developed in this work allows the profound separation and quantification of Cl-36 and I-129 from other interfering radionuclides, present in excess by many orders of magnitude in highly radioactive specimens, by using various extraction and precipitation steps. The results presented in this work provide information on the actual proportion of Cl-36 generated by neutron activation in highly radioactive waste, as well as on the amount of the initial Cl-35 impurity. Furthermore, it is shown, that I-129 is transported by a temperature driven process from the hot pellet centre to the peripheral area, adjacent to the colder cladding, resulting in the enrichment of the volatile radionuclide. In addition to the determination of Cl-36 and I-129 activities, other radionuclides (i.e. transuranium isotopes, fission and activation products) in the highly radioactive samples were determined and quantified with respect to enrichment factors in e.g. the fuel-cladding interaction layer in the spent nuclear fuel. The experimental radionuclide measurements performed within this thesis are in good agreement with values derived from calculations and are providing further knowledge on the distribution of radionuclides in spent nuclear

fuel and thus also to the more accurate determination of the source term for irradiated fuel.

In the second part of the thesis, different spectroscopic methods like scanning electron microscopy and energy / wavelength dispersive X-ray spectroscopy (SEM-EDS / -WDS) as well as X-ray photoelectron spectroscopy (XPS) and X-ray absorption spectroscopy (XAS) are used for the analysis of the fuel-cladding interface. Here, examinations of the occurrence of caesium / chlorine / iodine containing phases within the fuel-cladding interaction layer of different irradiated fuel-types ( $\text{UO}_x$  and mixed oxide fuel (MOX)) as well as different burn-ups (50.4  $\text{GWd/t}_{\text{HM}}$  and 38.0  $\text{GWd/t}_{\text{HM}}$ ) are performed. It is evident, that the chemistry at the interface is far more complex than often reported in the past literature, such as solely the occurrence of CsI,  $\text{UO}_2$  or a mixed compound of zirconium and uranium ( $(\text{Zr, U})\text{O}_{2-x}$ ). To the knowledge of the author, it is the first time that synchrotron radiation based Cl and I K-edge measurements are performed on actual spent nuclear fuel fragments and Zircaloy cladding segments, resulting in an iodine-bearing compound with structural similarity to CsI and a yet to be identified chlorine-bearing compound. These measurements aim to provide a better understanding on the occurrence of iodine and chlorine-bearing agglomerates in spent nuclear fuel.

The last part of the thesis focusses on possible corrosive effects of fission and activation product agglomerates on the interface layer, impacting the cladding integrity of spent nuclear fuel rods with regard to a prolonged dry interim storage. Hereto, U-O-Zr-Cs-Cl-I-containing phases are deposited on unirradiated Zircaloy and stored under inert gas and elevated temperature for an extended period of time. Afterwards the resulting samples are analysed by SEM-EDS and XPS to draw conclusions on their corrosion and embrittlement behaviour. Results obtained from this experiment indicate pitting corrosion processes on the Zircaloy cladding under the above mentioned conditions, enabled by the halogen-bearing species. Especially the role of the impurity chlorine in nuclear fuel and cladding material is highlighted by this experiment as its effects on possible cladding degradation under interim storage conditions is till now afflicted with uncertainties. However, it is evident, that more experiments are needed to elucidate this effect. The

applied experimental conditions are not fully representative for the interim storage environment. The effect of radiation is not considered and a significant oxidation of the introduced  $\text{UO}_2$  was found unexpectedly, despite working under Ar atmosphere.

The work of this thesis is performed in part within the EURAD work package “Spent fuel characterization and evolution until disposal”.

## Kurzfassung

Neben Deutschland, verfolgen auch weitere Länder wie Finnland oder Schweden, welche Kernenergie zur Stromerzeugung nutzen, für ausgediente Brennelemente (BE) das Konzept der direkten Endlagerung. Dieses sieht vor, dass BE nach dem Entladen aus dem Kernreaktor zunächst für einige Jahre unter Wasser in reaktornahen Brennelementlagerbecken gelagert werden, bevor sie zur weiteren Zwischenlagerung in einen Transport- und Lagerbehälter (TLB), wie beispielsweise dem CASTOR<sup>®</sup> der Gesellschaft für Nuklear-Service überführt und in einer Einrichtung zur Zwischenlagerung eingelagert werden. Schließlich sollen die BE in ein tiefengeologisches Endlager verbracht werden. So werden beispielsweise in Deutschland, Spanien und den Vereinigten Staaten von Amerika die TLB mit ausgedienten BE in Zwischenlagern in der Nähe der Kernkraftwerke aufbewahrt, aus denen der Kernbrennstoff aus dem Reaktor entladen wurde. Während einer solchen trockenen Zwischenlagerung verbleiben die BE in den TLB bis zur Bereitstellung eines Endlagers für hochradioaktive Abfälle. Der Beginn des Einlagerungsbetriebs hochradioaktiver Abfälle ist in den nächsten Jahren (Finnland und Schweden) beziehungsweise Jahrzehnten (z.B. Schweiz und weitere europäische Staaten) geplant. Da der TLB nicht zur Endlagerung zugelassen ist, müssen die BE dann in einen geeigneten Endlagerbehälter überführt werden. Die Integrität der Brennstabhüllrohre bei der Umladung vom TLB zum Endlagerbehälter ist entscheidend, da sonst bei einem Versagen des Hüllrohres, Radionuklide freigesetzt werden könnten.

Bereits während des Reaktorbetriebes werden die Zircaloy-Hüllrohre durch verschiedene Prozesse, wie z.B. transients Längung der Brennstäbe, Oxidation auf der Brennstoff- und Wasserseite, Bildung von Zirkonium-Hydriden und mechanischer Belastung, welche das mit zunehmenden Abbrand anschwellende Brennstoffpellet auf das Hüllrohr ausübt, beeinträchtigt.

Weiterhin, wird im Rahmen von Langzeitsicherheitsuntersuchungen für Endlager von radioaktiven Abfällen der Kontakt von Grundwässern mit den eingelagerten Abfällen

betrachtet. Je nach Klassifikation der nuklearen Entsorgungsorganisationen der einzelnen Staaten, bildet das Hüllrohr hierbei einen Teil der technischen Barriere, dessen Versagen zu einer Freisetzung von Radionukliden führt, d.h. zur Freisetzung von Aktivierungsprodukten aus dem Hüllrohr, sowie zur Radionuklidfreisetzung aus dem Kernbrennstoff infolge des Durchdringens von Wasser durch das Hüllrohr zum Brennstoff. In diesem Kontext sind verschiedene Spalt- und Aktivierungsprodukte wie unter anderem C-14, Cl-36, Cs-135 und I-129 aufgrund langer Halbwertszeiten, der erwarteten schnellen Freisetzung aus dem Abfall und erhöhten Mobilität im Endlagersystem von großem Interesse.

Die vorliegende Doktorarbeit befasst sich mit dem Verhalten beta- und gammastrahlender Nuklide wie Cl-36, Cs-137 und I-129, welche sich während des Reaktorbetriebes aus dem Kernbrennstoff an die Kernbrennstoffpellet-Hüllrohr-Grenzfläche abscheiden. Im Zuge von Untersuchungen wird zunächst das Inventar der Radionuklide an diesen Grenzflächen bzw. im Kernbrennstoff und Zircaloy-Hüllrohr experimentell bestimmt und mit Daten aus Monte Carlo N-particle Code und CINDER sowie webKORIGEN Berechnungen verglichen. Zur exakten experimentellen Bestimmung des Cl-36- und I-129-Inventars ist es nötig, einen radiochemischen Trennungsgang für hochradioaktive Proben zu entwickeln, der eine quantitative Analyse der beiden Nuklide erlaubt. Da Cl-36 keine und I-129 nur sehr niederenergetische, charakteristische Gammalinien besitzen, ist eine experimentelle Inventarbestimmung nur durch eine vorherige aufwendige Separation dieser beiden Isotopen von allen anderen Radionukliden möglich. Die Methode, welche in dieser Arbeit entwickelt wurde erlaubt die fundierte Abtrennung und Quantifizierung von Cl-36 und I-129 mittels verschiedenen Extraktions- und Fällungsschritten von anderen Radionukliden, welche sich in Überschüssen von mehreren Größenordnungen in hoch radioaktiven Proben befinden. Die in der Arbeit präsentierten Ergebnisse liefern Informationen zu der tatsächlich gebildeten Quantität an Cl-36, welches durch Neutronenaktivierung in hoch radioaktiven Abfällen generiert wurde, und darüber hinaus, werden Aussagen über die Menge der Cl-35 Verunreinigung getroffen. Des Weiteren wird gezeigt, dass I-129 über einen Temperatur-getriebenen Prozess vom heißen Pellet-

Zentrum zu der Randregion, welche in Kontakt mit dem kälteren Hüllrohr steht, transportiert wird, was zu einer Anreicherung des flüchtigen Radionuklids dort führt. Zusätzlich zur Bestimmung von  $^{136}\text{Cl}$  und  $^{129}\text{I}$  Aktivitäten, wurden weitere Radionuklide (Transurane, Spalt- und Aktivierungsprodukte) in den hoch radioaktiven Proben, in Hinblick auf Anreicherungsfaktoren wie beispielsweise in der Wechselwirkungsschicht zwischen Kernbrennstoff und Hüllrohr in abgebranntem Kernbrennstoff, bestimmt und quantifiziert. Die in dieser Arbeit durchgeführten, experimentellen Radionuklidmessungen befinden sich in Einklang mit Werten, welche aus Berechnungen erhalten wurden und tragen zu einem erweiterten Kenntnisstand der Verteilung von Radionukliden in abgebranntem Kernbrennstoff bei und somit auch zur genaueren Bestimmung des Quellterms für bestrahlten Kernbrennstoff.

Im zweiten Teil der Doktorarbeit werden verschiedene spektroskopische Methoden, wie Rasterelektronenmikroskopie, gekoppelt mit energiedispersiver bzw. wellenlängendispersiver Röntgenspektroskopie (REM-EDS / -WDS), Röntgenphotoelektronenspektroskopie (XPS), sowie Röntgenabsorptionsspektroskopie (XAS) zur Analyse der Kernbrennstoff-Hüllrohr-Grenzflächen eingesetzt. Hierbei wird die chemische Zusammensetzung von Cäsium / Chlor / Iod haltigen Phasen innerhalb der Kernbrennstoff-Hüllrohr-Wechselwirkungsschicht in verschiedenen bestrahlten Brennstoffarten ( $\text{UO}_x$ - und Mischoxidbrennstoff (MOX)), sowie bei verschiedenen Abbränden ( $50,4 \text{ GWd/t}_{\text{HM}}$  und  $38,0 \text{ GWd/t}_{\text{HM}}$ ) näher untersucht. Es ist offensichtlich, dass die Chemie der Wechselwirkungsschicht weitaus komplizierter ist als oftmals in vergangener Literatur berichtet, z.B. nur das Vorhandensein von CsI,  $\text{UO}_2$  oder einer Mischverbindung aus Zirkonium und Uran ( $(\text{Zr}, \text{U})\text{O}_{2-x}$ ). Nach Kenntnisstand des Autors, ist es das erste Mal, dass Synchrotronstrahlungs-basierte Cl und I K-Kanten Messungen an abgebrannten Kernbrennstofffragmenten und Hüllrohrsegmenten durchgeführt werden, welche in Iod-haltigen Verbindungen mit struktureller Ähnlichkeit zu CsI und einer bis dato zu identifizierenden Chlor-haltigen Verbindung resultieren. Diese Messungen haben das Ziel, zu einem besseren Verständnis des Vorkommens von Iod- und Chlor-haltigen Agglomeraten in abgebranntem Kernbrennstoff beizutragen.

Der letzte Teil der Arbeit behandelt mögliche, korrosive Auswirkungen von Spalt- und Aktivierungsproduktablagerungen an den Grenzflächen von Hüllrohren und deren Effekt die Integrität von Hüllrohren bestrahlter Brennstäbe im Hinblick auf eine verlängerte, trockene Zwischenlagerung. Hierzu werden U-O-Zr-Cs-Cl-I-haltige Phasen auf unbestrahltes Zircaloy aufgebracht und für einen längeren Zeitraum unter zwischenlagerrelevanten Bedingungen, Inertgas und erhöhter Temperatur aufbewahrt. Im Anschluss daran werden die erhaltenen Proben mittels REM-EDS und XPS analysiert, um Rückschlüsse auf deren Korrosions- und Versprödungsverhalten zu erhalten. Die Ergebnisse, welche aus diesem Experiment erhalten wurden, deuten auf Lochfraßkorrosions-Prozesse des Zircaloy-Hüllrohrs, ausgelöst durch die Halogenhaltigen Spezies, unter oben genannten Bedingungen hin. Insbesondere wird das Verhalten der Verunreinigung Chlor in Kernbrennstoff und Hüllrohrmaterialien durch dieses Experiment hervorgehoben, da sein Effekt auf eine mögliche Degradation von Hüllrohren unter Zwischenlagerungsbedingungen noch immer mit Unsicherheiten verbunden ist. Allerdings sind weitere Untersuchungen zur Bestätigung dieses Befunds notwendig. Die experimentellen Bedingungen sind nur eingeschränkt repräsentativ für die Zwischenlagerung. Der Einfluss von Strahlung wird nicht betrachtet und trotz des Arbeitens unter Ar Atmosphäre wurde eine unerwartet deutliche Oxidation des eingesetzten  $UO_2$  beobachtet.

Ein Teil der Arbeiten dieser Dissertation stellen einen Beitrag zum EURAD Arbeitspaket „Spent fuel characterization and evolution until disposal“ dar.

# Table of contents

1	Introduction .....	- 1 -
1.1	Background .....	- 1 -
1.2	Objectives of this work.....	- 5 -
2	SNF in context of storage and disposal .....	- 7 -
2.1	Composition of spent nuclear fuel.....	- 8 -
2.1.1	Long-lived fission and activation products .....	- 10 -
2.1.2	Behaviour of spent nuclear fuel under conditions of a deep geological repository.....	- 12 -
2.2	Cladding material of LWR nuclear fuel rods .....	- 14 -
2.3	Interim storage of SNF .....	- 17 -
2.4	Physical embrittlement processes during reactor operation and storage.....	- 20 -
2.5	Chemical degradation phenomena during reactor operation and storage .....	- 21 -
2.6	Pellet-cladding interactions .....	- 23 -
3	Chlorine-36 and iodine-129.....	- 26 -
3.1	Chlorine-36.....	- 26 -
3.2	Iodine-129 .....	- 29 -
3.3	Cl-36 and I-129 in terms of repository safety aspects.....	- 30 -
4	Materials and methods.....	- 31 -
4.1	Chemicals and radionuclides used in this work .....	- 31 -
4.1.1	Chemicals .....	- 31 -
4.1.2	Cl-36 standardised solutions used for quench and recovery tests .....	- 33 -
4.1.3	I-129 standardised solutions used for quench and recovery tests.....	- 34 -

4.2	Spent fuel samples origin and treatment .....	- 35 -
4.2.1	UO <sub>x</sub> fuel .....	- 35 -
4.2.2	MOX fuel.....	- 37 -
4.2.3	Preparation of the irradiated fuel samples .....	- 38 -
4.2.4	Sampling of high active specimens for radionuclide inventory analysis in fuel, cladding and fuel-cladding interface layer.....	- 40 -
4.3	Digestion of the irradiated fuel samples.....	- 42 -
4.4	Radionuclide inventory determination and separation method for Cl-36 and I-129 .....	- 46 -
4.4.1	Experimental set-up of the Cl-36 and I-129 separation method.....	- 46 -
4.4.2	Determination of actinide, fission and activation product inventory ...	- 51 -
4.4.3	Analytical methods for spent nuclear fuel and cladding samples .....	- 52 -
4.4.3.1	Liquid Scintillation Counting (LSC) for Cl-36, I-129 and Sr-90 / Y-90 activity concentration in solution.....	- 52 -
4.4.3.2	$\gamma$ -spectrometric analysis for I-129, Co-60, Sb-125, Eu-154 / 155, Am-241 and Cs-134 / 137 activity concentration in solution.....	- 55 -
4.4.3.3	Inductively coupled plasma mass spectrometry (ICP-MS) for I-127 and actinide concentration in solution .....	- 56 -
4.4.3.4	Ion chromatography (IC) for total chlorine concentration.....	- 56 -
4.4.3.5	Gas mass spectrometry (gas-MS) for fission gas inventory and release during digestion process.....	- 57 -
4.5	Calculation of the radionuclide inventory and activation prediction of chlorine-35 in irradiated Zircaloy-4 and fuel.....	- 58 -
4.6	Microscopic examinations of the fuel-cladding interface .....	- 59 -

4.6.1	Sample preparation for spectroscopic analysis of fuel, cladding and fuel-cladding interaction layer .....	60 -
4.6.2	Scanning electron microscopy – energy / wavelength dispersive X-ray spectroscopy (SEM-EDS / -WDS).....	61 -
4.6.3	X-ray photoelectron spectroscopy (XPS).....	62 -
4.6.4	X-ray absorption spectroscopy (XAS) .....	62 -
4.6.4.1	Cl K-edge measurements .....	63 -
4.6.4.2	I K-edge measurements.....	64 -
4.7	Simulation of Zircaloy-SNF interactions .....	64 -
4.7.1	Experimental set-up for cladding corrosion experiment with non-irradiated Zircaloy-4 .....	65 -
4.7.2	Examination of non-irradiated Zircaloy-4 specimens .....	70 -
5	Results and Discussion .....	71 -
5.1	Determination of radionuclide inventory in SNF, cladding and fuel-cladding interaction layers .....	71 -
5.1.1	Recoveries of the separation method for Cl-36 and I-129 .....	72 -
5.1.2	Determination of Cl-36 and I-129 inventory in digestion liquors of high active specimens.....	74 -
5.1.3	Radionuclide inventory of Zircaloy-4 in contact with spent UO <sub>x</sub> or MOX fuel and comparison to calculated inventories .....	80 -
5.1.4	Radionuclide inventory of spent UO <sub>x</sub> and MOX fuel and comparison to calculated results .....	83 -
5.1.5	Conclusions regarding the RN inventory determination of high active waste specimens .....	93 -

5.2	Microscopic and spectroscopic investigations on irradiated UO <sub>x</sub> and MOX fuel and their respective fuel-cladding interfaces.....	- 96 -
5.2.1	XAS investigations on the interaction layer between fuel and cladding.....	- 96 -
5.2.2	SEM-EDS / -WDS analysis of UO <sub>x</sub> and MOX cladding specimens .-	103 -
5.2.3	XPS surveys on the surface of the interaction layer between fuel and cladding .....	- 110 -
5.2.4	Conclusions on microscopic examinations on the fuel-cladding interface and their impact on possible cladding integrity degradation.....	- 114 -
5.3	Experimental simulation of cladding corrosion .....	- 116 -
5.3.1	Optical examination of non-irradiated Zircaloy after termination of the corrosion experiment.....	- 116 -
5.3.2	XPS surface analyses of non-irradiated Zircaloy after termination of the corrosion experiment.....	- 119 -
5.3.3	SEM-EDS analysis of the non-irradiated Zircaloy after termination of the corrosion experiment.....	- 123 -
5.3.4	Conclusions from the experimental simulation of cladding corrosion-	127 -
6	Summary and conclusions.....	- 129 -
	Appendix .....	- 133 -
	References .....	- 140 -

## List of figures

<b>Figure 2.1:</b> Microstructure of SNF and distribution of actinides and fission products... .	- 10 -
<b>Figure 2.2:</b> Chemical processes which might affect the alteration of SNF upon contact with groundwater.....	- 14 -
<b>Figure 2.3:</b> Simplified structure of an interim storage facility.....	- 19 -
<b>Figure 4.1:</b> LSC spectrum of Cl-36 standard reference material.....	- 33 -
<b>Figure 4.2:</b> LSC spectrum of I-129 standard reference material.....	- 34 -
<b>Figure 4.3:</b> High burn-up UO <sub>x</sub> fuel rod segment N0204 of fuel rod SBS 1108. ....	- 36 -
<b>Figure 4.4:</b> MOX fuel rod segment of the fuel rod 5810. ....	- 38 -
<b>Figure 4.5:</b> Cutting and preparation process for the UO <sub>x</sub> specimen.....	- 39 -
<b>Figure 4.6:</b> Cutting and preparation process of the MOX fuel sample.. ....	- 40 -
<b>Figure 4.7:</b> Pictures and dimension of the UO <sub>x</sub> fuel segment used for inventory determination and spectroscopic analysis. ....	- 41 -
<b>Figure 4.8:</b> Defueling process of the high burn-up UO <sub>x</sub> fuel.....	- 41 -
<b>Figure 4.9:</b> Fragment selection and alkaline digestion process of the UO <sub>x</sub> fuel specimen.. ..	- 44 -
<b>Figure 4.10:</b> Fragment and material for gas phase analysis. ....	- 44 -
<b>Figure 4.11:</b> Experimental procedure of the Cl-36 and I-129 separation method.....	- 47 -

<b>Figure 4.12:</b> Phase separation of aqueous phase containing Cl-36 amongst other RN and iodine bearing organic phase. ....	- 49 -
<b>Figure 4.13:</b> Stripping of iodine from the organic phase back into aqueous phase...	- 49 -
<b>Figure 4.14:</b> Precipitation of caesium and filtration with a 0.45 $\mu\text{m}$ syringe filter...	- 50 -
<b>Figure 4.15:</b> Quench correction curve for Cl-36. ....	- 54 -
<b>Figure 4.16:</b> Sample holder designated for XAS measurements of SNF specimens.	- 61 -
<b>Figure 4.17:</b> Polished Zircaloy-4 surface of the platelets utilised in the cladding corrosion experiment. ....	- 65 -
<b>Figure 4.18:</b> Design and dimensions of the components for the cladding corrosion experiment. ....	- 66 -
<b>Figure 4.19:</b> Autoclave, tantalum liner and graphite sealing rings for the cladding corrosion experiment. ....	- 67 -
<b>Figure 4.20:</b> Experimental setup for the cladding corrosion experiment. ....	- 67 -
<b>Figure 4.21:</b> Interior of the high temperature oven used for the cladding corrosion experiment. ....	- 68 -
<b>Figure 5.1:</b> LSC spectra of recovery tests without a SNF or Zircaloy matrix showing a clean separation of I-129 (b)) and Cl-36 (c)) from the initial sample solution (a))....	- 73 -
<b>Figure 5.2:</b> Cl-36 inventory [ $\text{Bq}/t_{\text{HM}}$ ] of the digested fuel specimens with respect to the sampling region in the SNF pellet. ....	- 75 -
<b>Figure 5.3:</b> Recorded Cl-36 spectra of a) a Cl-36 standard solution and b) extracted Cl-36 from the Zry- $\text{UO}_x$ specimen.....	- 76 -

**Figure 5.4:** Experimentally derived Cl-36 inventories [Bq/t<sub>HM</sub>] of the Zircaloy specimens of the UO<sub>x</sub> and MOX fuel and values obtained by MCNP / CINDER calculations..- 77 -

**Figure 5.5:** I-129 inventory [Bq/t<sub>HM</sub>] in the rim area of the two SNF specimens in comparison to calculated results by means of MCNP calculations.....- 79 -

**Figure 5.6:** Co-60 and Sb-125 activation product inventory [Bq/t<sub>HM</sub>] in comparison to MCNP calculations and results for the plenum tube section.....- 80 -

**Figure 5.7:** Experimentally obtained actinide inventory [Bq/t<sub>HM</sub>] of the Zircaloy specimen previously in contact with the UO<sub>x</sub> fuel compared to MCNP calculations- 82 -

**Figure 5.8:** Actinide inventories [Bq/t<sub>HM</sub>] of the Zircaloy specimens in contact with the UO<sub>x</sub> and MOX fuel, as well as the actinide inventories of the plenum section.....- 83 -

**Figure 5.9:** Experimentally determined actinide inventories [Bq/t<sub>HM</sub>] for the rim and core region of the examined UO<sub>x</sub> fuel. ....- 84 -

**Figure 5.10:** Comparison of selected actinide inventories [Bq/t<sub>HM</sub>] determined experimentally and MCNP calculations performed for distinct regions in the SNF pellet. ....- 85 -

**Figure 5.11:** Comparison of experimentally determined inventory [Bq/t<sub>HM</sub>] of selected fission products in distinct regions of the fuel pellet to MCNP calculations. ....- 86 -

**Figure 5.12:** Actinide inventory [Bq/t<sub>HM</sub>] of a core and rim sample of the MOX fuel specimen. ....- 88 -

**Figure 5.13:** Comparison of experimental MOX actinide inventories [Bq/t<sub>HM</sub>] to KORIGEN calculations. ....- 89 -

**Figure 5.14:** Selected fission product inventories [Bq/t<sub>HM</sub>] of the MOX fuel specimen and comparison to KORIGEN calculations.....- 90 -

**Figure 5.15:** Actinide inventories [Bq/t<sub>HM</sub>] of the UO<sub>x</sub> and MOX fuel rim specimens compared to each other.....- 91 -

**Figure 5.16:** Comparison of actinide inventory [Bq/t<sub>HM</sub>] of the fuel rod segment N0204 and the sister fuel rod segment N0203. ....- 92 -

**Figure 5.17:** Comparison of the actinide inventory [Bq/t<sub>HM</sub>] of the examined MOX fuel rod segment with a burn-up of 38.0 GWd/t<sub>HM</sub> and a MOX fuel rod segment irradiated to a burn-up of 39.6 GWd/t<sub>HM</sub>.....- 93 -

**Figure 5.18:** Cl K-edge XANES spectra for a fuel fragment from the previously closed gap, a Zircaloy cladding segment with fuel residue and an unirradiated Zircaloy-4 specimen. ....- 97 -

**Figure 5.19:** Cl K-edge XANES of the fuel fragment in comparison to a CsCl reference. ....- 98 -

**Figure 5.20:** Cl K-edge XANES spectra with Y-offset.....- 99 -

**Figure 5.21:** Cl K-edge XANES spectra of a MOX fuel fragment in comparison to the UO<sub>x</sub> fuel fragment.....- 100 -

**Figure 5.22:** Cl K-edge XANES spectra of both Zircaloy claddings previously in contact with the respective fuel type.....- 100 -

**Figure 5.23:** I K-edge XANES of a MOX fuel fragment and cladding specimen compared to a CsI reference spectrum. ....- 101 -

<b>Figure 5.24:</b> K-edge XANES spectra of different iodine species measured and published by Reed and colleagues [REED <i>ET AL.</i> , 2002].	- 102 -
<b>Figure 5.25:</b> I K-edge XANES spectra of the CsI reference and fuel fragments for UO <sub>x</sub> and MOX SNF in comparison to each other.	- 103 -
<b>Figure 5.26:</b> SEM-EDS analysis of crystalline precipitates on irradiated Zircaloy cladding in contact with spent UO <sub>x</sub> fuel.	- 104 -
<b>Figure 5.27:</b> EDS analysis and SEM pictures of the interaction layer upon the Zircaloy surface for the MOX cladding specimen.	- 105 -
<b>Figure 5.28:</b> Zircaloy surface and residual layer on the alkaline defueled high burn-up UO <sub>x</sub> fuel.	- 106 -
<b>Figure 5.29:</b> Elemental mapping of the alkaline defueled high burn-up UO <sub>x</sub> fuel Zircaloy with a magnification of 250 μm.	- 107 -
<b>Figure 5.30:</b> Deposit of chlorine and iodine bearing crystalline compound on defueled Zircaloy layer indicated by red circle.	- 108 -
<b>Figure 5.31:</b> Epsilon particle agglomerate on the interaction layer of the defueled Zircaloy surface.	- 109 -
<b>Figure 5.32:</b> Recorded WDS spectrum in comparison to the EDS spectrum.	- 110 -
<b>Figure 5.33:</b> XPS spectrum of fuel layer on Zircaloy previously in contact with UO <sub>x</sub> fuel cladding.	- 111 -
<b>Figure 5.34:</b> Examined surface area analysed by XPS on Zircaloy segment previously in contact with MOX fuel.	- 112 -

<b>Figure 5.35:</b> XPS survey spectrum of Zircaloy surface previously in contact with spent MOX fuel.....	- 112 -
<b>Figure 5.36:</b> Narrow scans for the Cl 2p elemental lines for chlorine in the interaction layer upon the Zircaloy for the UO <sub>x</sub> and MOX fuel. ....	- 113 -
<b>Figure 5.37:</b> Narrow scans for the U 4f and Cd 3d elemental lines in the interaction layer upon the Zircaloy for the MOX fuel.....	- 114 -
<b>Figure 5.38:</b> Comparison by optical examination of Zircaloy platelets before and after termination of the corrosion experiment. ....	- 117 -
<b>Figure 5.39:</b> Optical examination of the utilised Zircaloy platelets after the corrosion experiment. ....	- 118 -
<b>Figure 5.40:</b> Recorded XPS spectra of all four Zircaloy platelets after termination of the experiment. ....	- 119 -
<b>Figure 5.41:</b> Narrow scans of uranium 4f orbitals in order to determine the uranium oxidation state in the Zircaloy specimens.....	- 120 -
<b>Figure 5.42:</b> Iodine 3d narrow scans. ....	- 121 -
<b>Figure 5.43:</b> XPS analysis of a halogen rich agglomerate on the Zircaloy surface.-	- 122 -
<b>Figure 5.44:</b> SEM picture taken in secondary electron mode and EDS analysis of the blank specimen. ....	- 123 -
<b>Figure 5.45:</b> UO <sub>2</sub> deposits on the zirconia surface observable in all specimens.....	- 124 -
<b>Figure 5.46:</b> SEM picture taken in backscatter electron mode of the area on the Zircaloy specimen in contact with CsCl and UO <sub>2</sub> , indicating a pitting corrosion process on the zirconia layer. ....	- 125 -

<b>Figure 5.47:</b> Crystals on the surface layer rich in iodine and uranium of the specimen previously in contact with CsI and UO <sub>2</sub> . .....	- 126 -
<b>Figure B.1:</b> I K-edge XANES spectra of the examined specimens.....	- 137 -
<b>Figure B.2:</b> Recorded Cl K-edge XANES spectra. ....	- 138 -

## List of tables

<b>Table 2.1:</b> Half-lives, type of decay and thermal fission yield of LLFP. ....	- 11 -
<b>Table 2.2:</b> Main alloying elements and impurities in Zry-2 and Zry-4 in weight %. -	16 -
<b>Table 4.1:</b> Chemicals used in this work.....	- 32 -
<b>Table 4.2:</b> Characteristics and irradiation data of the UO <sub>x</sub> fuel rod SBS1108.....	- 36 -
<b>Table 4.3:</b> Characteristics and irradiation data of the MOX fuel rod 5810. ....	- 37 -
<b>Table 4.4:</b> Masses, dose rate and initial location within the SNF specimen of the samples used for inventory analysis. ....	- 45 -
<b>Table 4.5:</b> Deposited fission and activation product salt mixtures simulating components at the Zircaloy-UO <sub>2</sub> interface. ....	- 68 -
<b>Table 4.6:</b> Time intervals and temperature during the experiment.....	- 69 -
<b>Table 5.1:</b> Selected recovery tests performed as double determinations in order to monitor the extraction yield of the separation technique. ....	- 73 -
<b>Table 5.2:</b> Experimental Cl-36 inventories [Bq/t <sub>HM</sub> ] of the examined fuel types with respect to the sampling region in the SNF pellet.....	- 75 -

**Table 5.3:** Experimentally obtained Cl-36 inventories [Bq/t<sub>HM</sub>] in the Zircaloy specimens compared to results derived from MCNP calculations for 15 ppm initial Cl-35 impurity. .... - 78 -

**Table 5.4:** I-129 inventories [Bq/t<sub>HM</sub>] of the examined rim area fragments of both SNF types and MCNP calculations for distinct regions within the fuel pellet. .... - 79 -

**Table 5.5:** Fission gas inventory in mol/g<sub>UO<sub>2</sub></sub> for an alkaline digested fuel fragment of the high burn-up UO<sub>x</sub> fuel in comparison to calculated values. .... - 87 -

**Table 5.6:** Atomic composition and uncertainties in atom % of the chlorine and iodine bearing agglomerate within the interaction layer of the defueled Zircaloy specimen..... - 108 -

**Table A.1:** Experimentally determined activation product inventory for all samples..... - 133 -

**Table A.2:** Experimentally determined fission product inventory for all samples.. - 133 -

**Table A.3:** Experimentally determined actinide inventory for all samples..... - 134 -

**Table A.4:** Experimentally determined total inventory of selected fission products for both fuel types assuming 100 μm of RIM area. .... - 135 -

**Table A.5:** Experimentally determined total inventory of selected actinides for both fuel types assuming 100 μm of RIM area..... - 135 -

**Table A.6:** Calculated actinide inventory of various regions within the UO<sub>x</sub> fuel pellet as well as values obtained for KORIGEN calculations of the MOX fuel. .... - 136 -

**Table A.7:** Calculated fission product inventory of various regions within the UO<sub>x</sub> fuel as well as values obtained for KORIGEN calculations of the MOX fuel. .... - 136 -

**Table C.1:** Atomic composition and uncertainties in atom % of phase 1 (red) of the alkaline defueled high burn-up UO<sub>x</sub> fuel Zircaloy specimen. .... - 139 -

**Table C.2:** Atomic composition and uncertainties in atom % of phase 2 (yellow) of the alkaline defueled high burn-up UO<sub>x</sub> fuel Zircaloy specimen. .... - 139 -

**Table C.3:** Atomic composition and uncertainties in atom % of phase 3 (blue) of the alkaline defueled high burn-up UO<sub>x</sub> fuel Zircaloy specimen. .... - 139 -

**Table C.4:** Atomic composition and uncertainties in atom % of phase 4 (green) of the alkaline defueled high burn-up UO<sub>x</sub> fuel Zircaloy specimen. .... - 139 -

## List of abbreviations

(aq)	aqueous species
(nat)	natural
(l)	liquid
(s)	solid
AFI	accessible fraction of inventory
a. g.	analytical grade
AMP	ammonium molybdophosphate
BWR	boiling water reactor
cpm	counts per minute
EDS	energy dispersive X-ray spectroscopy
HLW	high-level waste
IAEA	International Atomic Energy Agency
IC	ion chromatography
ICP-MS	inductively coupled plasma mass spectrometry
INE	Institut für Nukleare Entsorgung / Institute for Nuclear Waste Disposal
KARA	Karlsruhe Research Accelerator
KIT	Karlsruhe Institute of Technology
KKG	Kernkraftwerk Gösgen / nuclear power plant Goesgen
KWO	Kernkraftwerk Obrigheim / nuclear power plant Obrigheim

LLFP	long-lived fission product
LSC	liquid scintillation counting
LWR	light water reactor
MOX	mixed oxide fuel
PCI	pellet-cladding interaction
PP	polypropylene
r.t.	room temperature
PWR	pressurised water reactor
RN	radionuclide
sat.	saturated
SCC	stress corrosion cracking
SEM	scanning electron microscopy
SNF	spent nuclear fuel
TOC	total organic carbon
WDS	wavelength dispersive X-ray spectroscopy
XANES	X-ray absorption near edge structure spectroscopy
XAS	X-ray absorption spectroscopy
XPS	X-ray photoelectron spectroscopy
Zry-2	Zircaloy-2
Zry-4	Zircaloy-4



# **1 Introduction**

## **1.1 Background**

Since the dawn of the nuclear age in the 2<sup>nd</sup> half of the 20th century, countries which utilised nuclear energy from commercial power plants are in search for a safe disposal option for high-level waste (HLW), mainly spent nuclear fuel (SNF) or vitrified high active waste concentrates, originating from SNF reprocessing and consecutive vitrification. For numerous countries, as well as the Federal Republic of Germany, the direct disposal of SNF in a deep geological repository (DGR) without reprocessing of the fuel elements is the favoured option for the back end of the nuclear fuel cycle [EUROPEAN UNION, 2011; IAEA, 2018]. Regarding the long-term safety of a final repository for HLW, the concept of a multi-barrier system is internationally discussed, in which the nuclear waste will be disposed of in deep geological formations with high inclusion and retention capabilities, protected from the biosphere by several independent, passive and robust barriers. It is of utter importance that after closure, the safety of a final repository will be assured by a system of resilient and eclectic barriers, namely:

- i. A technical barrier, consisting of the waste matrix itself, a metallic container and, in case of SNF, the cladding tubes;

## Introduction

---

- ii. a geotechnical barrier, being composed of materials enhancing the mechanical stability, minimising cavities, preventing the intrusion of solutions or by retarding their inflow to the emplaced waste and thus retain the release of RNs;
- iii. a geological barrier, meaning the host rock and in some cases an additional overlying geological formation (overburden).

In most countries, three different types of lithologies are considered as potential host rocks for HLW, e.g. rock salt, clay rock or crystalline rock.

Geological repositories for radioactive waste in rock salt mines are in operation in Germany (Morsleben low / intermediate level waste repository, Saxony-Anhalt) and in the United States of America (transuranic waste repository “Waste Isolation Pilot Plant”, New Mexico). The benefits of final disposal of radioactive waste in rock salts are the low permeability and high thermal conductivity. Furthermore, salt rock provides an excellent self-sealing probability due to the high plasticity. However, the elevated corrosivity of saline solutions and solubility of salt, as well as the lack of a high retention capability for the radionuclides emplaced inside are considered as a disadvantage of rock salt as a host rock for a DGR [BGR, 2007].

Clay / Clay rock as a host rock type is currently under investigation in e.g. Belgium (Boom Clay), France (Callovo-Oxfordian Clay) and Switzerland (Opalinus Clay). Argillaceous rocks are characterised as nanoporous sediments with only diffusive water transport and offer next to their low permeability and high retention of radionuclides, a high plasticity. Nevertheless, due to the high plasticity of clay formations, difficulties could arise in terms of excavation stability during the building of a DGR. Additionally, the high salinity of pore water in some argillaceous rocks and low thermal conductivity / temperature load in clay lithologies have to be considered in performance assessment studies.

Final disposal of HLW in crystalline rock repositories is already determined in Finland (ONKALO spent nuclear fuel repository, Eurajoki) and Sweden (Forsmark spent fuel repository, Uppland) in crystalline bedrock. The high tectonic stability and low solubility of granitic rock makes it an appropriate choice for a DGR, yet due to the fractured nature

of the lithology it creates a migration pathway for radionuclides upon groundwater contact. To prevent this scenario, the Swedish KBS-3 concept provides a copper-lined cast iron container, which is planned to be embedded in a bentonite back-fill barrier in order to retard groundwater contact with the waste and radionuclide release to the biosphere [SKB, 2006].

Yet, the first barrier relevant to geological disposal of used fuel elements is the SNF as a waste form itself. The chemical inventory and radioactivity of the irradiated fuel differs significantly from its time before in-reactor usage as “fresh” UO<sub>2</sub> or (U, Pu)O<sub>2</sub> fuel. Due to the fission of U-235, neutron capture by U-238 successor nuclides and structural materials, transuranic isotopes, fission as well as activation products are generated which, in addition to irradiation damage and thermal stress, alter the characteristics of the fuel remarkably [EWING, 2015]. Amongst these newly produced radionuclides (RN), some are of major concern in safety analyses for DGR in terms of their rapid release from the SNF waste form. This “instantaneous” release, denoted as accessible fraction of inventory (AFI)<sup>1</sup>, is owed to the mobility and redox insensitivity of various radionuclides generated, e.g. the caesium isotopes, I-129 as well as the activation product Cl-36 [RONDINELLA *ET AL.*, 2013].

Chlorine-36 ( $E_{\beta\text{max}} = 709.53 \text{ keV}$ ) is generated due to impurities in the cladding, adjacent reactor materials (e.g. steel components) and fuel via neutron activation of the natural occurring isotope Cl-35 (75.77 % natural abundance) by the reaction  $^{35}\text{Cl}(n,\gamma)^{36}\text{Cl}$ . With a half-life of  $3.01 \times 10^5 \text{ a}$ , low retention potential in various lithologies and high accumulation capability in plant tissue, it is denoted a major risk in safety assessment studies [COLLE *ET AL.*, 2005; BYTWERK AND HIGLEY, 2009]. However, the quantification of the amount of produced Cl-36 in fuel rod and cladding impurities displays a considerable uncertainty since its formation depends on many reactor operating parameters, e.g. burn-up and linear power rating [JOHNSON AND TAIT, 1997; HUMMEL, 2017].

---

<sup>1</sup> Also referred to as “Instant Release Fraction” (IRF).

The  $\gamma$ -emitting fission product iodine-129 ( $E_{\gamma} = 39.58$  keV) on the other hand is formed as a fission product inside the fuel with a thermal fission yield of 0.71 % and 1.41 % for U-235 and Pu-239, respectively [NICHOLS *ET AL.*, 2008]. Contrary to the non-repository relevant isotope I-131, which is of major safety concern in the first stages of nuclear accidents, I-129 contributes, due to its half-life of  $1.57 \times 10^7$  a, to the long-term radiotoxicity of SNF next to other long-lived fission products, as well as long-lived actinides and activation products.

Special focus needs to be set on the ability of these volatile radionuclides to migrate to the fuel-cladding gap during in-pile service, affected by temperature gradients. With increasing burn-up this gap between fuel and cladding closes and forms an interaction layer as basis for chemical interactions. Currently, in Germany and in other countries, discussions on the integrity of the cladding following a prolonged dry interim storage arise [WOLFF *ET AL.*, 2013; ESK, 2015]. At this, amongst other effects, like hydrogen uptake, hydride formation or the formation of oxide layers, halogen induced stress corrosion cracking is considered, which could lead to serious embrittlement due to fuel-cladding chemical interactions assisted by RNs like Cl-36 and I-129 [VISWANATHAN, 2014; SPYKMAN, 2018].

Therefore, both Cl-36 and I-129 are of great radiological significance not only in terms of the long-term safety analysis of a DGR regarding their risk potential for the biosphere in case of release from a repository, but also concerning the fact that prolonged interim storage will occur until a final repository is available. In comparison to a number of long-lived activation and fission products (e.g. Tc-99) and long-lived actinides, which undergo retardation in the technical and geo-engineered barriers as well as in the argillaceous or crystalline host rock system of a DGR, the supposedly anionic species of chlorine and iodine would not be retained [GRAMBOW *ET AL.*, 2011].

Recent studies report retardation effects for the volatile, long-lived activation and fission products Cl-36, I-129 and Se-79 in altered cementitious near-field environments [POINTEAU *ET AL.*, 2008; METZ *ET AL.*, 2013; WIELAND, 2014]. As cementitious material (e.g. Portland cement, Sorel concrete) is foreseen in many repository concepts, the arising

cement corrosion products display an interface for the sorption of these anionic RN in the event of release from a failed container in a DGR.

## 1.2 Objectives of this work

The present thesis aims at studies in context of the interim storage and final disposal of spent nuclear fuel assemblies in terms of the volatile fission and activation products I-129 and Cl-36. In long-term safety assessments, these isotopes are considered to contribute significantly to the radioactive exposure of the biosphere in case of pore water ingress into a DGR. Thus, additional information about their amount and release behaviour is indispensable. Therefore, in this study a separation method for Cl-36 and I-129 from the matrix of spent nuclear fuel was developed in order to acquire a better understanding in terms of their inventory fraction in SNF as well as their leached fraction from SNF in contact with water. In addition, this study deals especially with the fuel-cladding interaction layer, as the Zircaloy tubes of the spent fuel assemblies represent a part of the primary barrier of the nuclear waste, both in case of interim storage and long-term final disposal. At this, a thorough understanding is required to describe the possible corrosion processes due to caesium / chlorine / iodine containing phases accumulating at the fuel-cladding interface at higher burn-ups. Therefore, special focus is given to the accurate chemical composition of such phases, which is important to scrutinise existing models on the precipitation of fission- / activation-product bearing compounds at the fuel-cladding interface. Furthermore, the thesis gives an insight into corrosion phenomena of the cladding material under in-pile conditions after discharge from the reactor cores. These corrosion phenomena are of relevance for the integrity of the cladding tubes regarding either the relocation of older, already cooled off fuel assemblies in wet storage or a prolonged dry interim storage. Up until now, the relocation of the fuel rods, seems to be

unavoidable, regarding the absence of an operating DGR for HLW worldwide [BONANO *ET AL.*, 2018]. The three main objectives of this work can be summarised as follows:

- I. The Cl-36 and I-129 inventory of irradiated UO<sub>x</sub> and MOX fuel will be determined by means of a newly developed radiochemical separation procedure for highly radioactive samples and compared to theoretically obtained results. The radiochemical determination focusses on the different parts of irradiated fuel rod segments namely the fuel matrix itself, the cladding and especially the fuel-cladding interaction layer in which a large portion of the volatile fission products accumulate. Quantification of the radionuclides is performed by liquid scintillation counting (LSC),  $\gamma$ -spectrometry as well as inductively coupled mass spectrometry (ICP-MS) and ion chromatography (IC). Resulting data could give more insights into the mobility of Cl-36 and I-129 within the SNF pellet and their probability of being released from the fuel matrix after canister failure scenarios.
- II. The chemical composition of caesium / chlorine / iodine containing phases, which precipitated at the interface of the fuel with the Zircaloy cladding tube, is investigated by means of different spectroscopic methods including SEM-EDS / -WDS, XPS and XAS measurements, as well as taking into account different fuel types (irradiated UO<sub>x</sub> and MOX) and burn-ups (50.4 GWd/t<sub>HM</sub> and 38.0 GWd/t<sub>HM</sub>).
- III. In the context of fuel rod stability during prolonged interim storage, corrosion phenomena of the cladding material are examined in terms of experiments with synthesised U-O-Zr-Cs-Cl-I-phases deposited on Zircaloy cladding. Therefore, compounds such as depleted UO<sub>2</sub>, CsCl and CsI are brought in contact with non-irradiated reactor grade Zircaloy and kept under conditions of dry interim storage for three months in a gas-tight autoclave with successive reduction of the temperature starting from approximately 400°C down to room temperature. Afterwards, the samples are characterised by SEM-EDS and XPS to gain a better understanding on degradation processes during prolonged dry storage of nuclear fuel assemblies.

## 2 SNF in context of storage and disposal

The main waste product arising from electricity production utilising nuclear fission is SNF, largely in the form of irradiated  $\text{UO}_2(\text{s})$ . After utilisation of the fuel in a reactor, two options for safe management of high radioactive SNF are conceivable. Whereas a so-called *closed fuel cycle* considers the SNF to be reprocessed in order to retrieve the remaining fissile radionuclides (mainly Pu-239, built-up during reactor operation by neutron capture of U-238 and consecutive  $\beta^-$ -decays), whilst the high radioactive residuals separated by reprocessing are vitrified; the concept of a so-called *open fuel cycle* foresees the direct disposal of SNF in a DGR after storage in water-filled storage pools, and in some countries followed by dry storage in surface facilities to dissipate the decay heat of the fuel assemblies and bypass to time until construction and commissioning of a geological repository for high-level waste.

The volumetric amount of SNF only displays a small percentage of the produced nuclear waste, yet, its long-term disposal remains one of the most challenging tasks due to the high radioactivity, radiotoxicity and complex redox-sensitive system [EWING, 2008; GECKEIS *ET AL.*, 2012; SPAHIU *ET AL.*, 2020].

## 2.1 Composition of spent nuclear fuel

The nuclide composition of SNF differs significantly from the starting material  $\text{UO}_2$  or MOX fuel. During reactor operation two substantial reactions take place, affecting the chemical behaviour and homogeneity of the initial fuel. Due to nuclear chain reactions, fission products are formed proceeding from the initial U-235 or Pu-239 and resulting in a bimodal distribution of mass numbers with maxima at approximately 90 and 140. In addition, transuranic isotopes are generated because of neutron capture and subsequent  $\beta^-$ -decay starting from U-238 [BRUNO AND EWING, 2006]. Yet, the ultimate composition of the SNF is depending on various factors, e.g. the type of fissile material, its initial enrichment and manufacturing process, neutron energy, the activation of impurities as well as the burn-up and linear power rate of the fuel during reactor operation.

The chemical state and distribution of the generated fission products and transuranic isotopes can be described in categories as follows [KLEYKAMP, 1985; KONINGS *ET AL.*, 2015]:

- i. Fission gases and volatile fission products (Br, Kr, Rb, I, Xe, Cs and Te), which are finely dispersed as bubbles in the pores within the fuel matrix [WALKER *ET AL.*, 2009]. These radionuclides are typically localised in the plenum of the fuel rod, the pellet-cladding gap and in the porosity structure of the fuel.
- ii. Fission products forming mono- or two-phase metallic precipitates (Mo, Tc, Ru, Rh, Pd, Ag, Cd, In, Sn, Sb, Se and Te) characterised as  $\epsilon$ -particles. They are immiscible in the fuel matrix and occur as solid solutions with a varying composition [KLEYKAMP, 1989; CUI *ET AL.*, 2011].
- iii. Fission products forming perovskite-type oxide precipitates (Rb, Sr, Zr, Nb, Mo, Se, Te, Cs and Ba) with an  $\text{ABO}_3$  structure [KLEYKAMP *ET AL.*, 1985; HE *ET AL.*, 2007].

- iv. Fission products dissolved as oxides within the fuel matrix (Rb, Sr, Y, Zr, Nb, Te, Cs, Ba, La, Ce, Pr, Nd, Pm, Sm and Eu) forming solid solutions with the UO<sub>2</sub>.
- v. Transuranic isotopes and lanthanides, which substitute uranium in the fuel matrix.

Furthermore, activation products produced due to neutron capture by trace contaminants within the fuel and cladding are distributed in various parts of a fuel rod. For instance Cl-36 and C-14 occur mainly in the gap region and the cladding, respectively. Regarding this variety of actinides, activation and fission products in different physicochemical environments, knowledge about their chemical behaviour and transport mobility in the fuel matrix is of utter importance for the long-term safety of SNF disposal. Due to the steep radial thermal gradient between the centre of the pellet and the rim, the distribution of the radionuclides within a spent fuel pellet and the adjacent cladding is heterogeneous (see Figure 2.1) resulting in a complex chemistry of the SNF [BRUNO AND EWING, 2006; EWING, 2015].

In addition to the radial temperature gradient from the pellet centre to the cladding tube in contact with the coolant, an axial gradient along the fuel rod is observed. As the centre of the fuel rod is experiencing a higher neutron flux, the yield of undergone fissions and thus generated fission products is elevated in contrary to the upper and lower parts of the fuel rod<sup>2</sup> as examined via gamma scanning in fuel pools or hot cells [NEEB, 1997].

---

<sup>2</sup> For pressurised water reactors (PWRs) the axial distribution of fission products alongside the fuel rod is homogeneous according to gamma scans; for boiling water reactors (BWRs) a heterogeneous, asymmetric distribution is observed due to the varying positions of the control rods [NEEB, 1997].

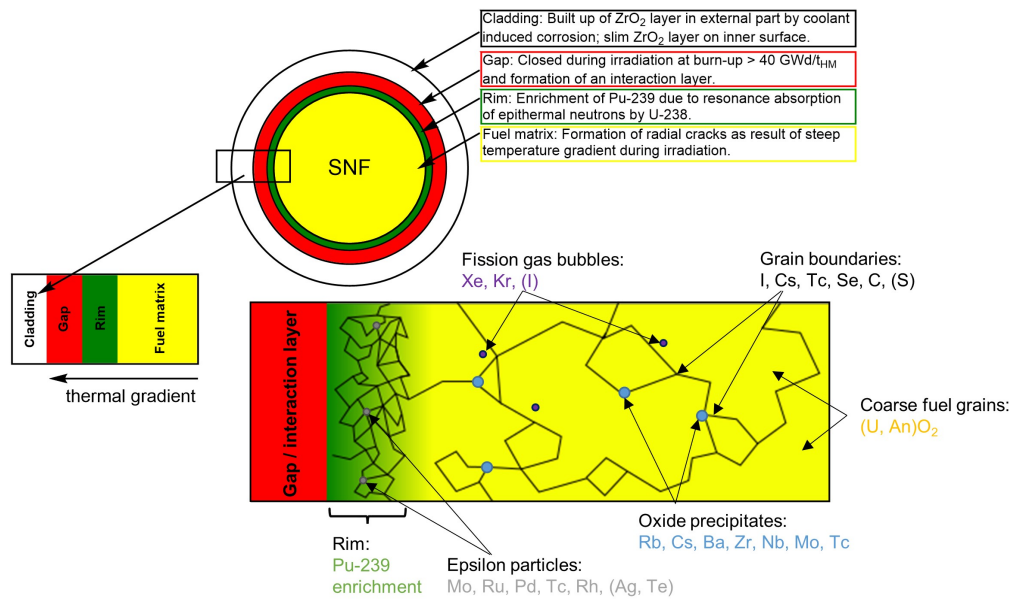


**Figure 2.1:** Microstructure of SNF and distribution of actinides and fission products. Adapted from [EWING, 2015].

### 2.1.1 Long-lived fission and activation products

Whereas most of the generated radioisotopes, which presently dominate the radioactivity of SNF, such as Cs-137 or Sr-90 will decay within the first few hundred years, certain fission products have half-lives exceeding the timescale of  $10^5$  a. These long-lived fission products (LLFP) determine the abiding radiotoxicity of the SNF next to the long-lived actinides and activation products. The seven most prominent LLFP are listed in Table 2.1 with respect to their half-lives, type of decay and fission yield for U-235 [OECD-NEA, 2006].

**Table 2.1:** Half-lives, type of decay and thermal fission yield of LLFP.

radionuclide	half-life [Ma]	type of decay	fission yield for U-235 [%] <sup>d</sup>
<b>Se-79</b>	0.327 <sup>a</sup>	$\beta$	0.045 $\pm$ 0.004
<b>Zr-93</b>	1.64 <sup>b</sup>	$\beta, \gamma$	6.340 $\pm$ 0.045
<b>Tc-99</b>	0.211	$\beta$	6.138 $\pm$ 0.068
<b>Pd-107</b>	6.5	$\beta$	0.145 $\pm$ 0.0004
<b>Sn-126</b>	0.233 <sup>c</sup>	$\beta, \gamma$	0.056 $\pm$ 0.004
<b>I-129</b>	15.7	$\beta, \gamma$	0.543 $\pm$ 0.0001
<b>Cs-135</b>	2.3	$\beta$	6.526 $\pm$ 0.028

<sup>a</sup>[JÖRG *ET AL.*, 2010], <sup>b</sup>[CASSETTE *ET AL.*, 2010], <sup>c</sup>[CATLOW *ET AL.*, 2005], <sup>d</sup>fission yield data for thermal fission obtained from NDC-JAEA (<https://wwwndc.jaea.go.jp/NuC/index.html>), last visited on 16.02.2022.

Furthermore, thermal neutrons produced by the ongoing fission of U-235 or Pu-239 can induce neutron activation reactions with the nuclear fuel, cladding material and structure components of the reactor. Assertions on the quantity of these activation products are difficult, since many of the radionuclides are generated due to impurities in the materials listed above. In terms of final disposal of irradiated fuel rods, the isotopes C-14 ( $t_{1/2} = 5730$  a), Cl-36 ( $t_{1/2} = 301000$  a) and Ag-108m ( $t_{1/2} = 438$  a) are of great significance regarding their mobility and release behaviour [EVANS *ET AL.*, 1984; HUMMEL, 2017]. Exemplarily the neutron activation reactions of C-14<sup>3</sup> are shown in the equations 2.1 – 2.3 [MAGILL *ET AL.*, 2018]:

<sup>3</sup> Neutron capture reactions resulting in Cl-36 are given in the following chapter.



## **2.1.2 Behaviour of spent nuclear fuel under conditions of a deep geological repository**

Although, geological, geotechnical and technical barriers may prevent to some extent the groundwater from contacting SNF, water ingress into a breached container and subsequent interaction with SNF has to be taken into account within the long-term safety case of a DGR. The resulting corrosion chemistry of the SNF displays a complex issue, since a variety of factors e.g. groundwater composition, redox conditions and fuel properties are affecting the alteration of the fuel. Dispersion of the radionuclides within the fuel (gap, grain boundaries, high burn-up rim region) is considerably influencing their release behaviour [POINSSOT *ET AL.*, 2004; RONDINELLA AND WISS, 2010]. The radionuclide release mechanism of SNF can be described in three phases: (i) a rapid release of radionuclides from high reactive sites of the SNF pellets and adjacent cladding, such as caesium, chlorine or iodine denoted as AFI or as “instantaneous release”, (ii) the release of RN from grain boundaries of the SNF and (iii) the ultimately dissolution of the fuel matrix itself governed by radiolytic and thermodynamic processes [BRUNO AND EWING, 2006; GECKEIS *ET AL.*, 2012; FANGHÄNEL *ET AL.*, 2013].

After breaching of the container and fuel cladding, water contact with SNF leads to a fast release of the radionuclides from the fuel gap and fractures. This prompt release of mobile and easy soluble species within a few weeks after water ingress is followed by a slower

release of radionuclides from the grain boundaries in the SNF pellet [GRAMBOW *ET AL.*, 1996, 2000]. The release of radionuclides in these first steps is depending on many factors, e.g. irradiation history of the fuel, burn-up and linear power rate. The AFI includes to some extent the fission gases (Kr, Xe), volatile fission products (Cs, Se, I) as well as metallic precipitates (Tc, Sn) [JOHNSON *ET AL.*, 2004].

In conjunction with the rapid release explained above, a much slower dissolution of the matrix bound radionuclides due to corrosion of the  $\text{UO}_2(\text{s})$  occurs. This corrosion is governed to some extent by oxidising species generated by radiolysis of the ingressed water ( $\text{H}_2\text{O}_2$ ,  $\text{O}_2$  and respective radicals) near the fuel surface and complexing agents (e.g. carbonate) [CLARENS *ET AL.*, 2005; EWING, 2015; SPAHIU *ET AL.*, 2020]. These effects compete with the reducing conditions of a repository, e.g. groundwater redox potential, near neutral or slightly alkaline pH range<sup>4</sup> and corrosion inhibiting  $\text{H}_2$ -overpressure, descending from iron corrosion of the SNF cask. Figure 2.2 gives an overview of the different chemical processes which might affect the alteration of SNF upon contact with groundwater.

Yet, until the commissioning of a DGR, the high-level waste is stored under interim storage conditions, i.e. wet storage in a spent fuel pool or, as practiced in Germany and in Switzerland, in a dry storage facility subsequent to an appropriate cooling time in a SNF pool. As described in the following sections (see chapter 2.3 – 2.6), during dry interim storage various degradation effects may enhance the cladding embrittlement further, e.g. fission gases produced during reactor operation, especially from high burn-up fuel leading to an elevated rod pressure together with helium generation due to ongoing alpha decays, as well as the reorientation of hydride precipitates inside the cladding tube [SPYKMAN, 2018].

---

<sup>4</sup> In the current Belgian DGR concept for SNF and high-level waste glass, strongly alkaline conditions due to a large cementitious overpack are envisaged.

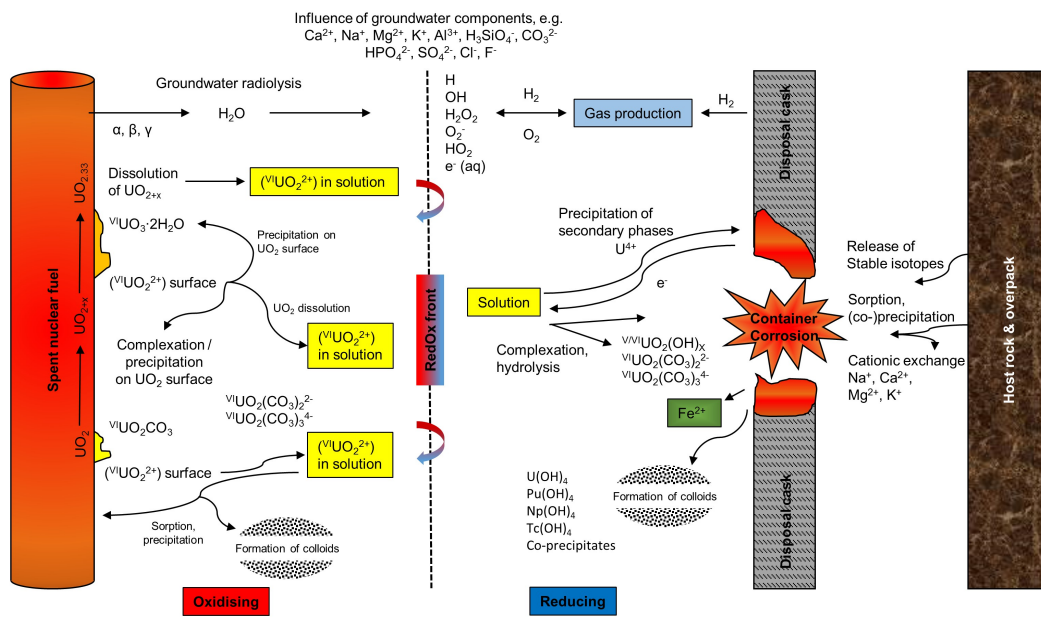


Figure 2.2: Chemical processes which might affect the alteration of SNF upon contact with groundwater. Adapted from [EWING, 2015].

## 2.2 Cladding material of LWR nuclear fuel rods

Fuel pellets ( $UO_2$  or MOX) as they are used in light water reactors (LWR) are usually embedded in a cladding tube consisting of an inert and corrosion resistant metal. At this, the enriched nuclear fuel is inserted in form of cylindrical pellets into long cladding tubes, pressurised with helium to improve the heat conductivity of the system and sealed air-tight by welding two end caps on the fuel rod under inert helium atmosphere. To ensure that the fuel stack stays in position during the irradiation processes, a steel spring is inserted into the upper plenum part of the fuel rod. This plenum space also displays a free

accumulation area for fission gases released during the irradiation processes from the pellets, without straining the surrounding cladding of the fuel by additional overpressure. Likewise, the lower part of the fuel rod is sealed by welding an end cap with a guidance for the bottom plate onto it [RUDLING *ET AL.*, 2007; OLANDER, 2009].

The respective tubes are bundled in varying lattices, depending on the reactor type (e.g.  $14 \times 14$ ,  $15 \times 15$ ), to form the nuclear fuel assembly which is then placed into the reactor core [BAILLY *ET AL.*, 1999]. Due to the harsh conditions during irradiation, combined with the constant build-up of fission products and strain upon the cladding, its material, mechanical and nuclear properties are of great importance.

In present LWRs, the cladding tubes of most nuclear fuel rods consist of zirconium alloys. Zirconium has suitable properties for in-reactor use like a very low thermal neutron absorption, good mechanical stability and, most important, very low corrosivity in water at high temperatures [NEEB, 1997; BAILLY *ET AL.*, 1999]. For LWRs zirconium alloys, predominantly Zircaloy-2 (Zry-2) for boiling water reactors (BWR) and Zircaloy-4 (Zry-4) for pressurised water reactors (PWR) are most commonly used in western reactor designs<sup>5</sup>. Table 2.2 gives an overview on the composition of Zry-2 and Zry-4 with respect to impurities and alloying elements within the material<sup>6</sup>.

---

<sup>5</sup> For the different BWR and PWR reactor designs and generations, the zirconium alloys may vary in their chemical composition regarding additives and alloying compounds.

<sup>6</sup> Chlorine impurities are given in section 3.1.

**Table 2.2:** Main alloying elements and impurities in Zry-2 and Zry-4 in weight % [RUDLING *ET AL.*, 2007].

---

<b>Alloying elements</b>	<b>Zry-2</b>	<b>Zry-4</b>
<b>Zirconium</b>	balanced	balanced
<b>Tin</b>	1.20 – 1.70	1.20 – 1.70
<b>Iron</b>	0.07 – 0.20	0.18 – 0.24
<b>Chromium</b>	0.05 – 0.15	0.07 – 0.13
<b>Nickel</b>	0.03 – 0.08	-
<b>Oxygen</b>	0.09 – 0.16	0.09 – 0.16
<b>Silicon</b>	0.005 – 0.012	0.005 – 0.012
<b>Impurities</b>		
<b>Aluminium</b>	< 0.0075	< 0.0075
<b>Boron</b>	< 0.00005	< 0.00005
<b>Cadmium</b>	< 0.00005	< 0.00005
<b>Carbon</b>	< 0.0270	< 0.0270
<b>Cobalt</b>	< 0.0020	< 0.0020
<b>Copper</b>	< 0.0050	< 0.0050
<b>Hafnium</b>	< 0.0100	< 0.0100
<b>Hydrogen</b>	< 0.0025	< 0.0025
<b>Magnesium</b>	< 0.0020	< 0.0020
<b>Manganese</b>	< 0.0050	< 0.0050
<b>Molybdenum</b>	< 0.0050	< 0.0050
<b>Nitrogen</b>	< 0.0080	< 0.0080
<b>Tungsten</b>	< 0.01	< 0.01
<b>Titanium</b>	< 0.0050	< 0.0050
<b>Uranium</b>	< 0.00035	< 0.00035

---

## 2.3 Interim storage of SNF

According to the IAEA report “Status and Trends in Spent Fuel and Radioactive Waste management” [IAEA, 2018] over 250000 t<sub>HM</sub> are currently stored in either wet or dry interim storage facilities. Independently from the mode of interim storage, the most important criteria of both designs is to maintain subcriticality and integrity of the emplaced fuel assemblies as well as to allow a further handling of the SNF subsequent to the storage period [IAEA, 1999].

Wet storage of LWR SNF assemblies is in general performed at reactor-site in spent fuel pools, with the exception of reprocessing facilities (e.g. La Hague, France or Sellafield, United Kingdom), where the fuel will be reprocessed afterwards for new fuel production. Due to the increasing amount of SNF and the limited capacity of on-site reactor pools, additional storage space is needed in form of either supplementary SNF pools, largely or completely independent from the initial reactor-site storage pool, or dry interim storage facilities [IAEA, 1999].

By far, the major amount of SNF worldwide is currently stored in wet interim storage pools, which dissipate the decay heat by an active cooling system via the pool water and provide radioactive shielding for the fuel assemblies submerged in water as practiced for example in the CLAB interim storage facility located on the premises of the nuclear power plant of Oskarshamn in Sweden [IAEA, 2003]. The devoted spent fuel pools consist in most cases of reinforced concrete structures equipped with a stainless steel liner and are filled with deionised water. Similar to the coolant of the primary and secondary circuit in LWRs during reactor operation, the pool water quality and the resulting chemistry (e.g. pH, conductivity, additives in the pool water) is one of the most crucial aspects in order to avoid cladding degradation during storage time. In general, zirconium-based fuel rod claddings, if not damaged during reactor operation, are very resistant against any type of corrosion due to the formation of an outer zirconia layer [IAEA, 1998].

The main cladding degradation process occurring during wet interim storage of SNF is the ductile-to-brittle transition of incorporated hydrides (see section 2.5). However, countries worldwide utilising wet storage for used fuel assemblies are reaching their capacity limit of the respective pools. Therefore, older, already cooled off fuel assemblies are relocated from wet storage pools to dry interim storage facilities as described in case of the United States of America by Bonano and co-workers [BONANO *ET AL.*, 2018].

For countries (e.g. Germany, Canada) whose governmental regulations focus on the direct disposal of used fuel assemblies without reprocessing, successive dry interim storage, after cooling off the decay heat to manageable levels<sup>7</sup> in pools at reactor-site, is envisaged. For dry interim storage, two profound and established concepts are currently being pursued: Either storage of used fuel assemblies in vault type facilities consisting of reinforced concrete with an internal metallic liner or the storage of the SNF in a container system [IAEA, 1999].

Vaults type facilities (e.g. MVDS facility in Paks, Hungary) receive the SNF assemblies from a reactor pool in transport casks, from which they are lifted into a drying tube and afterwards extracted by means of a fuel handling machine and emplaced inside the vault structure. Before closing of the storage tube inside the vault, an inert atmosphere is established. Shielding from radiation is given by the surrounding structure and decay heat is dissipated by either natural air convection or by use of an auxiliary cooling system [IAEA, 1999; BENCZE, 2017].

Storage of spent fuel in container systems, either metallic / concrete casks or silos, yields the benefits of radiological shielding by the vessel itself as well as the capability of an uncomplicated transportation of the emplaced assemblies to e.g. a final disposal site. At this, the used fuel assembly is loaded under water into a transport and storage cask and the residual water is removed by means of vacuum drying. In order to reduce any corrosive and degrading effects of possible remains of oxygen or water vapour into the

---

<sup>7</sup> The time for LWR SNF in spent fuel pools in order to dissipate the decay heat to manageable levels depends largely on the fuel type (UO<sub>x</sub> or MOX) and irradiation conditions (e.g. burn-up, average linear power, ramping).

transport and storage cask, the interior of the vessel containing the used fuel assemblies is pressurised with inert helium gas to approximately 0.8 bar as for example in the CASTOR<sup>®</sup> vessel [DROSTE AND KOWALEWSKY, 1987; IAEA, 2014; SCHNEIDER-EICKHOFF, 2021]. Afterwards, the hermetically enclosed transport and storage casks are transferred to dry interim storage facilities and either stored in an open space for cooling or placed inside a building as shown in figure 2.3, where the decay heat, subsequently generated from ongoing decay processes inside the SNF, is dissipated by means of natural air convection through vents in the building walls.

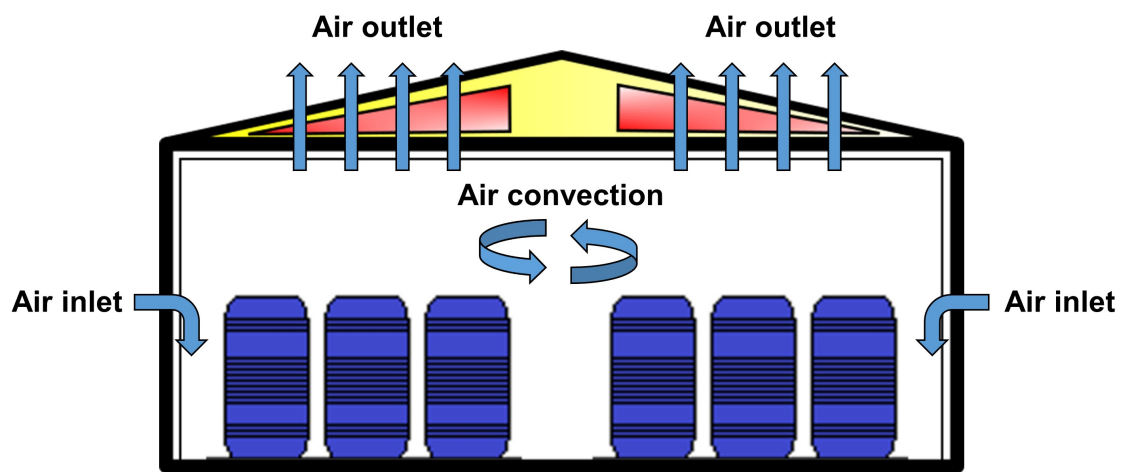


**Figure 2.3:** Simplified structure of an interim storage facility.

The encapsulated fuel assemblies inside the transport and storage casks do not remain unchanged with time, as ongoing physical embrittlement processes and chemical degradation phenomena alter the structure of the nuclear fuel and may affect the integrity of the cladding beyond reactor discharge (see chapters 2.4 – 2.6).

## 2.4 Physical embrittlement processes during reactor operation and storage

With the reactor core going critical, the material properties of the inserted nuclear fuel undergoes drastic changes. As a consequence of nuclear chain reactions, energy is released in great measure in form of kinetic energy due to the fission of uranium or plutonium into two lighter fission product nuclei and to a smaller extent as  $\beta$  and  $\gamma$  radiation, resulting in the immense heat production in the nuclear fuel assemblies. The elevated temperature within the individual fuel pellets is not evenly distributed as the centre of the fuel is experiencing a much higher temperature than the cladding being in contact with the coolant which leads to a steep thermal gradient within the respective pellet-cladding system [ZIEGLER AND ALLELEIN, 2013]. On account of this radial difference in temperature, the fuel will undergo a swelling process yielding in a reduction of the gap size between fuel and cladding as well as the strain-driven fracturing and “hour-glassing” of the fuel pellet structure itself [OLANDER, 2009]. With increasing burn-up, another effect is occurring within the pellet-cladding system namely a bonding phenomenon between fuel and cladding due to the further swelling of the fuel matrix by generated solid fission products, and additionally, a creep effect induced by radiation and, in PWRs, by the external pressure of the coolant [CISZAK *ET AL.*, 2019].

After in-reactor service, additional embrittlement processes may strain the cladding even more. Following successive wet storage and emplacement in a dry interim storage cask, the rod internal pressure of LWR fuel rods is in the region of 40 to 60 bar, without taking into account additional helium production due to subsequent alpha decays and fission gas release [POINSSOT *ET AL.*, 2002]. Thus, the cladding will experience an elevated hoop stress, which, in conjunction with the temperature decreases from approximately 400 °C<sup>8</sup>

---

<sup>8</sup> This threshold value refers to the IAEA TECDOC-1862 [IAEA, 2014]. In Germany, a threshold value of 370 °C is envisaged as described by e.g. Rowold and co-workers [ROWOLD *ET AL.*, 2018].

to room temperature over an extended period of several decades, will lead to a thermal creep mechanism that could result in the loss of cladding integrity by the reduction of the rods elasticity modulus in combination with the impairment due to precipitated hydrides [PAN *ET AL.*, 2010]. Yet, it is still afflicted with uncertainties, if the mentioned processes will affect the cladding integrity within the time frame of just a few decades [POINSSOT *ET AL.*, 2002; ELLINGER *ET AL.*, 2010]. From a metallographic point of view, the expected prevalent temperature of the SNF rods within an interim storage cask is too low to enable a self-sustaining annealing of the cracks in the nuclear fuel pellet as well as of the embrittled Zircaloy cladding [RIGBY, 2010].

## 2.5 Chemical degradation phenomena during reactor operation and storage

The chemical composition of the nuclear fuel, starting in its initial form  $\text{UO}_2$  or  $(\text{U}, \text{Pu})\text{O}_2$ , is significantly altered due to the neutron induced nuclear fission as new isotopes and hence new chemical compounds are produced. The oxygen potential within the fuel system before irradiation is predominantly stable and depends on the stoichiometry, i.e. the oxide to metal ratio (O / M ratio), of the nuclear fuel obtained during fabrication. This potential changes during irradiation, as the Zircaloy gathers to some extent the oxygen into the bulk structure under the formation of an inner, proximal zirconia ( $\text{ZrO}_2$ ) layer due to the radial thermal gradient and also newly generated elements consume oxygen released by the nuclear fission of uranium or plutonium in order to form new compounds with different chemical states (see chapter 2.1) [HOLLECK AND KLEYKAMP, 1970; BAILLY *ET AL.*, 1999]. With this variation in the oxygen potential throughout the nuclear chain reaction, fission products, such as caesium, tellurium, iodine or cadmium might meet the

thermodynamic conditions to attack the inner side of the cladding (see chapter 2.6) [GÖTZMANN, 1979; OLANDER, 1982].

Inevitably, the outer Zircaloy layer will oxidise in BWRs (predominantly nodular corrosion) and PWRs (predominantly uniform corrosion) during reactor operation [OLANDER, 2009]<sup>9</sup>. On the coolant side a zirconia layer will form due to the interaction of oxygen from the water with the respective zirconium alloy [NEEB, 1997] and hydrogen will evolve as shown in equation (2.4).



To some extent, this evolved hydrogen is integrated in the Zircaloy bulk by diffusion through the zirconia layer, forming precipitates in the stoichiometric range of  $\text{ZrH}_{2-x}$ . During irradiation, the zirconium hydride intrusions in the cladding are ductile due to the elevated temperature with hydride contents ranging from 200 to 400 ppm and maximum values of up to 600 ppm for LWR fuel Zry-4 claddings [IAEA, 2012].

Yet, after in-reactor service as the fuel rods cool down, these hydrides tend to be brittle, leading to the detriment of cladding integrity by propagation of micro cracks [BAILLY *ET AL.*, 1999; QIN *ET AL.*, 2015]. In the course of dry interim storage of SNF, two other possible hydride-including effects<sup>10</sup> may affect the cladding integrity furthermore, i.e. hydride reorientation (HR), mainly occurring during the drying process of the fuel assemblies, and delayed hydride cracking (DHC) [IAEA, 2012].

With the fuel rod cooling down and in conjunction with external hoop stress, previously formed circumferential hydrides in the cladding tubes are to some extent reoriented radially [CHOUBEY AND PULS, 1994; CHU *ET AL.*, 2007]. According to Daum and co-workers the minimum threshold level of hoop stress at 400 °C for the precipitated

---

<sup>9</sup> Both types of corrosion, nodular and uniform, occur in both reactor types, yet with varying intensity depending on the coolant chemistry and temperature (PWRs are operated at approximately 20 °C higher temperatures) [OLANDER, 2009].

<sup>10</sup> A further hydrogen-including effect is the hydride migration and reorientation after a significant time of storage, whereas hydrides are transported on an axially dimension from the hot centre of the fuel rod to the colder top and bottom parts. This effect is considered as not being significant on cladding degradation mechanisms and thus not further discussed here [IAEA, 2012].

hydrides in high burn-up Zry-4 cladding (average burn-up of 67 GWd/t<sub>HM</sub>) to be reoriented radially is in the range of  $75 \pm 12$  MPa, which is easily obtained for spent power reactor fuels according to TESP-ROD calculations [DAUM *ET AL.*, 2006; SONNENBURG AND BOLDT, 2017; STUKE *ET AL.*, 2018].

Another important degradation phenomenon regarding hydrides is the DHC process. At this, hydrides precipitated at crack tips are relocated alongside a stress gradient from the initial crack tip to the tensile stress area in front of it [GILBERT *ET AL.*, 1987]. There, if the stress level of the already existing crack tip exceeds the stress threshold level of the precipitated brittle ZrH<sub>2-x</sub> compound, the hydride will fracture and propagating crack growth [COLEMAN AND AMBLER, 1977].

As stated before in chapter 2.3, on the fuel side the UO<sub>2</sub> gets in contact with the Zircaloy due to thermal expansion, the progressive swelling of the pellet by gaseous and solid fission products and an irradiation depending inward creep of the cladding result in a strongly bonded interaction layer (see section 2.6). During cooling of the fuel, the bonded pellet-cladding gap reopens again leading to some extent to circumferential cracking which may affect the integrity of the fuel rod [KIM, 2010; JEGOU *ET AL.*, 2015; CISZAK *ET AL.*, 2017].

## 2.6 Chemical pellet-cladding interactions

With the formation of an interface in the fuel-cladding system, chemical interactions between these two are possible. In the past, various models for the pellet-cladding interactions (PCI) have been proposed, e.g. Götzmann, Fee and Johnson [GÖTZMANN, 1979; FEE AND JOHNSON, 1981], which are summarised by Viswanathan [VISWANATHAN, 2014]. Attacks upon the cladding from the fuel are regarded to rely on the fission products caesium, tellurium and iodine which are activated in their chemical reactivity at different

oxygen potentials [GÖTZMANN *ET AL.*, 1974; GÖTZMANN, 1979]. The attack behaviour is at this considered depending on the thermodynamics in the fission product-fuel system, the initial ratio of oxygen to uranium or initial ratio of oxygen to the sum of uranium plus plutonium (O / M ratio) of the fuel, respectively, and operational conditions, e.g. heat generation rate or number of irradiation cycles.

Recent studies by Ciszak and co-workers showed the built-up of a zirconia layer which is formed at the fuel-cladding interface measured by Raman spectroscopy and electron probe micro-analysis for a high burn-up UO<sub>2</sub> fuel (58.7 GWd/t<sub>HM</sub>) [CISZAK *ET AL.*, 2017, 2019]. This zirconia layer displays the adhesive interface for fuel-cladding bonding and thus the reaction zone for pellet-cladding interactions.

The volatile fission product tellurium is transported during reactor operation alongside the thermal gradient by a vapour phase migration process together with caesium to the fuel-cladding gap and expected to precipitate, to some extent, as telluride species, e.g. Cs<sub>2</sub>Te. Chemical interactions between the presumably formed, transient Cs<sub>2</sub>Te and the Zircaloy result in a tellurium-induced cladding embrittlement process under formation of various zirconium tellurides with different stoichiometries [PULHAM AND RICHARDS, 1990; PULHAM *ET AL.*, 1995; VISWANATHAN, 2014].

Furthermore, the effect of the halogens on PCI and their contribution to the degradation of cladding integrity is regarded as one of the reasons for low ductility failures limiting the life-time of nuclear fuel rods [BUSBY *ET AL.*, 1975]. All free halogens are able to initiate a pitting corrosion or stress corrosion cracking process within the cladding tube as shown by Götzmann, Heuvel, Gibs and co-workers [GÖTZMANN AND HEUVEL, 1979; GIBS *ET AL.*, 1982] for steel-clad tubes. Amongst the halogens, only iodine and bromine are generated by fission in noticeable amounts [NEEB, 1997], whilst chlorine and to some extent fluorine are minor impurities within the fuel and cladding originating from the manufacturing process [GÖTZMANN AND HEUVEL, 1979]. Especially the interaction of fission produced iodine as CsI in collaboration with the strong radiation field is seen as a major cause for stress corrosion cracking of the cladding tubes [BALL *ET AL.*, 1989].

Being one of the most abundant fission products, iodine displays a major role in the degradation of the Zircaloy cladding integrity of nuclear fuel rods. The requirements for iodine induced stress corrosion cracking (ISCC) are, according to Knaab and co-workers, a critical stress to crack the protective zirconia layer and a sufficient iodine concentration [KNAAB *ET AL.*, 1987]. One of the main iodine-involving compounds leading to stress corrosion cracking is considered to be CsI precipitated at the fuel-cladding interface [OHSE AND SCHECHTER, 1972; CUBICCIOTTI AND SANECKI, 1978]. Regarding the fission product system, the fission yield of caesium is usually higher than that of iodine, with the exception during a power ramp, thus the chemical reactivity is depending on the caesium activity [GÖTZMANN, 1979; LYSSELL AND SCHRIRE, 1990]. From a thermodynamic point of view, an ISCC of dissociated CsI is not possible due to the chemical stability of CsI and excess caesium over iodine in the system [GÖTZMANN, 1982B; BURNS *ET AL.*, 1985]. Yet, due to the intense radiation, CsI can be dissociated by radiolysis and build up the required iodine pressure to enable stress corrosion cracking [KONASHI *ET AL.*, 1983]. As CsI dissociates and the iodine pressure enhances, vapour transport reactions of the iodine with the exposed zirconium layers of the cladding can take place. At this, the zirconium is transported via a *van-Arkel-de-Boer reaction* from the crack regions (equation (2.5)) of the stressed zirconia layer, creating a pitting site which can lead to local cladding embrittlement [SIDKY, 1998].



Both radiolytically dissociated iodine from CsI and  $\text{ZrI}_4$ , produced during the *van-Arkel-de-Boer reaction* can lead to ISCC and affect the integrity of the cladding at temperatures in the range of 300 to 400 °C [HOFMANN AND SPINO, 1983; KAUFMANN, 1988; SIDKY, 1998].

## **3 Chlorine-36 and iodine-129**

Volatile fission and activation products present in SNF pellets, cladding and adjacent reactor materials display a potential safety hazard for the disposal of high radioactive waste concerning their mobility and lack of retention capability in the host rock of a geological repository. Amongst the numerous RN produced, either directly by nuclear fission or indirectly by neutron activation of stable isotopes, Cl-36 and I-129 are two of the most crucial nuclei regarding their radiotoxicity and ability to reach the biosphere in the long-term after a potential breaching combined with water ingress to the SNF disposal container.

### **3.1 Chlorine-36**

Cl-36 is a RN with a half-life of approximately  $3.01 \times 10^5$  years and a natural abundance of  $7 \times 10^{-13}$  % regarding the two non-radioactive chlorine isotopes, Cl-35 (75.77 %) and Cl-37 (24.23 %). It is produced naturally in negligible amount during spallation reactions in the upper atmosphere by the reaction of Ar-40 with high energetic protons and emission of an alpha particle (equation (3.1)) or by the reaction of Ar-36 with neutrons (equation (3.2)). Moreover, Cl-36 is produced in a nuclear reactor by neutron capture of Cl-35 under

emission of a  $\gamma$ -quant due to impurities in the nuclear fuel, cladding and reactor components as shown in equation (3.3). Two other routes of Cl-36 production in the reactor are possible regarding the direct activation of K-39 with emission of an alpha particle to Cl-36 or by activation of S-34 to S-35 with subsequent  $\beta^-$ -decay to the precursor isotope Cl-35 [BROWN *ET AL.*, 1999].

Cl-35 has a relatively high cross-section of 46.63 barn for (n, $\gamma$ ) reactions, which leads to a significant amount of produced Cl-36 during reactor operation [HUMMEL, 2017]. Moreover, atmospheric concentrations of Cl-36 rose significantly starting from the 1950s due to extensive atmospheric nuclear weapon testing worldwide [DEWAYNE CECIL AND VOGT, 1997].



Generation of Cl-36 in SNF and the Zircaloy cladding occurs almost solely due to Cl-35 impurities within the initial material. The amount of Cl-35 in the fuel assembly and UO<sub>2</sub> pellets, which will be later activated to Cl-36 via neutron capture (see equation (3.3)) displays a large uncertainty. According to ORIGEN2 calculations, Guenther et al. give a maximum Cl impurity of < 5 ppm for the fuel [GUENTHER *ET AL.*, 1988]. For Zry-4, values of the determined chlorine impurities are scarce. Tait and Theaker refer to the impurities in Zry-2.5Nb, which are in the range of 5 ppm and regarded as typical impurities in Zry-4 alloy as well [TAIT AND THEAKER, 1996].

Chlorine impurities in the cladding are introduced as trace elements during the manufacturing process of zirconium alloys for pressure tubes, e.g. Zry-2, Zry-4 and Zry-2.5Nb, which is based on the so-called *Kroll process*. Hereby, according to equation (3.4), magnesium chloride is formed as secondary product through reduction of  $ZrCl_4$  with elemental Mg:



This magnesium chloride is regarded as the main chlorine source for impurities within the cladding tube [THEAKER *ET AL.*, 1994]. Typical impurity values of  $MgCl_2$  for Zry-4 and Zry-1.0Nb are given in [NIKULINA AND MALGIN, 2008] with  $< 5$  ppm and  $< 7$  ppm, respectively.

For CanDU (Canada Deuterium Uranium) fuel, Sheppard and co-workers as well as Aitchison and Davies give a maximum impurity within both, the fuel and Zircaloy, of  $< 5$  ppm [AITCHISON AND DAVIES, 1993; SHEPPARD *ET AL.*, 1996]. For unirradiated CANDU fuel, Tait and co-workers give a value of  $2.3 \pm 1.1$  ppm [TAIT *ET AL.*, 1997]. For the irradiated fuel, Tait and co-workers state  $4.22 \cdot 10^2$  Bq/g<sub>U</sub> as calculated inventory with a burn-up of 190 GWh/t<sub>HM</sub> and 5 ppm initial Cl impurity. According to them, production of Cl-36 within the fuel is related to the neutron flux and thus also the burn-up, resulting in an average value of  $1.5 \pm 1.1$  ppm for used CanDU fuel [TAIT *ET AL.*, 1997].

Regarding the leachable fraction of Cl-36, i.e. the instantaneous release upon first contact with groundwater, originating from a breached SNF rod, Tait and colleagues stated that Cl-36 release from the fuel to the solution is depending on the experienced linear power rating of the irradiated material and comparable to the release behaviour of I-129 from the gap [TAIT *ET AL.*, 1997].

More recent values for Cl impurities within the Zircaloy-4 cladding of nuclear fuel rods are given by Caruso and summarised by Häkkinen with an upper limit of 20 ppm [CARUSO, 2016; HÄKKINEN, 2019].

## 3.2 Iodine-129

I-129 is a long-lived isotope with a half-life of  $1.57 \times 10^7$  years, formed via fission processes in the nature (Oklo natural reactor, Gabun), neutron capture of tellurium isotopes with subsequent  $\beta^-$  decay or the interaction of cosmic radiation with xenon in the upper atmosphere [MARTIN *ET AL.*, 1990]. Yet, the most governing source for I-129 is of anthropogenic nature, e.g. fission reactors and extensive atmospheric nuclear weapon testing in the past. In nuclear power reactors, iodine is produced by the fission reaction of U-235 or Pu-239. Moreover, iodine is released into the off-gas system of reprocessing facilities during the dissolution of SNF rods. For instance,  $10^{12}$  Bq I-129 have been released annually from the La Hague reprocessing plant into the Atlantic Ocean since the year 2000 [REITHMEIER *ET AL.*, 2006; TOSCH, 2010]. In some reprocessing plants, iodine is retained to large extent in high-efficiency-particulate-air filters, retaining it in a resin matrix for immobilisation and preventing the release into the environment.

Whilst most of the radioactive iodine isotopes will decay off within less than two years, e.g. I-125 ( $t_{1/2} = 59.41$  d), I-131 ( $t_{1/2} = 8.03$  d), only I-129 displays a potential hazard for safety assessment studies of geological repositories, owed to the poor retention of iodine species within the different barriers, i.e. technical, geotechnical and host rock. Due to its longevity, mobility, lack of retardation in most lithologies and biological accumulation it is regarded as one of the main dose-contributing radionuclides within SNF [GRAMBOW, 2008; HUMMEL, 2017].

As stated above, the main source for I-129 is the fission of UO<sub>2</sub> or MOX fuel in commercial nuclear power reactors. It is produced by fission of U-235 or Pu-239 with yields of 0.71 % and 1.41 %, <sup>11</sup> respectively. As for every long-lived fission nuclei, the activity concentration of I-129 also correlates with the burn-up of the fuel [NEEB, 1997].

---

<sup>11</sup> These values refer to the thermal, neutron induced fission of the respective nuclei.

The chemical behaviour of iodine in LWR fuel rods has been subject to extensive research in the past. The distribution of the produced iodine is almost equally in all regions of the fuel, yet regarding the mobility of iodine due to temperature and activity gradients local concentration maxima occur [PEEHS *ET AL.*, 1981]. Elevated iodine concentrations are reported upon the cladding near pellet fracture locations, in the chemical form of CsI precipitates [CUBICCIOTTI AND SANECKI, 1978; KLEYKAMP, 1985].

### **3.3 Cl-36 and I-129 in terms of repository safety aspects**

With groundwater access due to container breach of the SNF containment in a DGR, the Zircaloy cladding will corrode, eventually releasing the radionuclides denoted as the AFI (see section 2.1.2) and consecutive RN migration from the SNF matrix degradation occurs in the near-field of the DGR. Both radionuclides, Cl-36 and I-129, are hereby of great significance due to their anionic and long-term dose rate dominating behaviour in the evaluation of repository concepts [GRAMBOW, 2008; HUMMEL, 2017].

In reference and most alternative scenarios of long-term assessments of HLW disposal systems, most of the more radiotoxic actinides are expected to be retarded within a few meters of the near-field owing to their low mobility in different repository relevant lithologies. As a consequence for long-term safety assessments for DGRs, the retardation of the relatively mobile long-lived anionic species such as Cl-36 and I-129 is of considerable relevance and, to some extent, still an open question to be answered [GRAMBOW, 2008; GECKEIS *ET AL.*, 2012].

In most assessments, very little retention values are assumed for the two radionuclides. Yet, regarding the immense migration distance from the waste package through the

barrier system and lithology towards the biosphere, even small retention values can have an impact on the retardation of Cs-136 and I-129 as proven by experiments with layered double hydroxides by Aimoz and colleagues and, more recent, by Platte and co-workers [GRAMBOW, 2008; AIMOZ, KULIK, *ET AL.*, 2012; AIMOZ, TAVIOT-GUÉHO, *ET AL.*, 2012; AIMOZ, WIELAND, *ET AL.*, 2012; PLATTE *ET AL.*, 2021].

## **4 Materials and methods**

### **4.1 Chemicals and radionuclides used in this work**

#### **4.1.1 Chemicals**

All solutions in this work were prepared with ultrapure water purified by a MilliQ<sup>®</sup> A10 system (Merck Millipore, 18.2 MΩ·cm,  $T = 22 \pm 2$  °C, pore size: 0.22 μm, < 4 ppb TOC). The chemicals utilised in this work are listed in table 4.1. All chemicals were used without further purification.

## Materials and methods

**Table 4.1:** Chemicals used in this work.

<b>chemical name</b>	<b>chemical formula</b>	<b>molar weight [g/mol]</b>	<b>manufacturer</b>	<b>grade</b>
<b>ammonia solution (25 %)</b>	NH <sub>4</sub> OH	35.0	Merck	a. g.
<b>ammonium carbonate</b>	(NH <sub>4</sub> ) <sub>2</sub> CO <sub>3</sub>	79.1	Merck	ACS
<b>ammonium molybdophosphate</b>	(NH <sub>4</sub> ) <sub>3</sub> P(Mo <sub>3</sub> O <sub>10</sub> ) <sub>4</sub>	1876.4	Bio-Rad Laboratories	a. g.
<b>caesium chloride</b>	CsCl	168.4	Merck	a. g.
<b>caesium iodide</b>	CsI	259.8	Alfa Aesar	a. g.
<b>hydrochloric acid</b>	HCl	36.5	Merck	a. g.
<b>hydrofluoric acid</b>	HF	20.0	Merck	suprapur <sup>®</sup>
<b>hydrogen peroxide</b>	H <sub>2</sub> O <sub>2</sub>	34.0	Merck	a. g.
<b>isopropanol</b>	C <sub>3</sub> H <sub>8</sub> O	60.1	Merck	ACS
<b>nitric acid</b>	HNO <sub>3</sub>	63.0	VWR chemicals	a. g.
<b>silver nitrate</b>	AgNO <sub>3</sub>	169.9	Merck	a. g.
<b>sodium carbonate</b>	Na <sub>2</sub> CO <sub>3</sub>	105.9	VWR chemicals	a. g.
<b>sodium hydroxide (1 M)</b>	NaOH	40.0	Merck	suprapur <sup>®</sup>
<b>sodium chloride</b>	NaCl	58.4	VWR chemicals	ACS
<b>sodium nitrite</b>	NaNO <sub>2</sub>	69.0	Merck	a. g.
<b>sodium sulfite</b>	Na <sub>2</sub> SO <sub>3</sub>	126.0	Merck	a. g.
<b>sulphuric acid (96 – 97 %)</b>	H <sub>2</sub> SO <sub>4</sub>	98.1	Merck	suprapur <sup>®</sup>
<b>toluene</b>	C <sub>7</sub> H <sub>8</sub>	92.1	Merck	ACS

## 4.1.2 CI-36 standardised solutions used for quench and recovery tests

Standardised reference material solutions of CI-36 with an initial activity concentration of 3.7 MBq/mL in NaCl were obtained by Eckert & Ziegler Nuclitec GmbH. Recovery and quenching tests were performed by use of defined aliquots of the CI-36 bearing solution. Figure 4.1 shows the LSC spectrum of the unquenched reference material.

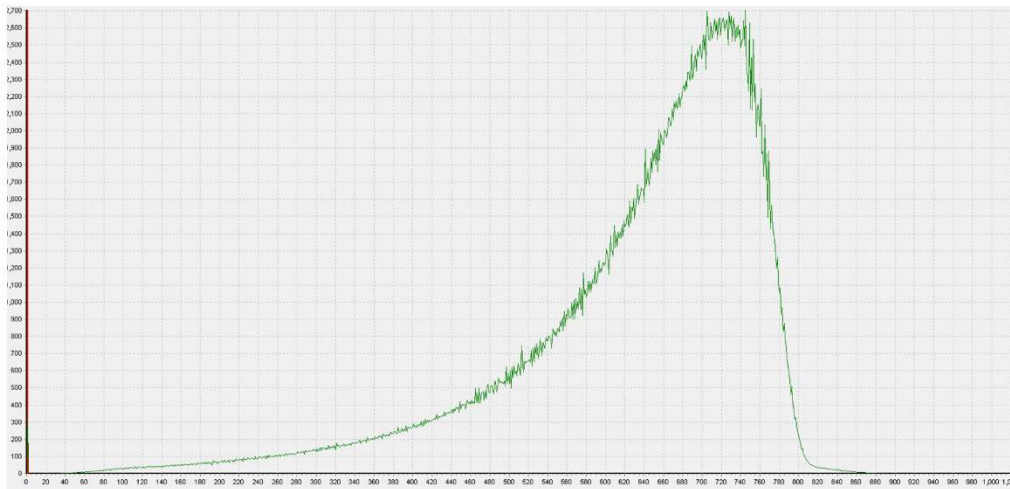


**Figure 4.1:** LSC spectrum of CI-36 standard reference material displayed as frequency of impulses as a function of channel number.

### 4.1.3 I-129 standardised solutions used for quench and recovery tests

For I-129 quenching and recovery tests, a standardised beta solution with an activity concentration of 370 kBq/mL I-129 in NaOH was obtained by Eckert & Ziegler Nuclitec GmbH. Purity of the standardised solution was > 99 % with a minor initial impurity of Cs-137 in the range of 0.0182 %. Figure 4.2 depicts the LSC spectrum of the I-129 reference material.



**Figure 4.2:** LSC spectrum of I-129 standard reference material displayed as frequency of impulses as a function of channel number.

## 4.2 Spent fuel samples origin and treatment

Within the frame of this work, two different types of SNF specimens were examined. Both fuel types were irradiated in commercial PWRs during the 1980s for electricity generation with cooling times exceeding 30 years. In the following two subsections, the fuel data, irradiation history and reactor specification concerning the respective fuel types are further explained. Since the characteristics of SNF, and also the amount and variety of generated fission products, are largely depending on the fuel burn-up, linear average power and possible ramping during reactor operation, special focus needs to be set on these parameters.

### 4.2.1 UO<sub>x</sub> fuel

The examined spent UO<sub>x</sub> fuel was sampled from the fuel rod segment N0204 of the fuel rod SBS1108, which was irradiated for four cycles in the nuclear power plant Gösgen (KKG, Switzerland). The final discharge from the reactor took place in May 1989 with an average rod burn-up of 50.4 GWd/t<sub>HM</sub>. The UO<sub>x</sub> fuel was fabricated by former Kraftwerk Union AG (KWU, today Framatome) with an initial enrichment of 3.8 % U-235, except for two natural UO<sub>x</sub> pellets at the top and bottom of the fuel segment with an U-235 content of 0.7 %, respectively. The cladding consists of Zry-4 and the fuel was fabricated using a NIKUSI sintering process, which is a fast sintering process at a temperature below conventional UO<sub>x</sub> pellet manufacturing processes [STRATTON *ET AL.*, 1991]. Characteristics and irradiation data of the fuel rod, conducted in the EURATOM FP7 collaborative project “Fast / Instant Release of Safety Relevant Radionuclides from Spent Nuclear Fuel (FIRST-Nuclides)” by the Joint Research Centre Karlsruhe and KIT-INE, are given in table 4.2. The fuel rod segment N0204 is shown in figure 4.3.

**Table 4.2:** Characteristics and irradiation data of the UO<sub>x</sub> fuel rod SBS1108 [METZ *ET AL.*, 2013].

Reactor	PWR Gösgen, Switzerland
Fuel data	UO <sub>x</sub> fuel with 3.8 % enrichment of U-235 Pellet length = 11.0 mm Pellet radius = 9.35 mm O / U ratio = 2.002 Density = 10.41 g/cm <sup>3</sup>
Cladding data	Zircaloy-4 Wall thickness: 0.75 mm
Irradiation data	Average burn-up: 50.4 GWd/t <sub>HM</sub> Number of cycles: 4 Average linear power: 260 W/cm Maximal linear power: 340 W/cm Date of discharge: 27.05.1989 Irradiation duration: 1226 days

KKG is operated with a fuel assembly lattice of 15 × 15 rods. In total 225 positions are available for nuclear fuel rod placement with 205 of them occupied by the fuel rods and 20 positions used for control rods usually consisting of neutron absorbing materials e.g. Ag-In-Cd alloys [KERNKRAFTWERK GÖSGEN, 2010]. The fuel rod SBS1108 was irradiated in central position of the 15x15 lattice.

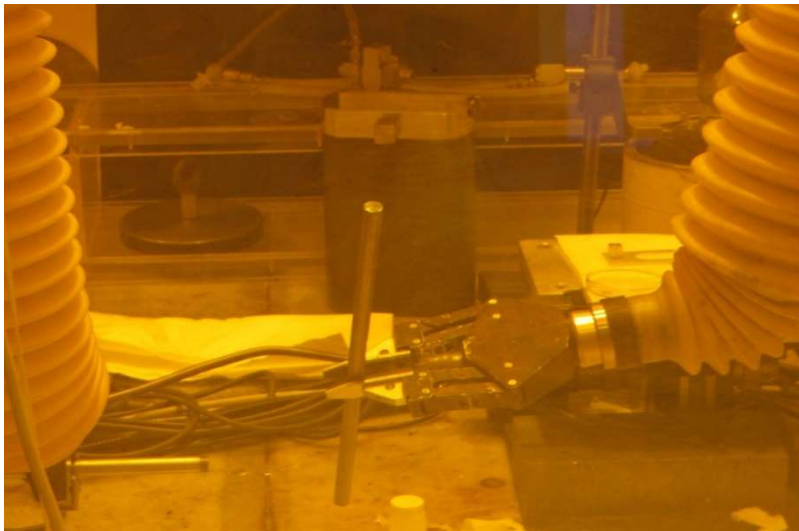


**Figure 4.3:** High burn-up UO<sub>x</sub> fuel rod segment N0204 of fuel rod SBS 1108 irradiated in the nuclear power plant KKG.

## 4.2.2 MOX fuel

The studied MOX fuel sample was obtained from the fuel rod 5810 of the fuel element 14.28 and was irradiated for 1157 days in the nuclear power plant of Obrigheim (KWO, Germany) with an average burn-up of 38.0 GWd/t<sub>HM</sub><sup>12</sup>. Discharge of the fuel rod took place in May 1986. The MOX fuel consisted of a UO<sub>x</sub> (nat.) matrix with an initial enrichment of 3.2 % plutonium manufactured by the optimised co-milling process (OCOM). After a cooling time of 31 years the fuel segment was cut and characterised at KIT-INE for the EURATOM Horizon2020 project “Modern Spent Fuel Dissolution and Chemistry in Failed Container Conditions” (DisCo) [GONZÁLEZ-ROBLES *ET AL.*, 2018]. The characteristics and irradiation data of the examined MOX fuel are given in table 4.3. The MOX fuel rod segment of fuel rod 5810 is shown in figure 4.4.

**Table 4.3:** Characteristics and irradiation data of the MOX fuel rod 5810 [GOLL *ET AL.*, 1988; GONZÁLEZ-ROBLES *ET AL.*, 2018].

Reactor	PWR Obrigheim, Germany
Fuel data	MOX fuel with 3.2 % Pu enrichment Pellet length = 11.0 mm Pellet radius = 9.08 mm O / M ratio = 1.99 Density = 10.36 g/cm <sup>3</sup>
Cladding data	Zircaloy-4 Wall thickness: 0.65 mm
Irradiation data	Average burn-up: 38.0 GWd/t <sub>HM</sub> Number of cycles: 4 Average linear power: 200 W/cm Date of discharge: 31.05.1986 Irradiation duration: 1157 days

<sup>12</sup> KWO was shut down in May 2015 as a result of the German nuclear power phase-out act of 2011 [BUNDESGESETZBLATT, 2011].

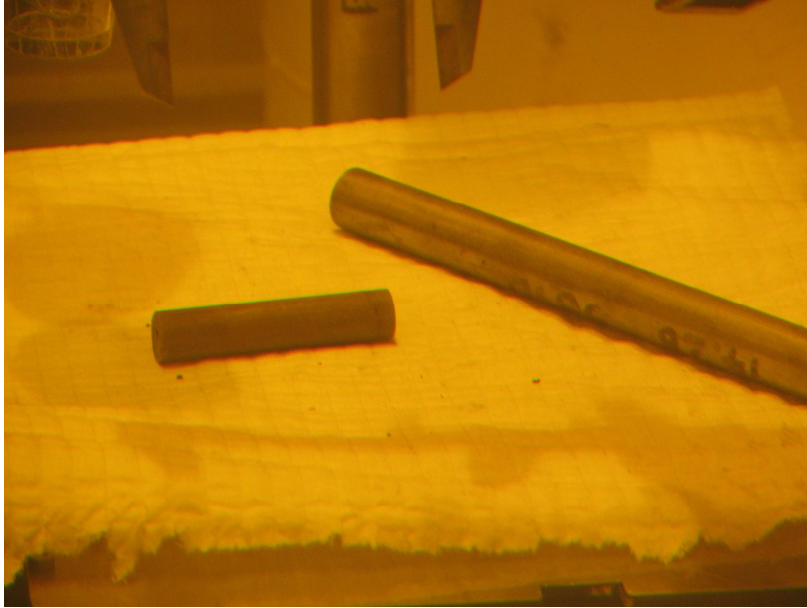


**Figure 4.4:** MOX fuel rod segment of the fuel rod 5810 used for inventory and spectroscopic analysis.

In total 196 positions were available for fuel rod placement, with 16 of them occupied by neutron absorbing control rods. The MOX fuel rod 5810, from which the sample was taken, had been irradiated in central position (F7) within the  $14 \times 14$  lattice of the KWO MOX assembly [GOLL *ET AL.*, 1988].

### 4.2.3 Preparation of the irradiated fuel samples

UO<sub>x</sub> and MOX specimens were cut from the respective fuel rods in the hot cell facility of KIT-INE using a low speed saw (IsoMet, 11-1180, Buehler Ltd.) with a diamond cutting disc (IsoMet, 15LC, Buehler Ltd.) by remote handling. In order to minimise any possible damage of the cladding and fuel as well as mitigating further oxidation, the cutting was performed with moderate speed (cutting times were in the range of 30 minutes per sample). From each rod an approximately 2 mm thick disk was cut in order to enable

a selective defueling of the samples. The cutting and preparation process for the irradiated  $\text{UO}_x$  and MOX fuel is illustrated in figures 4.5 and 4.6, respectively.

After cutting, the dose rates of the respective fuel specimens were determined with a probe inside the hot cell (6150AD-15/E, Automation und Messtechnik, Ladenburg, Germany) and a dose rate meter (6150AD, Automation und Messtechnik, Ladenburg, Germany) connected via wire to the interior of the cell.  $\gamma$  dose rates of the  $\text{UO}_x$  and MOX fuel disks were in the range of approximately 1.5 Sv/h. For spectroscopic and radiochemical examinations, subsamples were taken from the designated fuel disks (see section 4.2.4 and 4.6).

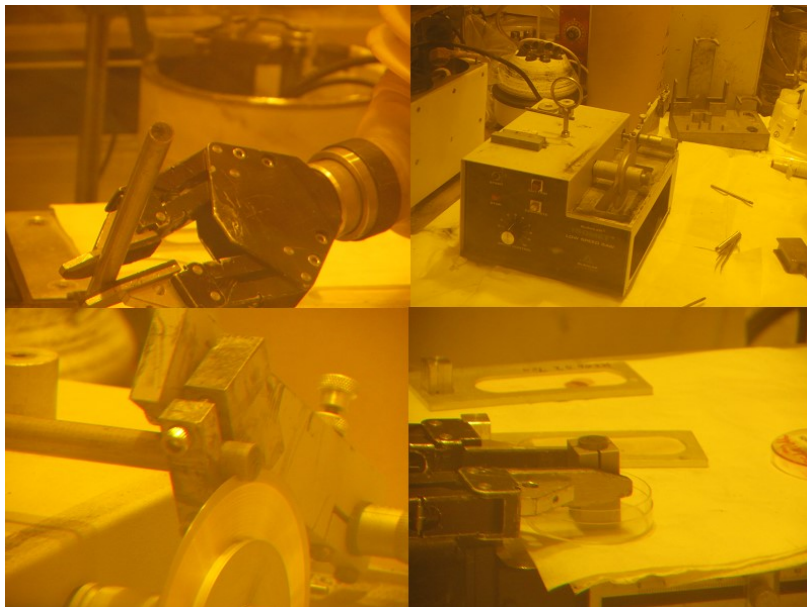


**Figure 4.5:** Cutting and preparation process for the  $\text{UO}_x$  specimen. Upper left picture shows the fuel rod segment N0204 of fuel rod SBS1108. Upper right picture features the low speed saw used for cutting the specimen from the fuel rod segment. Lower left picture displays the cutting process of the 2.4 mm diameter SNF disk. Lower right picture shows the 2.4 mm diameter SNF disk prior to defueling (see section 4.2.4).

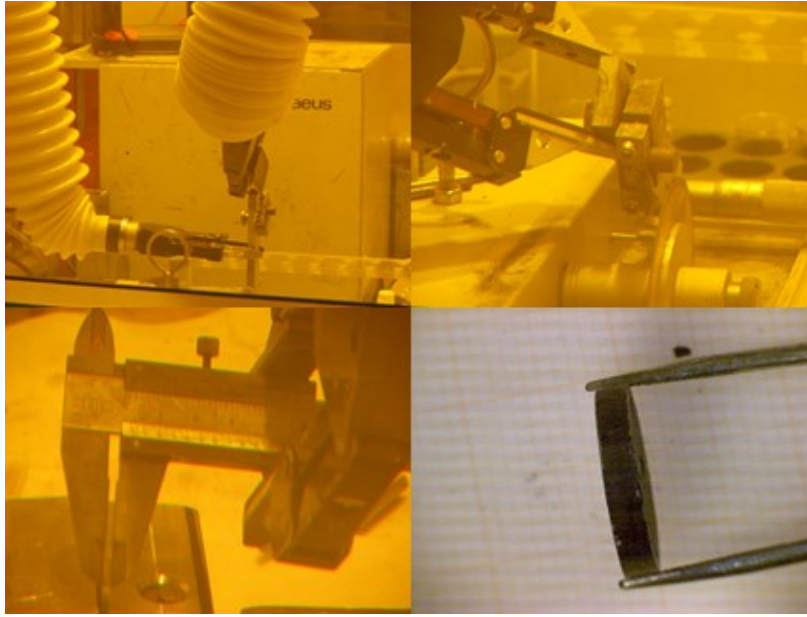


**Figure 4.6:** Cutting and preparation process of the MOX fuel sample. Upper left and right pictures depict the cutting process of the fuel disk from the fuel rod specimen KWO 5810. Lower left and right pictures show the dimensions of the cut fuel disk.

### **4.2.4 Sampling of high active specimens for radionuclide inventory analysis in fuel, cladding and fuel-cladding interface layer**

Fuel fragments and Zircaloy cladding with fuel residue of the spent  $\text{UO}_x$  and MOX fuels (see section 4.2.1 – 4.2.3) have been prepared in order to digest the respective specimens under either acidic or alkaline conditions. Defueling of the specimens was carried out by removing the fuel with a punch to obtain fuel fragments from the central region of the SNF disk at first. In a second step, the fuel still attached to the inner side of the cladding was carefully detached by means of a pick and scalpel. Received fuel fragments were stored separately in acrylic glass vessels under air in the hot cell. Furthermore, the Zircaloy cladding with fuel residue still attached to its inner facing side was sectioned by

use of a saw equipped with a saw blade designated for metals as well as by use of a cutting pincer. Figure 4.7 and 4.8 show the dimensions and defueling of the 2.4 mm disk of the high burn-up  $\text{UO}_x$  fuel, previously cut from the fuel rod segment (see section 4.2.3).



**Figure 4.7:** Pictures and dimension of the  $\text{UO}_x$  fuel segment used for inventory determination and spectroscopic analysis. The left picture shows the thickness of the cut fuel disk. The right picture shows the fractured surface of the irradiated fuel.



**Figure 4.8:** Defueling process of the high burn-up  $\text{UO}_x$  fuel. Upper left picture shows the segment with the central region already selectively defueled. Upper right and lower left picture feature the Zircaloy ring with fuel residue attached to it. Lower right picture shows the fragments obtained as a result of the defueling process.

### 4.3 Digestion of the irradiated fuel samples

For radionuclide inventory determination of the SNF, fuel and cladding specimens were taken from the respective fuel sample in order to be digested under acidic or alkaline conditions in either 3 % HF and 16 % H<sub>2</sub>SO<sub>4</sub>, *aqua regia* or saturated (NH<sub>4</sub>)<sub>2</sub>CO<sub>3</sub> and 30 % H<sub>2</sub>O<sub>2</sub> (see figure 4.9). The latter chemicals were chosen as a mild digestion mixture in order to prevent the loss of iodine during the dissolution process of the fuel matrix.

Fuel fragments of the UO<sub>x</sub> (0.017 ± 0.001 g for the rim specimen and 0.040 ± 0.001 g for the core specimen) and MOX (0.032 ± 0.001 g for the rim specimen and 0.026 ± 0.001 g for the core specimen) fuel were digested in a mixture of 14 M HNO<sub>3</sub> (2.5 mL) and 13 M HCl (7.5 mL) for approximately 30 minutes in a glass beaker located inside the hot cell. After the acidic digestion, no residue of undissolved material was apparent. In order to mitigate the dose rate and obtain solutions for subsequent radionuclide inventory determination, the digestion liquors were diluted with 1 M HNO<sub>3</sub> by a factor of 1:100<sup>13</sup>. Complementary to the acidic digestion, fuel fragments of both fuel types from the rim area (0.028 ± 0.001 g and 0.055 ± 0.001 g for UO<sub>x</sub> and MOX, respectively) were almost completely dissolved under alkaline conditions in a solution of saturated (NH<sub>4</sub>)<sub>2</sub>CO<sub>3</sub> (100 mL) and 30 % H<sub>2</sub>O<sub>2</sub> (50 mL) for five days with stirring<sup>14</sup>. This method for the digestion of SNF is similar to a standardised manufacturing process for the conversion of UF<sub>6</sub> to UO<sub>2</sub> in order to produce sinterable nuclear fuel pellets and described in [SODERQUIST AND HANSON, 2010; SODERQUIST *ET AL.*, 2011]. For additional fission gas analysis, one fragment of the UO<sub>x</sub> fuel (0.031 ± 0.001 g) was digested in 30 mL sat. (NH<sub>4</sub>)<sub>2</sub>CO<sub>3</sub> and 20 mL 30 % H<sub>2</sub>O<sub>2</sub> in a stainless steel autoclave (Berghof Products and

---

<sup>13</sup> This digestion method was previously described in report *Chemical reaction of fabricated and high burn-up spent UO<sub>2</sub> fuel with saline brines* [GRAMBOW *ET AL.*, 1996]. Dilution of the digestion liquor is necessary in order to lower the dose rate.

<sup>14</sup> Residues from the alkaline digestion process are consisting of undissolved noble metals, e.g. Tc, Ru, Rh, and Pd.

Instruments GmbH, Eningen unter Achalm, Germany) equipped with a titanium liner and titanium lid under room temperature, initial ambient pressure and continuous stirring. In order to prevent air intrusion into the autoclave, the respective solutions were previously prepared in an inert gas argon glove box and transported to the hot cell in sealed syringes equipped with two-way valves. Introduction of the solutions into the autoclave was performed under argon flux. Once the dissolution reaction was finished after five days, a single-ended gas sampling cylinder (SS-4CS-TW-50, Swagelok, USA) was connected to the back side of the hot cell and the gas phase from the autoclave extracted and analysed by means of gas mass spectrometry (see figure 4.10).

Digestion of the cladding samples was performed under acidic conditions by use of a mixture (30 mL) containing 3 % HF and 16 % H<sub>2</sub>SO<sub>4</sub>, which dissolved the Zircaloy specimens readily over the course of 20 minutes accompanied by the evolution of hydrogen gas and leaving a non-dissolvable thin layer of ZrO<sub>2</sub>. Dissolution reactions of the respective Zircaloy segments (denoted as Zry-UO<sub>x</sub> and Zry-MOX) previously in contact with fuel were performed outside of the hot cell in a ventilated isotope fume hood due to the moderate dose rate of the sample within the range of 240 – 350 μSv/h. The masses of the Zircaloy specimens amounted to 0.051 ± 0.001 g for the Zircaloy cladding previously in contact with the high burn-up UO<sub>x</sub> fuel as well as 0.045 ± 0.001 g for the cladding segment of the MOX fuel.

Details on masses, dose rates and initial location in the SNF pellet of the specific samples are summarised in table 4.4.

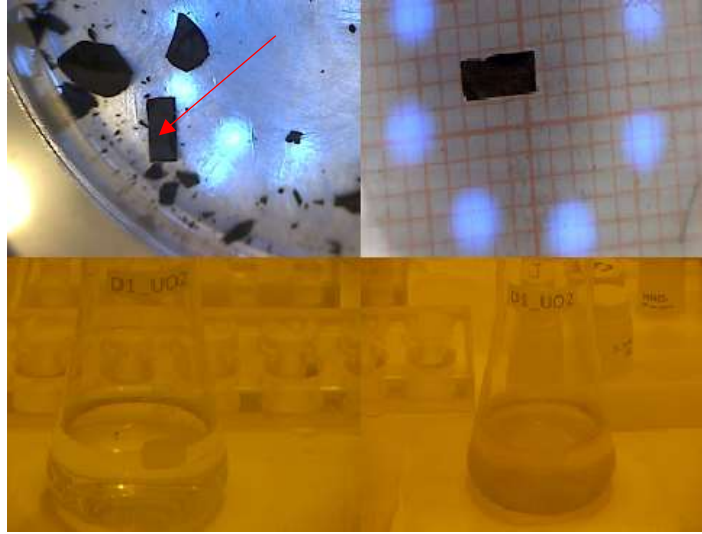


**Figure 4.9:** Fragment selection and alkaline digestion process of the  $\text{UO}_x$  fuel specimen. The upper pictures show the selected fragment from the defueled fuel segment. Lower left picture depicts the digestion process at the beginning of digestion; the lower right picture shows the resulting yellowish solution (colours are difficult to see through the lead windows of the hot cell) after digestion. The yellow colour of the solution is due to the formation of uranyl carbonates.



**Figure 4.10:** Fragment and material for gas phase analysis. Upper left picture features the  $\text{UO}_x$  fuel fragment used for fission gas analysis. Upper right picture shows the titanium liner later containing the specimen and solution. Lower left picture shows the SS-4CS-TW-50 gas sampling cylinder in detail and lower right picture depicts the reaction vessel equipped with a manometer and gas sampling connection.

**Table 4.4:** Masses, dose rate and initial location within the SNF specimen of the samples used for inventory analysis.

Sample	UO <sub>x_acd</sub>	UO <sub>x_acd</sub>	UO <sub>x_alk</sub>	MOX_acd	MOX_alk	UO <sub>x_gas</sub>	Zry-UO <sub>x</sub>	Zry-MOX
<b>mass</b> [g]	0.017 ± 0.001	0.040 ± 0.001	0.028 ± 0.001	0.032 ± 0.001	0.026 ± 0.001	0.055 ± 0.001	0.031 ± 0.001	0.051 ± 0.001
<b>dose rate</b> [mSv/h] <sup>a)</sup>	14.7	30.8	21.6	34.1	23.7	42.3	n. d.	0.24
<b>area</b> <sup>b)</sup>	rim	core	rim	rim	core	rim	rim	cladding
<b>digestion</b> <b>mixture</b>	HNO <sub>3</sub> HCl	HNO <sub>3</sub> HCl	(NH <sub>4</sub> ) <sub>2</sub> CO <sub>3</sub> H <sub>2</sub> O <sub>2</sub>	HNO <sub>3</sub> HCl	HNO <sub>3</sub> HCl	(NH <sub>4</sub> ) <sub>2</sub> CO <sub>3</sub> H <sub>2</sub> O <sub>2</sub>	(NH <sub>4</sub> ) <sub>2</sub> CO <sub>3</sub> H <sub>2</sub> O <sub>2</sub>	HF H <sub>2</sub> SO <sub>4</sub>

a): Gamma dose rate of the respective specimens. For fuel fragments, the dose rate was determined inside the hot cell with a gamma probe; for cladding segments, dose rate measurements were performed outside of the hot cell in a ventilated fume hood.

b): Area refers to the initial position in the pellet where the sample was selectively extracted from.

## **4.4 Radionuclide inventory determination and separation method for Cl-36 and I-129**

The Cl-36 and I-129 separation technique adapted for SNF specimen in this work is based on two separation methods previously reported in the literature by Hou and co-workers as well as Geckeis and colleagues [GECKEIS *ET AL.*, 1995; HOU *ET AL.*, 2007; HOU, 2018]. The analytical procedure outlined by Geckeis and co-workers was utilised for the determination of various radionuclides in halite-bearing leaching liquors of SNF specimen and describes the in-hot cell separation steps for I-129. The method described by Hou and colleagues was designed for the determination of Cl-36 and I-129 in nuclear waste arising from the decommissioning of reactor components e.g. steel, graphite and cement and adapted for the separation of the halogen isotopes in spent fuel and Zircaloy cladding digestion liquors and leaching solutions. Moreover, in order to determine the radionuclide inventory in the various sample solutions, a combination of different analytical methods was applied to the respective solutions.

### **4.4.1 Experimental set-up of the Cl-36 and I-129 separation method**

The experimental procedure for the separation method for Cl-36 and I-129 is outlined in figure 4.11 featuring a previous digestion or leaching of the high-active waste sample e.g. fuel or cladding specimens (see section 4.3) followed by either a dilution of the resulting

solution<sup>15</sup> in conjunction with the addition of an inactive carrier or advancing to the next step.

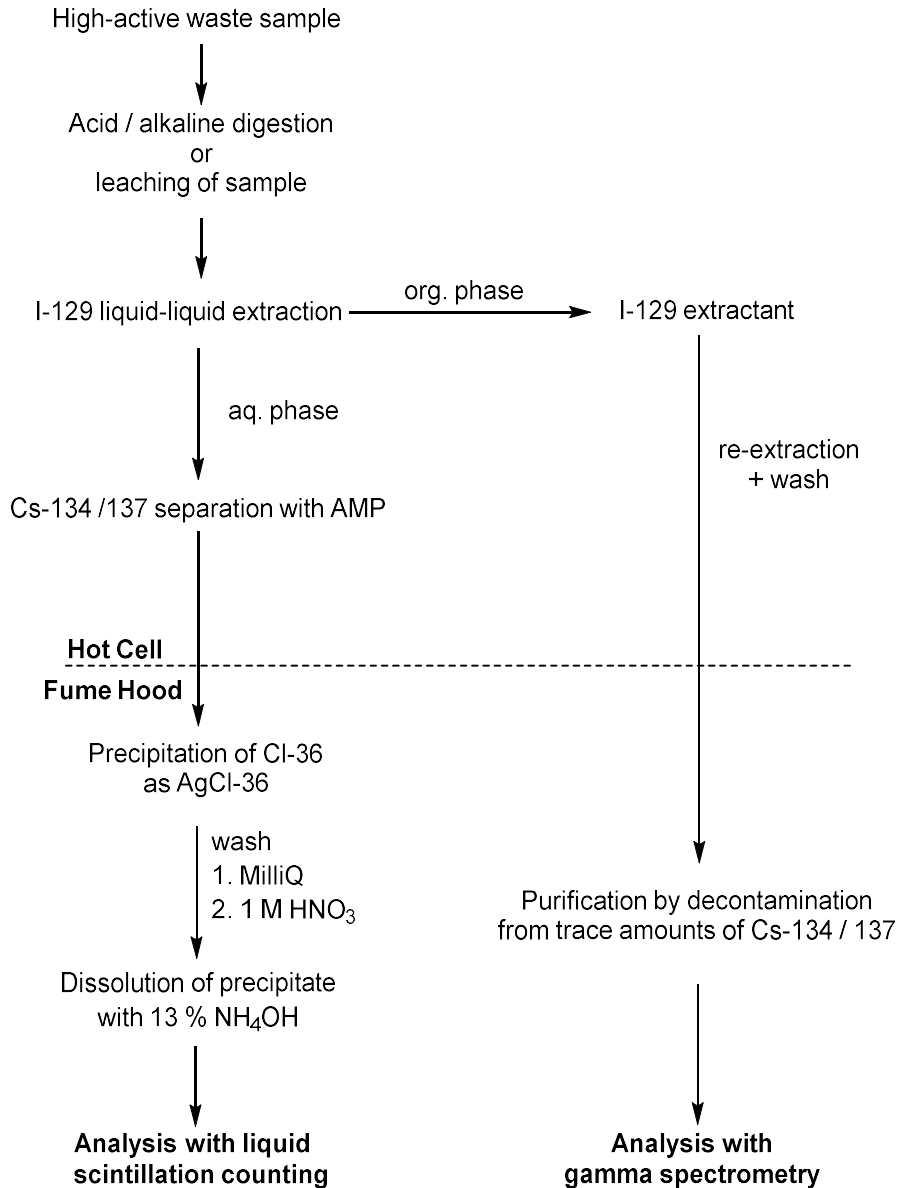


**Figure 4.11:** Experimental procedure of the Cl-36 and I-129 separation method.

<sup>15</sup> For some samples, a dilution step was preferred in order to decrease the dose rate and reduce the activity of some isotopes e.g. Cs-137 to minimise dead time of the analytical devices used after separation.

## Materials and methods

---

To separate I-129<sup>16</sup> from the solution, a liquid-liquid extraction was performed with a 2 mL aliquot of the solution to be analysed. In the first step, 0.3 mL of 2 M Na<sub>2</sub>SO<sub>3</sub> was added to the sample solution in order to ensure that iodine is reduced to iodide followed by shaking for approximately 15 minutes. Subsequently, the sample was acidified with 2 mL of 2 M H<sub>2</sub>SO<sub>4</sub><sup>17</sup> and shaken for additional five minutes. 2 mL of toluene was added to the reaction vial and the phases were separated over the course of five minutes. To oxidise the iodide to elemental I<sub>2</sub> 1 mL of 2 M NaNO<sub>2</sub> was added and I-129 gathered in the organic phase which turned to purple over the course of 5 minutes (colours are difficult to determine through the yellow hot cell windows, see figure 4.12). After separation of the aqueous and organic phase, a 1 mL aliquot of the organic phase was taken and transferred into a new reaction vial. The organic phase was stripped from the elemental iodine by means of the addition of 0.3 mL 2 M Na<sub>2</sub>SO<sub>3</sub> in order to reduce iodine to iodide again, as well as acidified with 4 mL of 2 M H<sub>2</sub>SO<sub>4</sub> as depicted in figure 4.13. The resulting I-129 bearing solutions with dose rates below 20 µSv/h were separated from the organic phase and taken out of the hot cell, the solution recovered from the vials by sampling them through a septum with a cannula and syringe and transferred into a new, contamination-free vial. To purify the solutions from caesium trace contaminants which would render the analysis by gamma spectroscopy impossible due to the high Compton background, Cs isotopes were separated by means of precipitation with 0.05 g ammonium molybdophosphate (AMP) without further acidification by nitric acid and subsequent filtration with a 0.45 µm syringe filter. Eventually, the resulting iodine-bearing solution was prepared for analysis.

---

<sup>16</sup> In addition to I-129 as long-lived iodine isotope, stable I-127 is also produced during nuclear fission resulting in a ratio of I-127 / I-129 of 23.5 % / 76.5 % two years after discharge [RILEY *ET AL.*, 2016]. Other iodine isotopes, e.g. I-125 ( $t_{1/2} = 59.4$  d) or I-131 ( $t_{1/2} = 8.6$  min) had already decayed during the cooling time of the nuclear fuel.

<sup>17</sup> The reader should be notified that, depending on the digestion liquor or leaching solution in which the SNF specimen was treated, the adjusting of acidity is one of the most crucial aspects, hence if the acid concentration is too low, not all iodide can be oxidised to iodine as already explained by Geckeis and co-workers [GECKEIS *ET AL.*, 1995].

Due to the extraction of iodine in toluene, interferences from other RNs in large excess such as Sr-90 and Cs-134 / 137 as well as the matrix constituents, i.e. U-238 and Pu-239 for the SNF solutions and Zr-93 for the cladding digestion liquors, are effectively prevented.

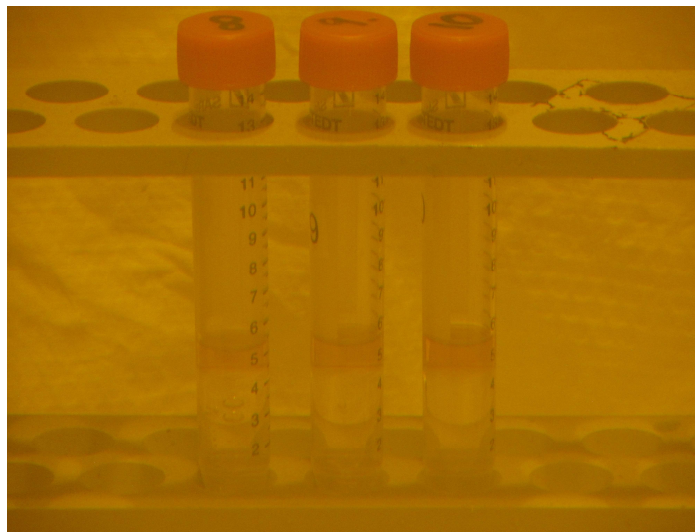


**Figure 4.12:** Phase separation of aqueous phase containing Cl-36 amongst other RN and iodine bearing organic phase.



**Figure 4.13:** Stripping of iodine from the organic phase back into aqueous phase.

## Materials and methods

---

To determine Cl-36 from the digestion liquors or leaching solutions, a 2 mL aliquot of the aqueous phase, previously stripped from iodine isotopes, was taken and caesium separated by means of acidification of the solution with 1 M HNO<sub>3</sub>, subsequent precipitation of caesium with 0.05 g AMP slurred in 1 mL concentrated HNO<sub>3</sub> and filtration through a 0.45 µm syringe filter as shown in figure 4.14.



**Figure 4.14:** Precipitation of caesium and filtration with a 0.45 µm syringe filter.

The resulting caesium free solutions (decontamination factors were within the range of  $10^3 - 10^4$ ) with dose rates in the order of less than 20 µSv/h were taken out of the hot cell for further handling. After transferring the solutions in new vials in order to avoid cross contamination of the samples, Cl-36 was separated from the solution by means of a further precipitation step. Therefore, a 5 mL aliquot of the solution was added to a stable chlorine carrier (1 g/L Cl<sup>-</sup> as NaCl) and 1 mL 0.5 M AgNO<sub>3</sub>. The voluminous, white precipitate containing AgCl-36 was filtrated off from the solution (2 µm pore size) and consecutively washed five times with 5 mL MilliQ<sup>®</sup> in order to remove radioisotopes which might bias the analysis by liquid scintillation counting, e.g. Sr-90 / Y-90 or Sb-125. After washing of the precipitate with MilliQ<sup>®</sup>, an additional rinsing step was performed with 5 mL of

1 M HNO<sub>3</sub> to remove yet undissolved metallic contaminants from the AgCl-36. Ultimately, the precipitate was dissolved in 5 mL of 13 % NH<sub>4</sub>OH and the resulting alkaline solution containing Cl-36 as presumably NH<sub>4</sub>Cl-36 prepared for analysis.

By this method, the residual RNs in the digestion liquors are effectively removed, since after the stripping of iodine from the aqueous solution, only chlorine shows large affinity to silver under formation of the respective silver salt. Other RNs pass through the filter material and can be either separated by further extraction chromatographic steps or directly determined by  $\gamma$ - and mass spectrometry (see following sections).

### **4.4.2 Determination of actinide, fission and activation product inventory**

In addition to the separation and determination of the volatile activation and fission products Cl-36 and I-129, other RNs were determined by means of various radiochemical methods within this study. From each digestion liquor or leachate, a 0.1 mL aliquot was taken and diluted by a factor of approximately 1:200 to determine the activity concentration of Cs-134 / 137 by gamma spectrometry (see section 4.4.3.2).

In order to analyse other radionuclides besides the caesium isotopes by gamma spectrometry (and to lower the dose rate of the solutions), it is necessary to lower the activity and to mitigate the Compton-background of Cs-137. Sample preparation for the determination of other gamma emitting radionuclides was performed by acidification of a 1 mL aliquot of the respective sample solution with 5 mL 1 M HNO<sub>3</sub> and mixing it with 0.08 g AMP slurred in 1 mL concentrated nitric acid followed by the filtration through a 0.45  $\mu$ m syringe filter. From the resulting solution, samples were prepared for the determination by gamma spectroscopy and ICP-MS as well as for further separation steps in order to determine the Sr-90 activity concentrations.

### 4.4.3 Analytical methods for spent nuclear fuel and cladding samples

Various analytical methods were used in this work to examine the recovery, concentration and activities of the studied high radioactive solutions. In order to monitor extraction yield and distribution factors, inactive tracers in form of CsCl-35 / 37 and CsI-127 with varying concentrations as well as active tracers (Cl-36 and I-129) were added to the samples before the separation.

#### 4.4.3.1 Liquid Scintillation Counting (LSC) for Cl-36, I-129 and Sr-90 / Y-90 activity concentration in solution

To investigate the activity concentrations of Cl-36, I-129 and Sr-90 / Y-90 in the digestion liquors and separated solutions, liquid scintillation counting (LSC) was used. LSC is a sensitive radiochemical analysis technique for the determination of alpha and beta emitting radionuclides in liquids. At this, the solution containing the radioactive isotope of interest is mixed with a “cocktail”, usually consisting of an organic solvent, e.g. toluene or xylene, and two scintillators. Energy emitted from the respective radionuclide to the solvent molecule results in an excitation of their state. The excited solvent molecules transfer their molecular activation energy to the scintillators, which emits a photon as the solvent molecule relaxes back to ground state. The resulting light quanta are converted and multiplied by a photomultiplier consisting of a cathode and electron dynode inside the device to detectable electronic impulses.

Measurements with LSC require an extensive sample preparation beforehand, since any other beta-emitting nuclide within the analysed solution can falsify the measurement<sup>18</sup>.

---

<sup>18</sup> Measurements are biased if the beta energies of the respective radionuclide mixtures are within the same energy region. For some radionuclide mixtures, e.g. H-3 and Cs-137 separation is negligible, hence the energies are far enough apart from each other that energy windows can be identified for individual analysis.

Another factor for LSC measurements which should be taken into account is a quenching effect of the recorded spectra by either the chemical composition of the analysed sample or a change in colour after the addition of the solution to be analysed.

For the analysis of Sr-90 ( $E_{\beta\max} = 0.546$  MeV) in the digestion liquors, a separation of the isotope from the caesium-free solution was conducted. At this, Sr-90 is isolated by means of a column separation on Sr\*Spec-resin (Eichrom Technologies Inc., Darien, USA) from its daughter nuclide Y-90 and the beta spectrum recorded. After accumulation of the secular equilibrium with the yttrium daughter nuclide, the beta spectrum is recorded again and the count rate calculated [GECKEIS *ET AL.*, 1995].

The sample preparation respectively separation method for Cl-36 is already mentioned in section 4.4.1. For LSC analysis of the separated chlorine bearing samples, it was necessary to record a quench correction curve (see figure 4.15) since the separation step for Cl-36 involved Ag, which blackens most scintillation cocktails, as well as alkaline sample solutions<sup>19</sup> in order to determine the activity concentration. Quench correction was performed by the addition of a known activity of Cl-36 to a LSC cocktail and a quenching agent (nitro methane) in varying amounts from 0 to 200  $\mu$ L. The resulting spectral quench parameter of the external standard (SQP(E)) is then plotted against the efficiency of the Cl-36 measurements.

---

<sup>19</sup> Most LSC cocktails are preferably used for acidic or neutral solutions in order to minimise quenching or oversaturation effects.

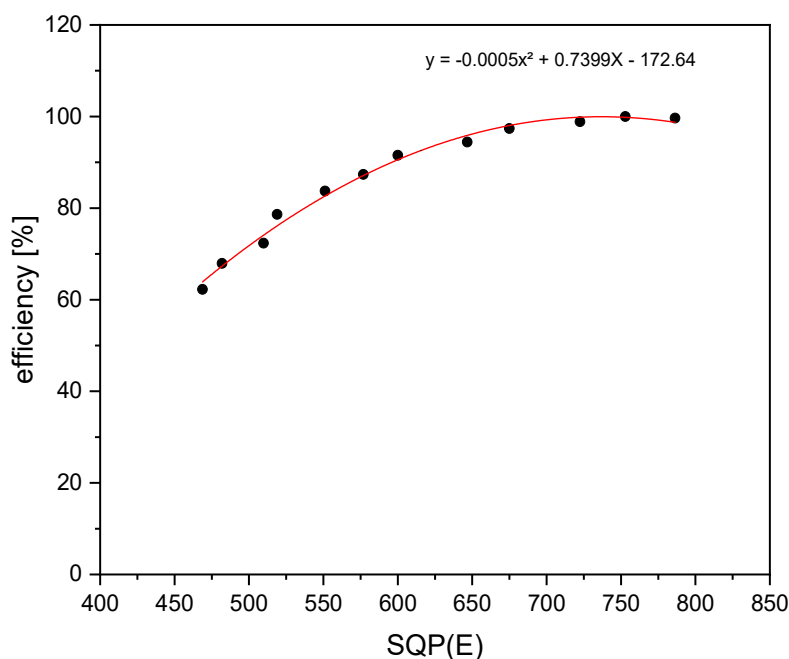


**Figure 4.15:** Quench correction curve for CI-36 in the sample geometry and ProSafe HC+ LSC cocktail with varying amounts of quenching agent. The quench parameter of the external standard (SQP(E)) is plotted against the efficiency of the measurement.

Within this work, LSC measurements were conducted for all solutions and eluates in order to examine the activity of the desired radioisotopes, as well as to derive information on the decontamination factors of the separations. Aliquots of the obtained eluates and digestion liquors were measured with an ultra-low level LSC spectrometer (Quantulus 1220, Wallac Oy, PerkinElmer) by addition of 10 mL of cocktail (ProSafe HC+, Meridian Biotechnologies Ltd., Tadworth, UK or Ultima Gold LLT/XR, PerkinElmer, Waltham, USA) in a Polyvial<sup>®</sup> (HDPE, Zinsser Analytic, Eschborn, Germany). The background of the LSC spectrometer was determined by the addition of one millilitre of the respective matrix solution into a vial without radioactive materials and was measured to be in the range of two to three counts per minute (cpm). Uncertainties for LSC measurements are within the range of < 5 %.

#### 4.4.3.2 $\gamma$ -spectrometric analysis for I-129, Co-60, Sb-125, Eu-154 / 155, Am-241 and Cs-134 / 137 activity concentration in solution

In addition to LSC measurements,  $\gamma$ -spectrometry was conducted in order to analyse the I-129 ( $E_\gamma = 39.58$  keV), Cs-134 ( $E_\gamma = 604.72$  keV), Cs-137 ( $E_\gamma = 661.66$  keV), Eu-154 ( $E_\gamma = 123.07$  and  $1247.4$  keV), Eu-155 ( $E_\gamma = 86.55$  and  $105.31$  keV) as well as Am-241 ( $E_\gamma = 59.54$  keV) activities in solution and, especially regarding the Zircaloy specimens, the activities of Co-60 ( $E_\gamma = 1173.2$  and  $1332.5$  keV) as well as Sb-125 ( $E_\gamma = 427.88$  and  $600.6$  keV)<sup>20</sup>. Determination of  $\gamma$ -ray emitting RNs is performed by the measurement of charge carriers within semiconducting materials, e.g. high purity germanium, as ionising radiation generates electron-hole pairs. The electric pulse generated as the electrons and holes move to the respective electrodes within the detector system is further amplified and analysed by a multichannel analyser.

Activity measurements were performed with a high-resolution  $\gamma$ -spectrometer (GX3018, Canberra Industries Inc., USA) equipped with an extended range coaxial Ge detector and a relative efficiency of  $\geq 30$  %. Energy calibration of the device was performed with a certified multi-nuclide standard (Mixed Gamma 7600, Eckert & Ziegler Nuclitec GmbH, USA) and data was evaluated using the Genie 2000 software (Canberra Industries Inc., USA).

Aliquots of one millilitre each were examined in two millilitre APEX<sup>®</sup> screw cap vials (PP, Alpha Laboratories Ltd., Eastleigh, UK) with an approximate measuring time of 180 minutes. For Cs-134 / 137 determination the samples were further diluted by a factor of 1:10 (see section 4.4.2). Uncertainties for  $\gamma$ -spectroscopic measurements are in the range of  $< 5$  %.

---

<sup>20</sup> Gamma energies listed display decays with most intensity for the respective isotope.

### **4.4.3.3 Inductively coupled plasma mass spectrometry (ICP-MS) for I-127 and actinide concentration analysis in solution**

For U-233 / 234 / 235 / 236 / 238, Np-237, Pu-239 / 240 / 241 / 242, Am-241 / 243, Cm-244 / 245 / 246 inventory, as well as for recovery tests for added inactive I-127 to the solutions, inductively coupled plasma mass spectrometry (ICP-MS) measurements were performed. At this, a nebulised sample aerosol is introduced in a spray chamber and directed into an Ar plasma, where molecules dissociate and atoms are ionised. The produced ionic species are separated by means of a mass analyser. This mass analyser consists in most cases of four parallel coordinated molybdenum rods in form of a quadrupole with an electrical current applied to it. The resulting electromagnetic field is only traversable for ions with an equivalent mass-to-charge ratio to the field resonance. Subsequently, the segregated ionic species are multiplied in an electron multiplier, resulting in an electron cascade, which can be detected as impulse.

In order to reduce the background electrolyte concentration of the aliquots and to obtain the ideal concentration in the range of 1 – 10 ppb for the nuclides to be analysed, samples were diluted with either 2 % HNO<sub>3</sub> or MilliQ<sup>®</sup> water (in order to prevent loss of iodine) by varying factors and afterwards measured by ICP-MS (NexION 2000, PerkinElmer, USA). The uncertainties of the device are in general within a range of 10 %, but depend on the respective nuclide and concentration level.

### **4.4.3.4 Ion chromatography (IC) for total chlorine concentration**

The determination of total chlorine concentration was carried out by ion exchange chromatography (IC), which is based on the exchange of solvated ions in a mobile phase and surface adsorbed ions in a stationary phase. The ions are hereby separated due to their varying affinity to the positively charged ion exchange resin. For sample analysis, the conductivity of the aliquot is depicted as a function of time resulting in a chromatogram.

Sample preparation was performed by dilution of the digestion liquors, leachates and solutions with MilliQ<sup>®</sup> water in order to acquire the optimum concentration of 1 – 10 ppm chlorine in the aliquots. IC measurements (ICS-1100 Dionex, Thermo Scientific, USA) were thereafter conducted to obtain the total chlorine concentration. A distinction between the different chlorine isotopic species is not possible. The lowest detection limit of the device is 0.01 ppm with an overall uncertainty of 5 – 10 %.

#### **4.4.3.5 Gas mass spectrometry (gas-MS) for the determination of fission gas inventory and release during digestion process**

Gas samples obtained from the alkaline digestion processes of the SNF specimens in the respective autoclaves were analysed by gas mass spectrometry (GAM400, InProcess Instruments, Germany) for the fission gas inventory and possible iodine evaporated during the dissolution process. The gas-MS is equipped with a secondary electron multiplier for precise low concentration measurements. The gas sampling cylinder is connected to the gas-MS inlet system and the gas phase successively measured for ten times, giving a mean value of the measurements. Analytic uncertainties are in the range of 5 %.

## 4.5 Calculation of the radionuclide inventory in irradiated Zircaloy-4 and fuel

RN inventory including the estimation of Cl-36 content via its precursor Cl-35<sup>21</sup> for Zry-4, UO<sub>x</sub> and MOX fuel was calculated by using the Monte Carlo N-particle code in conjunction with the neutron activation and burn-up module CINDER (MCNP6 / CINDER) as well as the webKORIGEN package [WILSON *ET AL.*, 2008; NUCLEONICA GMBH, 2011; PELOWITZ *ET AL.*, 2013]<sup>22</sup>. The nuclear data (neutron cross sections, fission product yields, etc.) is based on the ENDF-B-VII data library [CHADWICK *ET AL.*, 2011]. The simulated subassemblies are taken from the KKG and KWO reactors (see sections 4.2.1 and 4.2.2) and in accordance with their operation conditions. The reaction rate calculations within MCNP6 / CINDER are based upon 3D geometrical shape of the assembly, as well as on the given burn-up, level, irradiation time and the linear power rate. In case of chlorine activation calculations, the impurity concentration within the fuel and cladding has to be carefully regarded, as chlorine is not produced by nuclear fission (see section 3.1). By the MCNP calculations, an average neutron flux of  $3.8 \times 10^{14}$  n/cm<sup>2</sup>s was obtained and burn-ups of 38.0 and 50.4 GWd/t<sub>HM</sub> were adjusted for the respective fuel types.

In both cases, the fuel and Zircaloy cladding, the exact impurity or alloying constituent of chlorine exhibits a large uncertainty (see sections 2.2 and 3.1) leading to pronounced discrepancies with the measured data. Therefore, minimum and maximum impurity

---

<sup>21</sup> For activation calculations the isotopic composition of pristine chlorine which amounts to 75.77 % chlorine-35 and 24.23 % chlorine-37 has to be taken into account.

<sup>22</sup> Calculations within this subsection were performed by apl. Prof. Dr. Ron Dagan of KIT-INE.

values for fuel (1 – 25 ppm) and Zircaloy (1 – 20 ppm)<sup>23</sup> were chosen as a most optimistic assumption made (see section 3.1) for the calculations.

## 4.6 Microscopic examinations of the fuel-cladding interface

Microscopic and spectroscopic examinations were performed for fragments and cladding segments with fuel residue of a high burn-up UO<sub>x</sub> and MOX fuel, respectively. Microscopic visualisation of the SNF specimens was conducted with a digital microscope (DigiMicro 2.0, Drahtlose Netztechnik, Germany) located inside the hot cells at KIT-INE (see section 4.2.1 – 4.2.3). Spectroscopic examinations involving synchrotron radiation were performed in terms of X-ray absorption (XAS) measurements at the INE and CAT-ACT beamlines located at the Karlsruhe Research Accelerator (KARA) synchrotron facility. In addition, energy and wavelength dispersive scanning electron microscopic (SEM-EDS / WDS) and X-ray photoelectron spectroscopic (XPS) measurements were conducted in order to obtain further insights into the surface composition of the respective specimen.

---

<sup>23</sup> Chosen minimum and maximum Cl-35 values are five times smaller or five times larger than the Cl-35 estimated, as given by Guenther and colleagues and Tait and Theaker, respectively [GUENTHER *ET AL.*, 1988; TAIT AND THEAKER, 1996]

### 4.6.1 Sample preparation for spectroscopic analysis of fuel, cladding and fuel-cladding interaction layer

For spectroscopic measurements, in total four fuel and cladding samples from each type of nuclear material were prepared. In accordance with the technical advisory board of KIT-INE and German radiation protection laws, the specimens with contact dose rates of  $\approx 6$  mSv/h for the fuel fragments and  $\approx 0.3$  mSv/h for the cladding samples were removed from the hot cell and transferred to a ventilated isotope fume hood for further preparation. For XAS measurements, a fuel fragment and cladding segment of each fuel type was prepared in a specifically designed sample holder as depicted in figure 4.16. The sample holder was fabricated of a  $25 \times 25$  mm rectangular block of aluminium with approximately 10 mm in thickness. For sample adjustment, a circular immersion was milled in central position with a diameter of 5 mm and a depth of 3 mm, in which the sample was placed without adhesive in order to ensure as little chlorine contamination<sup>24</sup> as possible. Following emplacement of the specimen, the immersion was sealed twice with 8  $\mu$ m polyimide foil (KAPTON<sup>®</sup>, DuPont, USA) and the foil fixated to the aluminium sample holder with chlorine-free ( $\leq 0.09$  % chlorine), adhesive polyimide tape (KAPTON<sup>®</sup>, DuPont, USA) in order to ensure a double-containment for the radioactive specimen and prevent contamination. For transfer to the synchrotron facility, the samples were measured by means of wipe tests in order to confirm that all surfaces are contamination free and subsequently emplaced in certified lead shielding vessels for transport.

---

<sup>24</sup> Previous sample preparation for synchrotron radiation based techniques involved double sided adhesive carbon tabs, which were identified as a contamination source for chlorine measurements biasing surface analysis.



**Figure 4.16:** Sample holder designated for XAS measurements of SNF specimens.

Further spectroscopic surface and bulk analysis of the specimens was carried out by means of XPS and SEM-EDS measurements. For this purpose, the respective sample was immersed in MilliQ<sup>®</sup> water and treated in an ultrasonic bath for 15 minutes followed by a rinsing step with isopropanol in order to prevent further fragmentation and thus contamination of the spectrometers. After drying of the specimens in air, fuel fragments and cladding segments were emplaced separately on a double-sided adhesive carbon tab adjusted on an aluminium sample holder.

#### **4.6.2 Scanning electron microscopy – energy / wavelength dispersive X-ray spectroscopy (SEM-EDS / -WDS)**

Scanning electron microscopy (SEM) measurements in conjunction with energy and wavelength dispersive X-ray spectroscopy (EDS / WDS) were performed to gain information on the chemical composition of the Zircaloy segments of both the UO<sub>x</sub> and

MOX fuel. For measurements the SNF samples were removed from the hot cell, immersed in MilliQ<sup>®</sup> water and treated in an ultrasonic bath for 30 minutes. The respective specimen had then been rinsed with isopropanol, dried and mounted on a double-sided adhesive carbon tab on an aluminium sample holder and sealed with a polyethylene cap. SEM-EDS / -WDS measurements were performed by use of a Quanta 650 FEG (Thermo Fisher Scientific, accelerating voltage 15 kV, beam current 1 nA, 1  $\mu$ m information depth) in order to obtain data on the surface composition, especially on the concentrations of iodine, chlorine and caesium. Data analysis was performed using Pathfinder software for the Quanta 650 FEG instrument.

### **4.6.3 X-ray photoelectron spectroscopy (XPS)**

In order to derive further information on the surface composition of the fuel and cladding specimens, XPS measurements were conducted. XPS analysis offers a very sensitive method for characterisation of the surface chemistry of solid phases without extensive sample preparation. Measurements were performed on a ULVAC-PHI VersaProbe II spectrometer mounted with an Mg K $\alpha$  ( $E = 1253.6$  eV) and an Al K $\alpha$  ( $E = 1486.7$  eV) radiation source as well as a monochromatic microprobe source prior to analysis of the specimens by SEM-EDS (see section 4.6.2). XPS measurements were performed in an ultra-high vacuum chamber within the device and data treatment was performed by use of the PHI MultiPak program. For metals the binding energy errors are in the range of  $\pm 0.1$  eV.

### **4.6.4 X-ray absorption spectroscopy (XAS)**

Within this work, X-ray absorption (XAS) was performed on spent fuel fragments as well as Zircaloy cladding with fuel residue attached to it. XAS is a spectroscopic method which

provides information on the redox state, chemical periphery and coordination environment of the respective sample. At this, core electrons of the element to examine are excited, resulting in an elevated absorption of X-ray radiation at the respective absorption edge. The intensity of the emitted beam ( $I_0$ ) by the synchrotron source was measured and monitored by use of an Ar-filled ionisation chamber. Cl K-edge ( $E = 2822$  keV) and I K-edge ( $E = 33169$  keV) X-ray absorption near edge structure (XANES) measurements were conducted at the INE and CAT-ACT beamline of the Karlsruhe Research Accelerator (KARA)<sup>25</sup> synchrotron facility [IBPT, 2016; ROTHE *ET AL.*, 2019].

Data treatment for XANES measurements was performed with the respective beamline scientists using the Demeter IFEFITT program pack [RAVEL AND NEWVILLE, 2005] and with PyMCA software package [SOLÉ *ET AL.*, 2007].

#### 4.6.4.1 Cl K-edge measurements

Low energy Cl K-edge measurements were performed at the INE-beamline by use of a double crystal monochromator equipped with Si[111] crystals (Vortex 60EX, Hitachi, USA). Prior to the measurement of the high active specimens, energy calibrated spectra were recorded in transmission mode by use of a crystalline CsCl reference (2824.9 keV) in the same sample holder geometry. In order to verify that no chlorine contamination is present neither in the sample holder nor the polyimide containment of the samples<sup>26</sup>, beforehand an empty sample vessel was measured. In total, two samples, a fuel fragment and a cladding segment, from each fuel type (UO<sub>x</sub> and MOX) were analysed for their chlorine content and chemical form. Additionally, a high-purity, reactor grade Zry-4 cladding tube segment (Framatome, Erlangen, Germany) was analysed in order to compare it to the irradiated material.

---

<sup>25</sup> Until 2015 referred to as Ångströmquelle Karlsruhe (ANKA).

<sup>26</sup> Chlorine contamination could also result from the acrylic glass containment, where the sample holder systems were placed in or by backscattering material within the hutch. These sources of contamination could not be identified as no Cl K-edge jump was detected in blank measurements.

### 4.6.4.2 I K-edge measurements

Measurements for I K-edge were conducted at the CAT-ACT-beamline by energy calibration of a crystalline CsI standard reference material (33182 keV) using a pair of Ge[422] crystals mounted on a double crystal monochromator in a 45° angle to the five pixel LGe solid state detector (Canberra, Belgium). Subsequently, the specimens, cladding and fuel of the respective fuel types were analysed for their iodine speciation as well as measured semi-quantitatively for the amount of iodine within the samples.

## 4.7 Simulation of Zircaloy-SNF interactions

In order to derive information on the behaviour of the cladding tube integrity during prolonged interim storage under dry conditions, experiments were conducted with non-irradiated, reactor-grade Zircaloy-4 in presence of caesium, iodine and chlorine bearing compounds as well as depleted UO<sub>2</sub> pellets. The prepared samples were stored in an inert gas environment (autoclave) and under elevated temperature to simulate conditions as they are expected during interim storage (see sections 2.4 and 2.5). Insights gained by this experiment are anticipated to ensure better information on degradation effects of the cladding in case of an extended interim storage period by caesium-, chlorine- and iodine-rich compounds as they are envisaged as integrity mitigating agents.

### 4.7.1 Experimental set-up for the cladding corrosion experiment with non-irradiated Zircaloy-4

Four Zircaloy-4 platelets ( $10 \times 10 \times 0.65$  mm, Framatome, Erlangen) were washed with MilliQ<sup>®</sup> water and isopropanol, treated in an ultrasonic bath for 30 minutes and polished in order to obtain a clean and smooth surface and to remove impurities from the surface which could bias the results. In addition, two UO<sub>2</sub> pellets containing depleted uranium (10.75 mm in diameter, 5 mm in height,  $m = 3.4$  g,  $A = 42.5$  kBq) were treated in an ultrasonic bath in similar manner as stated above. Subsequent to the purification (and polishing) of the specimens, the prepared Zircaloy and UO<sub>2</sub> samples were introduced into an inert gas glove box filled with Ar. Figure 4.17 shows exemplarily the polished surface of the Zircaloy platelets.

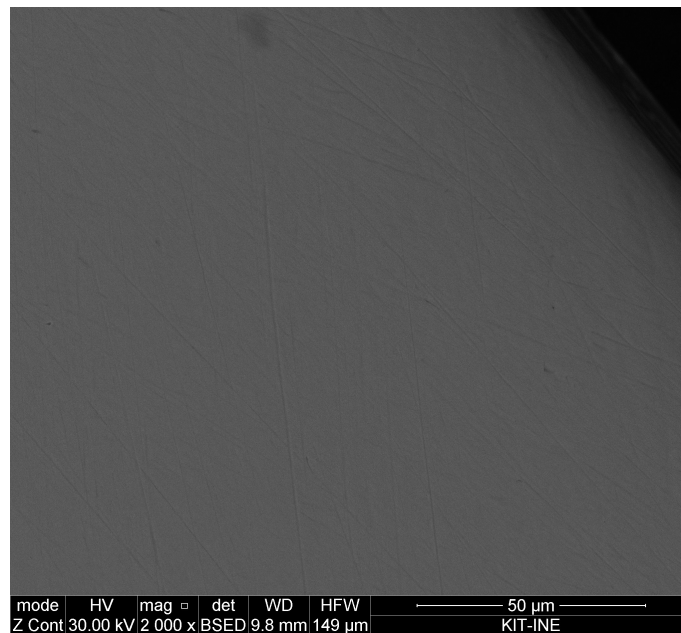


**Figure 4.17:** Polished Zircaloy-4 surface of the platelets utilised in the cladding corrosion experiment.

## Materials and methods

---

In order to prevent air contamination during the heating and subsequent cooling of the experiment, two sample vessels for the Zircaloy platelets and  $\text{UO}_2$  pellets were designed. The sample vessel consisted of a cubic aluminium block ( $25 \times 25 \times 25$  mm) with eight screw threads and a central cavity (15 mm in diameter, 10 mm in depth) in which the respective specimen was inserted. An aluminium plate ( $25 \times 25 \times 10$  mm) also provided with eight screw threads was fashioned as a lid for the vessel. To ensure tightness of the sample vessel, a metallic copper gasket ( $25 \times 25 \times 1$  mm) with circular guides for the screws was fabricated by previously smouldering the copper plate. Figure 4.18 depicts the sample vessel, copper gasket and the specimens.

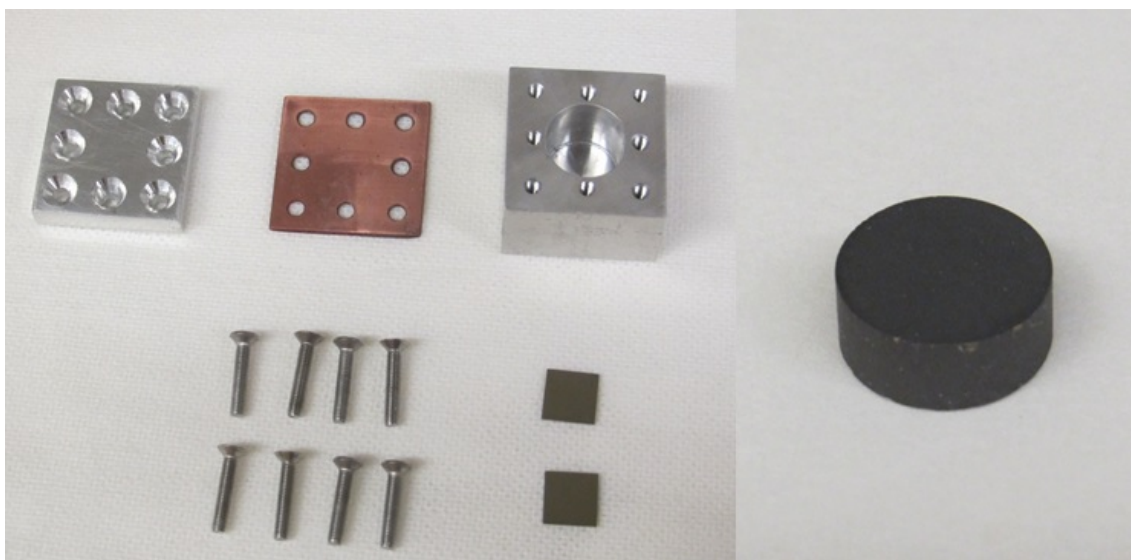


**Figure 4.18:** Design and dimensions of the components for the cladding corrosion experiment. Left side shows the individual parts of the sample vessel, as well as the Zircaloy platelets. Right picture depicts the depleted  $\text{UO}_2$  pellet.

In addition to the aluminium sample vessels and for further prevention of air intrusion as well as radioactive contamination, a stainless-steel autoclave ( $\approx 75$  mL, Carl Roth, Germany) equipped with a tantalum liner and graphite sealing rings<sup>27</sup> was utilised. The

---

<sup>27</sup> Graphite sealing rings were chosen as temperature stable gaskets for the heating experiment.

autoclave, tantalum liner and sealing rings are shown in figure 4.19. Sample vessels and the autoclave parts were introduced into the inert gas glove box as well.



**Figure 4.19:** Autoclave, tantalum liner and graphite sealing rings for the cladding corrosion experiment.

Zircaloy platelets were inserted into the aluminium sample vessels, the respective inactive caesium halide salt deposited on the polished surface and brought into contact with the depleted  $\text{UO}_2$  pellets alongside the cylindrical surface. Each vessel was loaded with two Zircaloy platelets and one depleted  $\text{UO}_2$  pellet, being stacked “sandwich-wise” in order to ensure contact of one platelet surface with the surface of the  $\text{UO}_2$  (see figure 4.20). Table 4.5 lists the deposited fission and activation product salt analogues.

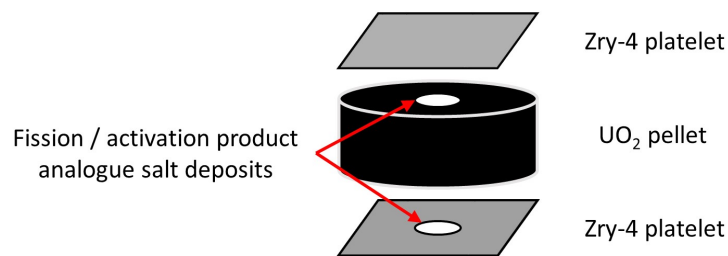


**Figure 4.20:** Experimental setup for the cladding corrosion experiment.

## Materials and methods

---

**Table 4.5:** Deposited fission and activation product salt mixtures simulating components at the Zircaloy-UO<sub>2</sub> interface.

No. of Zircaloy-4 platelet	Deposition of salt
1	1 mg CsCl
2	1 mg CsI
3	1 mg CsCl / 1 mg CsI
4	no deposition / blank sample

After insertion in the aluminium sample vessel and securing that the components are in direct contact with each other over their respective surfaces, the vessels were mounted with the copper gasket and aluminium lid and ultimately bolted tightly with eight screws under Ar-atmosphere and ambient pressure. Both bolted sample vessels were transferred to the tantalum liner and eventually the autoclave equipped with the graphite sealing rings was sealed air tight with a torque of 25 Nm and removed from the inert gas glove box.

The charged autoclave was then put into a high temperature oven (Heraeus, Germany) and heated to approximately 400 °C. Figure 4.21 shows the interior of the used high temperature oven.



**Figure 4.21:** Interior of the high temperature oven used for the cladding corrosion experiment.

Over the course of three months, the temperature in the oven was reduced by 30 °C each seven days in order to simulate<sup>28</sup> the decay heat decrease of the fuel assembly in a transport and storage vessel within an interim storage facility. Table 4.6 lists the envisaged temperature decrease and time intervals.

**Table 4.6:** Time intervals and temperature during the cladding corrosion experiment.

---

<b>Time interval, cumulative [d]</b>	<b>Temperature [°C]</b>
<b>0</b>	400
<b>7</b>	370
<b>14</b>	340
<b>21</b>	310
<b>28</b>	280
<b>35</b>	250
<b>42</b>	220
<b>49</b>	190
<b>56</b>	160
<b>63</b>	130
<b>70</b>	100
<b>77</b>	70
<b>84</b>	40
<b>91</b>	r.t.

---

<sup>28</sup> In reality, the decay heat decrease of SNF assemblies stored in a transport and storage vessel is much slower than performed within this experiment.

After 91 days the experiment was terminated and the autoclave respectively sample vessels opened in a ventilated isotope fume hood. The Zircaloy and UO<sub>2</sub> specimens were retrieved from the vessels, submerged in isopropanol and treated in an ultrasonic bath for 20 minutes. Subsequently, the samples were dried and prepared for analysis (see section 4.7.2).

### **4.7.2 Examination of non-irradiated Zircaloy-4 specimens**

After retrieving the samples from the reaction vessels and subsequent cleaning, the Zircaloy surface was examined by means of optical microscopy, XPS and SEM-EDS in order to evaluate potential cladding degradation phenomena occurring on the surface. XPS and SEM-EDS sample preparation was performed as described in section 4.6.2 on the same type of sample holder. Measurements were conducted in order to analyse possible reactions at the Zircaloy surface. Pictures of the respective Zircaloy specimen were taken at 30 kV; measurements were performed with electron acceleration voltages ranging from 15 to 20 kV.

## **5 Results and Discussion**

### **5.1 Determination of radionuclide inventory in SNF, cladding and fuel-cladding interaction layers**

In the frame of this Ph.D. thesis, radionuclide inventories of defined regions in used fuel pellets with respect to two different types of SNF were determined. Special focus was set on the volatile activation and fission products Cl-36 and I-129. Both radionuclides are difficult to measure due to their emitted radiation (Cl-36 is a pure  $\beta^-$  emitter and has no  $\gamma$ -lines, I-129 emits  $\beta^-$  and low energy  $\gamma$ -radiation, 39.58 keV), hence a precise and profound separation and analytical method for them is indispensable. In the following sections, selected RN inventory data are listed, compared and discussed. For the overall inventory of all measured RN in the different specimens, the reader is referred to the appendix section.

### 5.1.1 Recoveries of the separation method for Cl-36 and I-129

Recoveries of the separation technique were monitored by the addition of a defined amount of carrier solution containing the inactive isotopes Cl-35 / 37 and I-127 to solutions after digestion of SNF and Zircaloy specimens, respectively. Furthermore, for quality control, tracer experiments were conducted by performing a separation of blank sample solutions, where known activities of Cl-36 and I-129 were added beforehand. Analysis of the respective halogen containing solutions after application of the separation technique with IC, ICP-MS and LSC showed an overall recovery yield of  $(94 \pm 2)$  % for chlorine and  $(93 \pm 3)$  % for iodine for the respective Zircaloy or SNF matrices. Results of selected recovery tests including a SNF or Zircaloy matrix are shown in table 5.1 with respect to the concentration of used carrier isotopes in addition to e.g. HCl, NaCl or CsI. For Zircaloy specimens, no iodine carrier was added since it is assumed, that due to the digestion method involving concentrated acids, I<sub>2</sub> would evaporate. It should be further noted, that in case of recovery tests performed with solutions without the irradiated material as matrix compound, recovery yields were between 98 and 100 %. LSC spectra for recovery tests performed without the influence of a SNF or Zircaloy matrix are shown in figure 5.1 displaying a clean separation of both RN from each other.

Yet for validation, the respective matrix influence as well as handling within the hot cell has to be taken into account. Similar extraction yields were also observed by Tait and colleagues for the precipitation of Cl-36 as silver halide salt (recovery yield 100 %) and by Geckeis and co-workers for the liquid-liquid extraction of I-129<sup>29</sup> [GECKEIS *ET AL.*, 1995; TAIT *ET AL.*, 1997].

---

<sup>29</sup> Geckeis and co-workers reported recovery yields of up to 70 % for the iodine separation, yet a loss of iodine has to be taken into account since the separation of caesium was performed beforehand in concentrated nitric acid.

**Table 5.1:** Selected recovery tests performed as double determinations in order to monitor the extraction yield of the separation technique. Recovery test No. 1 + 2 involved an irradiated Zircaloy matrix, whilst 2, 3 and 5 were performed with alkaline digested SNF.

recovery test No.	Added tracer [ppm]		recovery of tracer [ppm]		recovery of tracer [%]	
	Cl-35 / 37 (± 5 %)	I-127 (± 5 %)	Cl-35 / 37 (± 5 %)	I-127 (± 5 %)	Cl-35 / 37 (± 5 %)	I-127 (± 5 %)
1	4.0	-	3.9	-	97.5	-
2	1.2	-	1.0	-	83.3	-
3	12.5	15.0	11.9	13.2	95.2	87.8
4	5.0	15.0	4.7	13.4	94.0	89.4
5	25.0	30.0	25.2	32.0	101	107
mean value ± SD					94 ± 2	93 ± 3

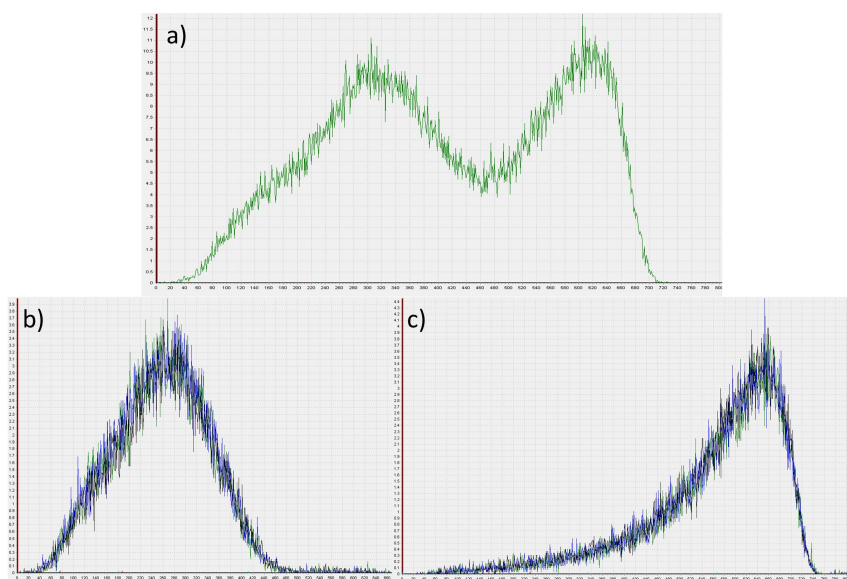


**Figure 5.1:** LSC spectra of recovery tests without a SNF or Zircaloy matrix showing a clean separation of I-129 (b) and Cl-36 (c) from the initial sample solution (a)). Spectra displayed as frequency of impulses as a function of channel number.

Furthermore, two possible phenomena were examined which could result in the loss of either Cl-36 or I-129 throughout the separation procedure, i.e. the loss of chlorine due to photochemical degradation of the silver halide salt and volatilisation of iodine during the alkaline digestion process of the SNF specimens.

For Cl-36 no loss was observed in recovery experiments throughout the whole separation process even after halting the separation procedure for one day in between the MilliQ<sup>®</sup> washing steps with exposure of the silver halide salt to light. In addition, as described in section 4.3, an autoclave digestion of an UO<sub>x</sub> fuel fragment was performed with addition of inactive I-127 carrier and subsequent analysis of the gas phase in order to monitor a loss of I-127 / 129 by analysing the obtained gas composition in a mass spectrometer. No signal for mass 127 (isobaric Xe-127 is radioactive with a short half live of 36.4 d and thus not present in the fuel anymore) was observed within the gas phase and thus it is concluded that no iodine is volatilised during the digestion process of the SNF.

### **5.1.2 Determination of Cl-36 and I-129 inventory in digestion liquors of high active specimens**

Figure 5.2 depicts the results of the experimental inventory analysis for Cl-36 in the studied SNF specimens. The determined activities (see table 5.2.) are in good agreement with respect to their analytical uncertainty as expected by the scarce literature data for used fuel by e.g. Tait and colleagues who postulated a value for spent CanDU fuel of approximately  $4.22 \times 10^8$  Bq/t<sub>HM</sub> from ORIGEN-S code calculations [TAIT *ET AL.*, 1997].

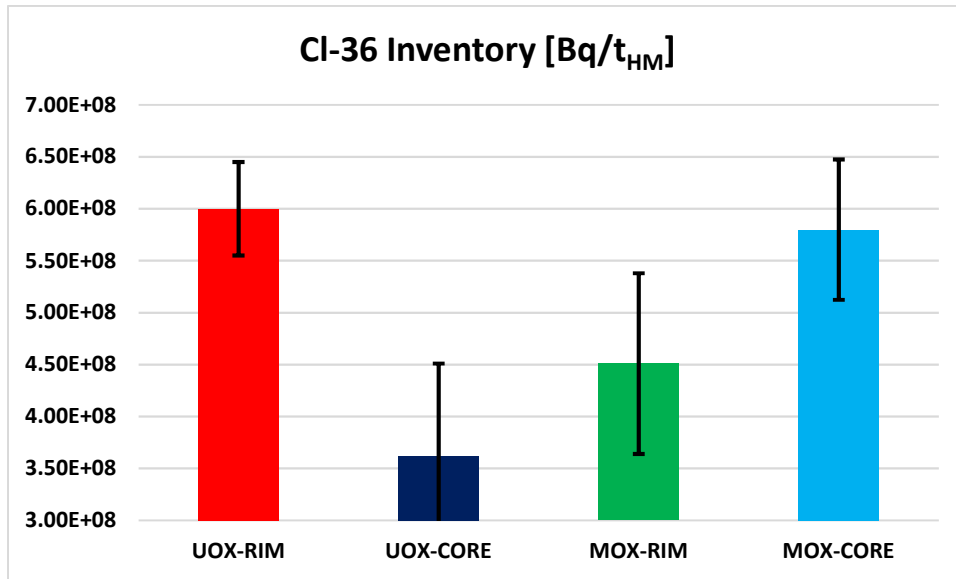


**Figure 5.2:** Cl-36 inventory [Bq/t<sub>HM</sub>] of the digested fuel specimens with respect to the sampling region in the SNF pellet.

**Table 5.2:** Experimental Cl-36 inventories [Bq/t<sub>HM</sub>] of the examined fuel types with respect to the sampling region in the SNF pellet.

Sample	UO <sub>x</sub> -RIM	UO <sub>x</sub> -CORE	MOX-RIM	MOX-CORE
Cl-36 activity [Bq/t <sub>HM</sub> ]	6.0(±0.9) × 10 <sup>8</sup>	3.6(±0.5) × 10 <sup>8</sup>	4.5(±0.7) × 10 <sup>8</sup>	5.8(±0.9) × 10 <sup>8</sup>

In case of the UO<sub>x</sub> fuel, an enrichment of Cl-36 in the cladding adjacent rim area can be seen in conjunction with a significantly lower Cl-36 inventory in the central area, whereas for the MOX fuel the Cl-36 inventories in the rim and core area are the same within the error. Several conceivable reasons for the relative strong Cl-36 enrichment in the rim zone of the UO<sub>x</sub> fuel in contrast to the Cl-36 distribution in the MOX fuel might be feasible. One explanation could be, that due to the higher burn-up of 50.4 GWd/t<sub>HM</sub> as well as the higher linear power rate of 260 W/cm of the UO<sub>x</sub> fuel and thus a pronounced gap closure a considerable portion of chlorine is transported to the rim area compared to the 38.0 GWd/t<sub>HM</sub> and 200 W/cm average linear power rate of the MOX fuel. This would

## Results and Discussion

imply that Cl-36 behaves in a similar manner to iodine within the fuel, following the thermal gradient and grain boundaries resulting in the enrichment at the pellet-cladding interface during reactor operation and beyond. Based on digestion and leaching experiments, Tait and co-workers stated, most of the chlorine may still be bound to the fuel matrix and would be released consecutive to a slow dissolution of the (U, Pu)O<sub>x</sub> matrix [TAIT *ET AL.*, 1997].

Furthermore, the Cl-36 inventory in the Zircaloy cladding specimens in contact with the respective UO<sub>x</sub> and MOX fuels were determined experimentally. Figure 5.3 shows the recorded LSC spectrum of a Cl-36 standardised solution to which the separation technique was applied in comparison to the Cl-36 LSC spectrum of the Zry-UO<sub>x</sub> specimen. The high energy part in displayed in the right spectrum depicts the background of the LSC measurement.

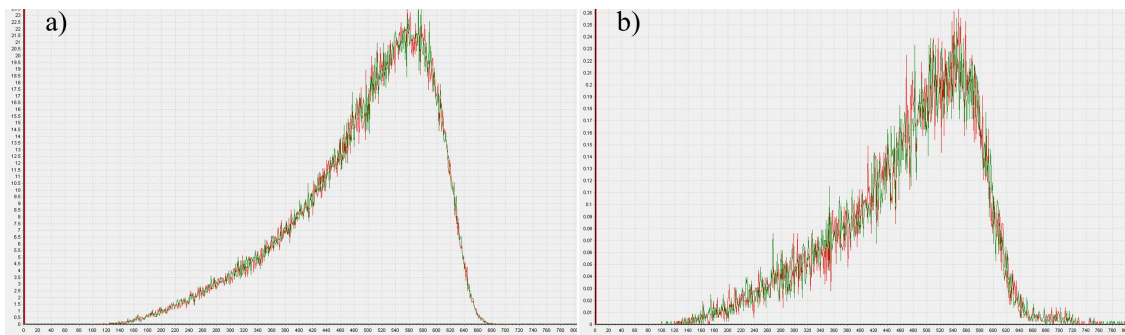


**Figure 5.3:** Recorded Cl-36 spectra of a) a Cl-36 standard solution and b) extracted Cl-36 from the Zry-UO<sub>x</sub> specimen. Spectra displayed as frequency of impulses as a function of channel number.

Results of the Cl-36 inventory in the Zircaloy samples of the UO<sub>x</sub> and of the MOX fuel rod segments are shown in figure 5.4 respectively table 5.3 and compared to the values calculated by MCNP assuming the same initial Cl-35 content in the Zircaloy for both fuel types (see section 4.5). The experimentally determined activity values are in accordance with the Cl-36 inventories obtained by MCNP activation calculations within the analytical uncertainty (see figure 5.4). Slightly higher values are found experimentally

for Zry-UO<sub>x</sub> and for the calculated Cl-36 inventory. Since the same initial Cl-35 content is used in the calculations, for both the Zircaloy of the UO<sub>x</sub> and the Zircaloy of the MOX fuel rod segment, differences in calculated Cl-36 inventories are caused by reactor operation parameters of the two irradiated fuel rod segments. Cl-36 activities in Zry-MOX specimens are found to be lower, presumably due to the lower burn-up resulting in the lower activation of the Cl-35 precursor in the MOX sample. Notably, the measured Cl-36 activities of the Zry-UO<sub>x</sub> and Zry-MOX samples are equal to the respective calculated values, within error, and thereby they reflect the differences in activation of chlorine in the cladding of the studied UO<sub>x</sub> and MOX fuel rod segments. Similar results for Cl-36 in Zircaloy cladding are obtained by activation calculations performed by Caruso [CARUSO, 2016]. The author calculated the Cl-36 inventory in a 55 GWd/t<sub>HM</sub> UO<sub>2</sub>, as well as in a 55 GWd/t<sub>HM</sub> MOX fuel pin with initial chlorine impurities of 20 ppm resulting in the generation of Cl-36 within the order of 10<sup>8</sup> Bq/t<sub>HM</sub> demonstrating the reliability of the applied digestion method of the specimen and separation technique for Cl-36.

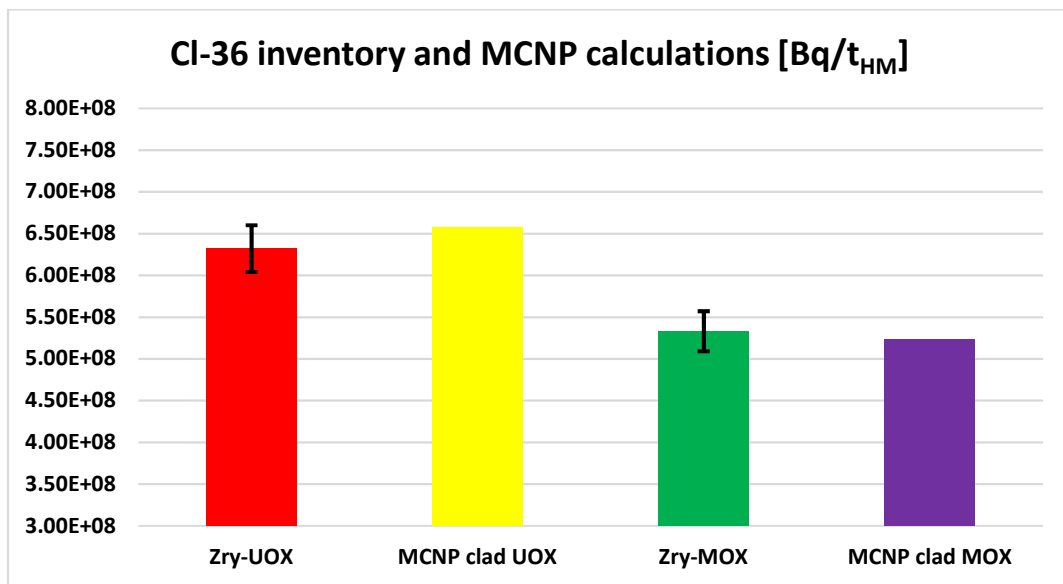


**Figure 5.4:** Experimentally derived Cl-36 inventories [Bq/t<sub>HM</sub>] of the Zircaloy specimens of the UO<sub>x</sub> and MOX fuel and values obtained by MCNP / CINDER calculations.

## Results and Discussion

---

**Table 5.3:** Experimentally obtained Cl-36 inventories [Bq/t<sub>HM</sub>] in the Zircaloy specimens compared to results derived from MCNP calculations for 15 ppm initial Cl-35 impurity.

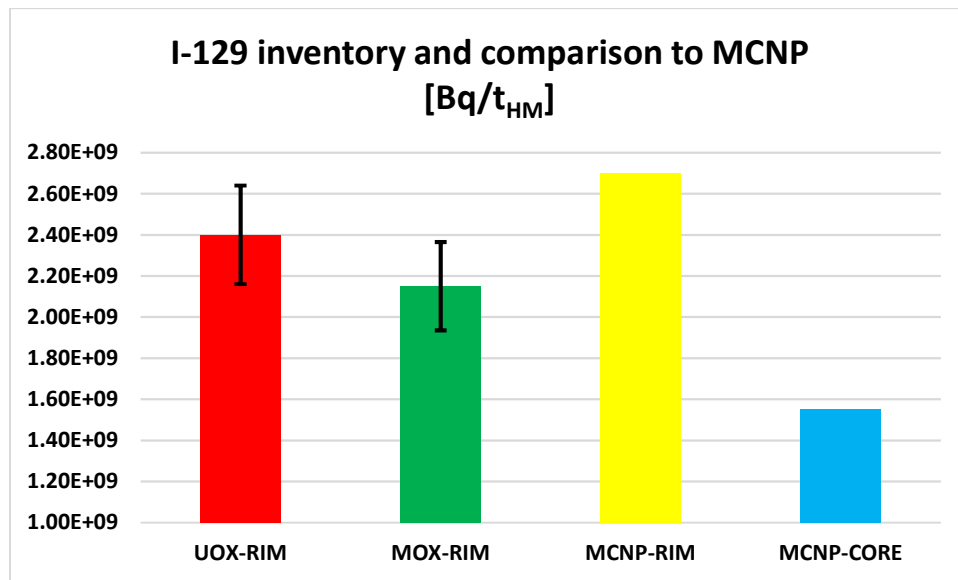
Sample	Zry-UO <sub>x</sub>	MCNP clad UO <sub>x</sub>	Zry-MOX	MCNP clad MOX
Cl-36 activity [Bq/t <sub>HM</sub> ]	6.3(±0.3)×10 <sup>8</sup>	6.6×10 <sup>8</sup>	5.3(±0.2)×10 <sup>8</sup>	5.2×10 <sup>8</sup>

Figure 5.5 and table 5.4 show the results of the experimentally obtained I-129 inventory in the UO<sub>x</sub> and MOX rim specimens in comparison to values obtained by MCNP calculations for the rim and central area of the fuel pellet. Notably, about the same I-129 activities are calculated for the UO<sub>x</sub> and the MOX central samples. Similarly, calculated I-129 activities are about the same for the UO<sub>x</sub> and the MOX rim samples. Therefore, only two columns are shown in figure 5.5 for the calculated I-129 inventories. However, MCNP calculations suggest a considerable enrichment in the rim as compared to the central part of the fuel pellet. The MCNP values calculated for the rim area of the pellet are to some extent comparable to the experimental values. Yet a loss of highly volatile iodine in both specimens (UO<sub>x</sub> and MOX) cannot be excluded due to cutting of the samples and mechanical defueling (see section 4.2.4) as well as part of the digested specimens consisted of not only the rim area owing to the sample size of approximately 1 mm<sup>2</sup>. On the other hand MCNP calculations will also be associated with uncertainties with regard to input parameters and cross section data.

In general, MOX fuel, more precisely the Pu-239 and Pu-241 content within the fissile material, has a higher fission yield for I-129 than the U-235 utilised in standard-type UO<sub>x</sub> fuel (see section 3.2). Therefore, the higher I-129 activity of the UO<sub>x</sub> fuel specimen in contrary to the examined MOX fuel is attributed to the higher burn-up and average linear power. Furthermore, the calculated MCNP values for the rim area display precise activities on the expected iodine inventory at this region, yet they do not take into account a thermal transport process e.g. a *van-Arkel-de-Boer process* during reactor operation. Thus, one may argue, that the I-129 inventory in the peripheral region is even higher than experimental and calculated results.

**Table 5.4:** I-129 inventories [Bq/t<sub>HM</sub>] of the examined rim area fragments of both SNF types and MCNP calculations for distinct regions within the fuel pellet.

Sample	UO <sub>x</sub> -RIM	MOX-RIM	MCNP-RIM	MCNP-CORE
I-129 activity [Bq/t <sub>HM</sub> ]	2.4(±0.3)×10 <sup>9</sup>	2.1(±0.4)×10 <sup>9</sup>	2.7×10 <sup>9</sup>	1.6×10 <sup>9</sup>



**Figure 5.5:** I-129 inventory [Bq/t<sub>HM</sub>] in the rim area of the two SNF specimens in comparison to calculated results by means of MCNP calculations for the outer (RIM) and central (CORE) part of the fuel pellet. Displayed MCNP values for RIM and CORE regions are valid for both fuel types. Regarding the I-129 inventories obtained by calculations, the higher burn-up of the UO<sub>x</sub> fuel is compensated by the higher fission yield due to the elevated initial plutonium content in the MOX fuel.

### 5.1.3 Radionuclide inventories of Zircaloy-4 in contact with spent $UO_x$ or MOX fuel and comparison to calculated inventories

In addition to the  $Cl-36$  activity inventory in the Zircaloy specimens further RN were determined experimentally and compared to calculated results of Zircaloy-4 cladding material applying the MCNP / CINDER codes adjusted to the available fabrication and irradiation history as well as results obtained by Herm and co-workers for the plenum section of the cladding tube of the same fuel rod corrected for decay [HERM *ET AL.*, 2018]. Figure 5.6 depicts the experimentally obtained inventory of the activation products  $Co-60$  and  $Sb-125^{30}$  in comparison to the plenum section inventory and calculated results.

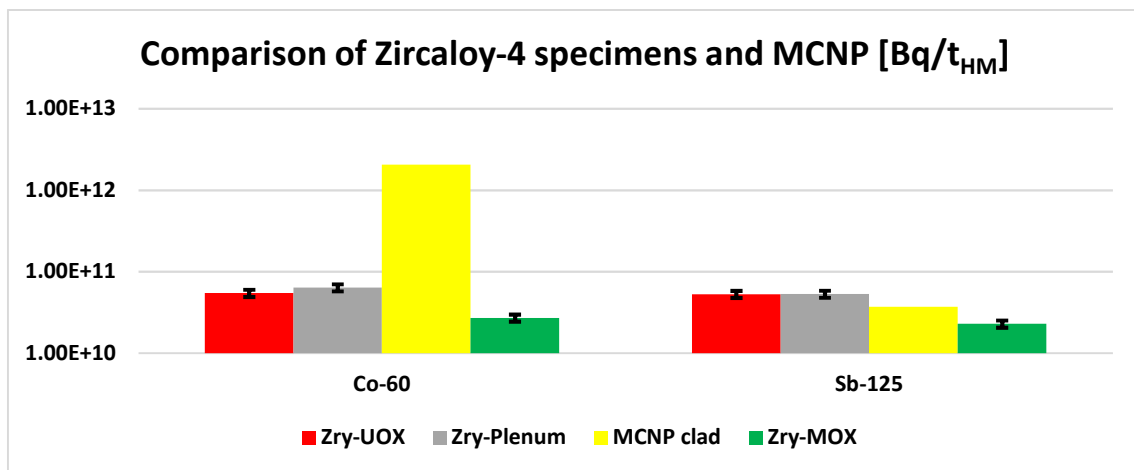


**Figure 5.6:**  $Co-60$  and  $Sb-125$  activation product inventory [Bq/t<sub>HM</sub>] in comparison to MCNP calculations and results obtained by Herm and co-workers for the plenum tube section of the fuel rod segment N0204 [HERM *ET AL.*, 2018].

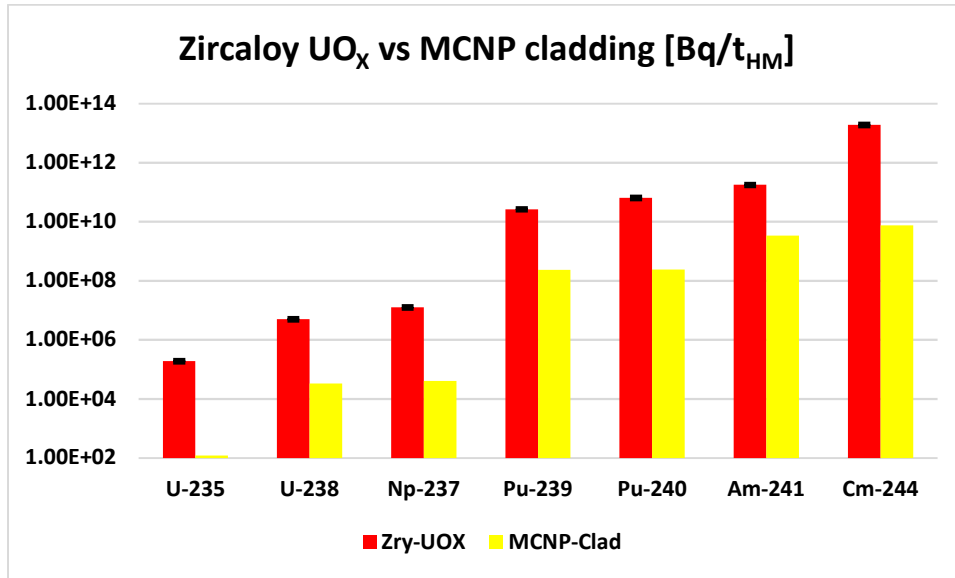
<sup>30</sup> In addition to the neutron activation reaction of  $Sn-124$  to  $Sn-125$  and subsequent  $\beta$  decay to  $Sb-125$ , the antimony isotope is also generated during nuclear fission of uranium or plutonium.

As shown, the results regarding the Zircaloy in contact with the  $\text{UO}_x$  fuel are in good agreement within the analytical uncertainties with the activities obtained from the plenum section for the two activation products. The predicted Co-60 inventory of the cladding material derived from MCNP calculations based on assumed impurities (see table 2.2) is exceeding the experimentally obtained values by far. This suggests that the precursor (either directly due to Co-59 impurities or by neutron activation of iron isotopes with subsequent  $\beta^-$ -decay) for the activation reaction to Co-60 might be overestimated in the cladding material. Contrary to the Co-60 inventory comparison of experimentally and calculated results, the Sb-125 inventories are in good agreement to each other. The examined Zircaloy-4 cladding of the  $\text{UO}_x$  fuel rod specimen was fabricated with an elevated amount of tin, which might be an explanation of the slightly higher activities obtained by experimental analysis (see section 2.2).

In case of the MOX cladding specimen, the Co-60 and Sb-125 activities are slightly lower than for the two samples of the  $\text{UO}_x$  fuel rod due to either the lower burn-up, axial position in the reactor, neutron flux or lesser impurity contents within the cladding material.

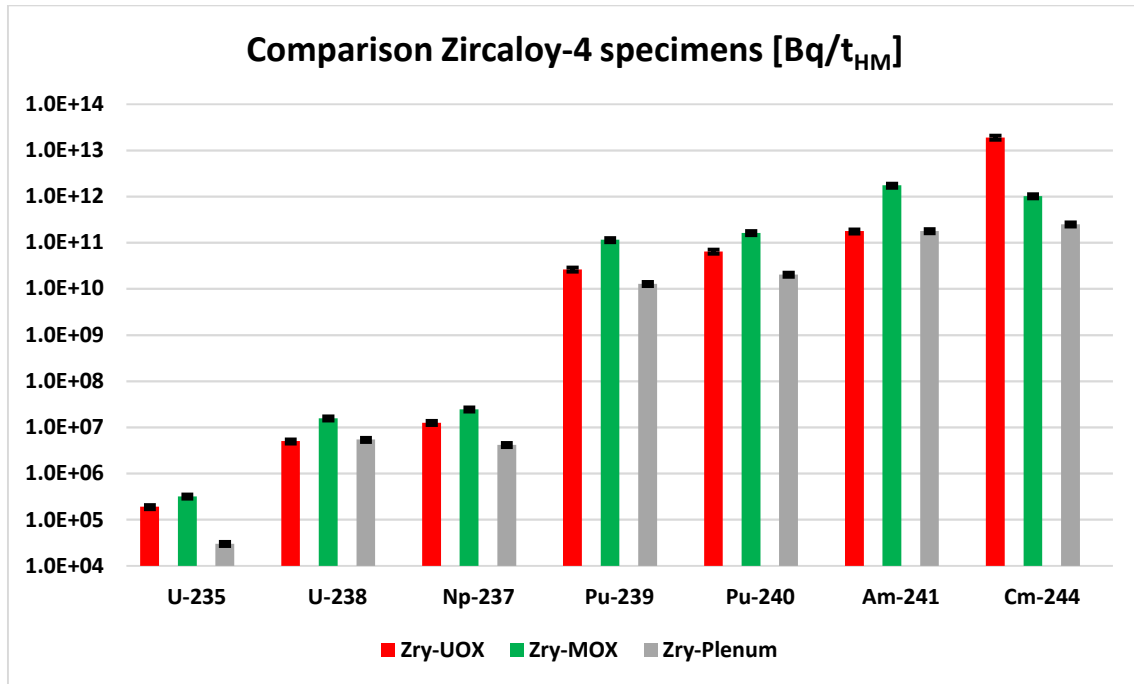
Figure 5.7 shows the experimentally obtained actinide inventory within the Zircaloy in contact with the  $\text{UO}_x$  fuel compared to MCNP / CINDER calculations made for the cladding material. The elevated amounts of uranium and minor actinides within the Zircaloy specimens can be explained by two phenomena: One the one hand, Zircaloy-4 contains up to 3.5 ppm of uranium as an impurity within the material. This uranium impurity can undergo fissions, as well as neutron capture reactions, with the latter resulting in the generation of minor actinides. On the other hand, the experimentally obtained actinide contents can be higher due to residual SNF on the cladding surface, still present after mechanical defueling [HERM *ET AL.*, 2018]. Especially elevated activities of minor actinides in Zircaloy cladding could be a matter of concern for prolonged interim storage and the later conditioning for final disposal, since isotopes such as Cm-242 and Cm-244, among others, contribute mainly to the degradation of the cladding material by irradiation damage through their intense alpha radiation. Within the alpha decay event the

cladding structure is damaged by either the alpha particle itself or the resulting recoil particle as described by Ewing and colleagues [EWING *ET AL.*, 1995].



**Figure 5.7:** Experimentally obtained actinide inventory [Bq/t<sub>HM</sub>] of the Zircaloy specimen previously in contact with the UO<sub>x</sub> fuel compared to MCNP calculations of Zircaloy-4 cladding material with the irradiation conditions adjusted to the examined fuel type.

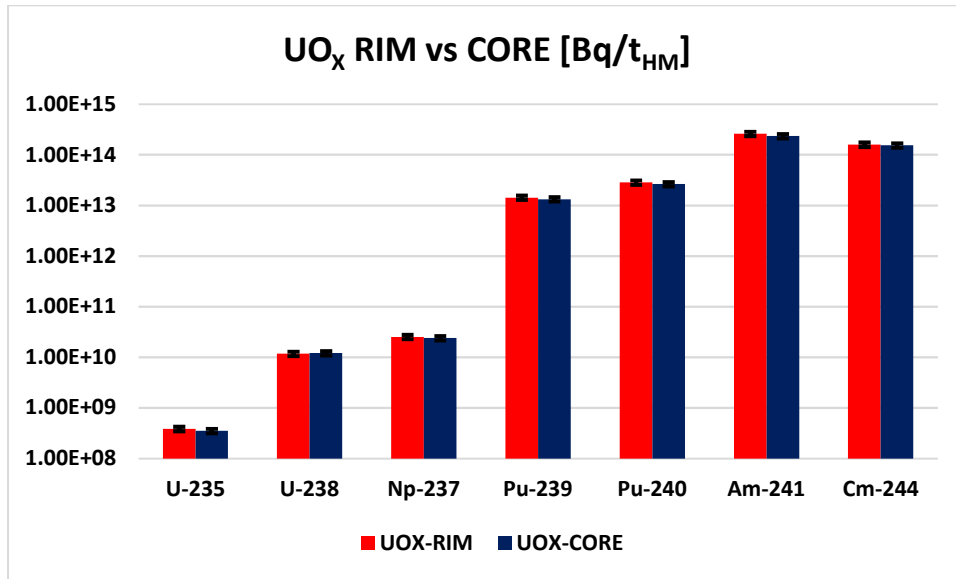
For the examined MOX cladding segment, the actinide inventory is displayed in figure 5.8 along with the results obtained from the UO<sub>x</sub> cladding as well as the activities determined by Herm and colleagues [HERM *ET AL.*, 2018; HERM, 2021]. Contrary to the examined Zircaloy specimen previously in contact with the UO<sub>x</sub> fuel, the MOX cladding features higher activities for all actinides with the exception of Cm-244. In case of U-235, this observation can be explained by lesser uranium fissions due to the lower burn-up and preferred fission of plutonium isotopes in MOX fuel. The higher plutonium content is attributed to the fabrication of the MOX with plutonium as main fissile material and non-enriched uranium as matrix compound. The elevated Cm-244 activity within the Zry-UO<sub>x</sub> sample could be explained by the higher burn-up and greater average linear power of the UO<sub>x</sub> fuel pin contrary to the MOX fuel pin.



**Figure 5.8:** Actinide inventories [Bq/t<sub>HM</sub>] of the Zircaloy specimens in contact with the UO<sub>x</sub> and MOX fuel, as well as the actinide inventories of the plenum section.

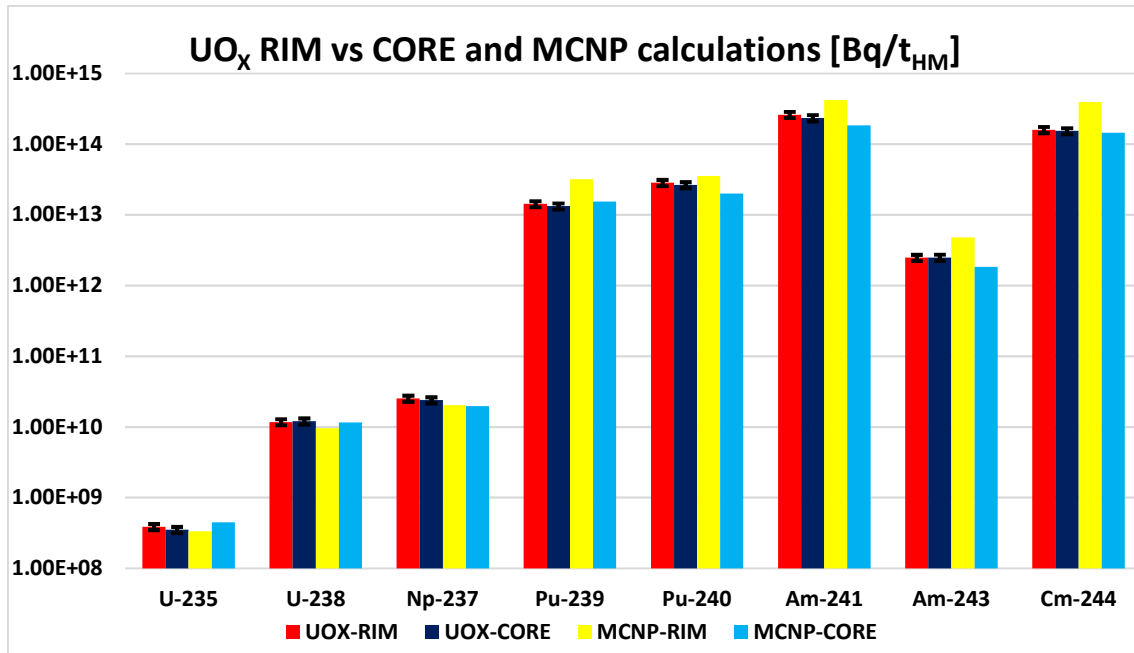
#### 5.1.4 Radionuclide inventory of spent UO<sub>x</sub> and MOX fuel and comparison to calculated results

Figure 5.9 shows the experimental inventory analysis of selected actinides for the cladding adjacent rim and central area of the UO<sub>x</sub> fuel. A slight enrichment effect of the minor actinides in conjunction with a depletion of U-238 can be observed within the UO<sub>x</sub>-RIM specimen which is attributed to the higher neutron resonance in the peripheral part of the SNF pellet. This enrichment effect in the outer part of the SNF denoted as *rim effect* occurs in general within a 100 μm distance from the inner side of the cladding as described by e.g. Grambow and co-workers [GRAMBOW *ET AL.*, 1996].



**Figure 5.9:** Experimentally determined actinide inventories [Bq/t<sub>HM</sub>] for the rim and core region of the examined UO<sub>x</sub> fuel.

Moreover, the experimental actinide inventory obtained for the UO<sub>x</sub> fuel was compared to results derived from MCNP / CINDER calculations for distinct regions in the fuel pellet (see figure 5.10). All in all, the experimental inventory is in good agreement with the expected activities by calculations, yet a clear enrichment effect for the minor actinides is not observed. This could be attributed to the size of the analysed SNF fragments, as the enriched rim layer is expected to have a thickness of 100 μm, which is difficult to sample under hot cell conditions.



**Figure 5.10:** Comparison of selected actinide inventories [Bq/t<sub>HM</sub>] determined experimentally and MCNP calculations performed for distinct regions in the SNF pellet.

The determined fission product inventory for Cs-137, Eu-154 and Eu-155 in the UO<sub>x</sub> fuel is shown in figure 5.11 in comparison to expected results by MCNP / CINDER calculations again for distinct regions within the fuel pellet. As depicted, a slight enrichment of Cs-137 can be seen regarding the experimentally derived data from the pellet rim to the pellet centre. This is attributed to a higher fission yield within the cladding adherent area as well as a transport process of volatile caesium along the fractures within the pellet due to a thermal gradient between the central part of the SNF and the peripheral region in contact with the cladding being cooled by the primary circuit water. For the europium isotopes no enrichment effect was observed in the RIM specimen, which is attributed to the chemistry of fission produced trivalent europium as presumably Eu<sub>2</sub>O<sub>3</sub> not being mobile within the fluorite UO<sub>x</sub> matrix [NEEB, 1997]. Again, the obtained data is in good agreement with the results derived from calculations in the present work.

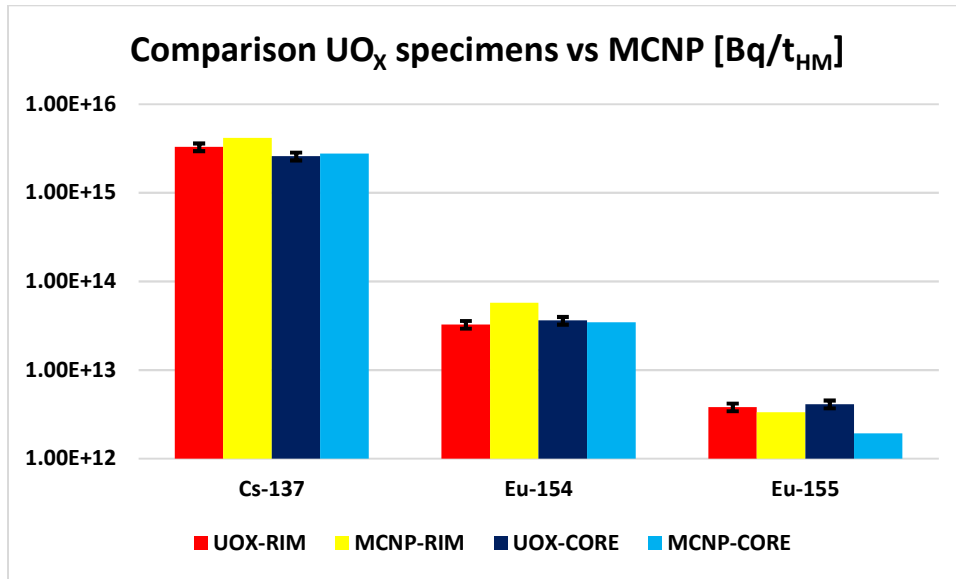


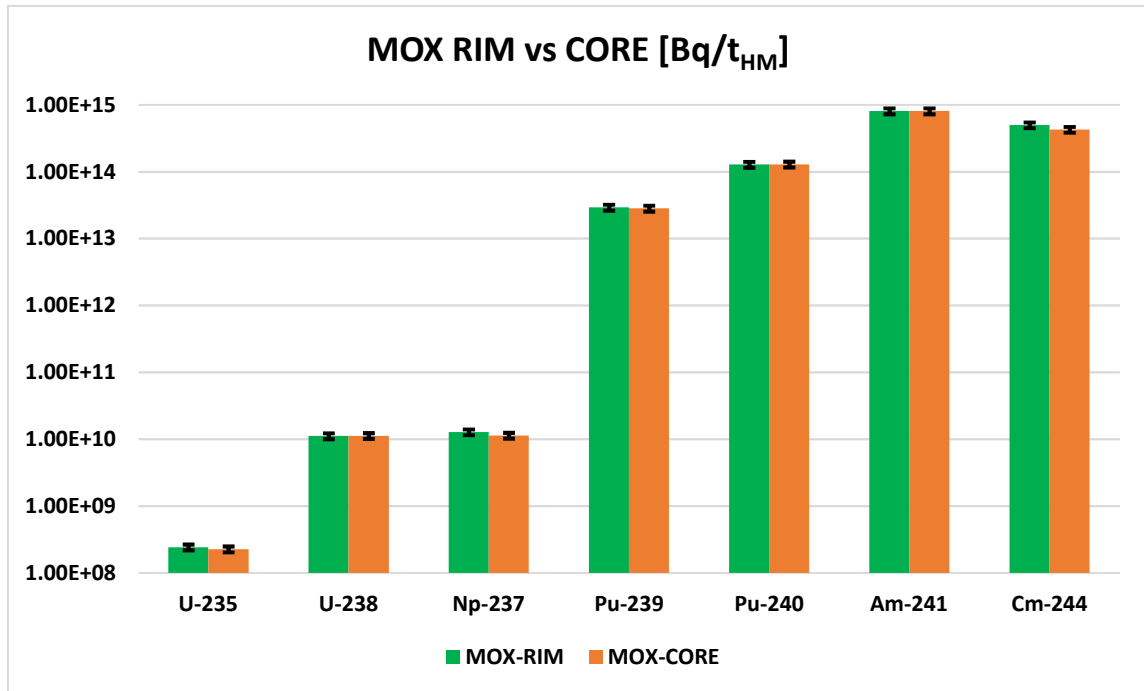
**Figure 5.11:** Comparison of experimentally determined inventory [Bq/t<sub>HM</sub>] of selected fission products in distinct regions of the fuel pellet to MCNP calculations.

Furthermore, the fission gas inventory for an UO<sub>x</sub> fuel fragment digested in a mixture of (NH<sub>4</sub>)<sub>2</sub>CO<sub>3</sub> and H<sub>2</sub>O<sub>2</sub> was determined by use of an autoclave (see table 5.5). For experimentally determined inventory, the prior partial release of fission gases via puncturing test from the plenum of the sealed fuel rod segment performed at the Joint Research Centre Karlsruhe was taken into account [GONZÁLEZ-ROBLES *ET AL.*, 2016]. The obtained concentration of Xe-isotopes is in good accordance with values resulting from MCNP calculations, yet for the Kr-isotopes a significantly higher concentration was detected by gas-MS which might be the result of a contamination of the Ar gas with Kr used for flushing the autoclave beforehand and purging the remaining air out of the vessel. It is also conceivable, that due to the enhanced mobility of Kr-isotopes contrary to Xe-isotopes as described by González-Robles and colleagues, Kr could segregate in another part of the pellet than xenon and thus the results could be biased by a large krypton inclusion leading to elevated values [GONZÁLEZ-ROBLES *ET AL.*, 2016].

**Table 5.5:** Fission gas inventory in mol/g<sub>UO<sub>2</sub></sub> for an alkaline digested fuel fragment of the high burn-up UO<sub>x</sub> fuel in comparison to calculated values.

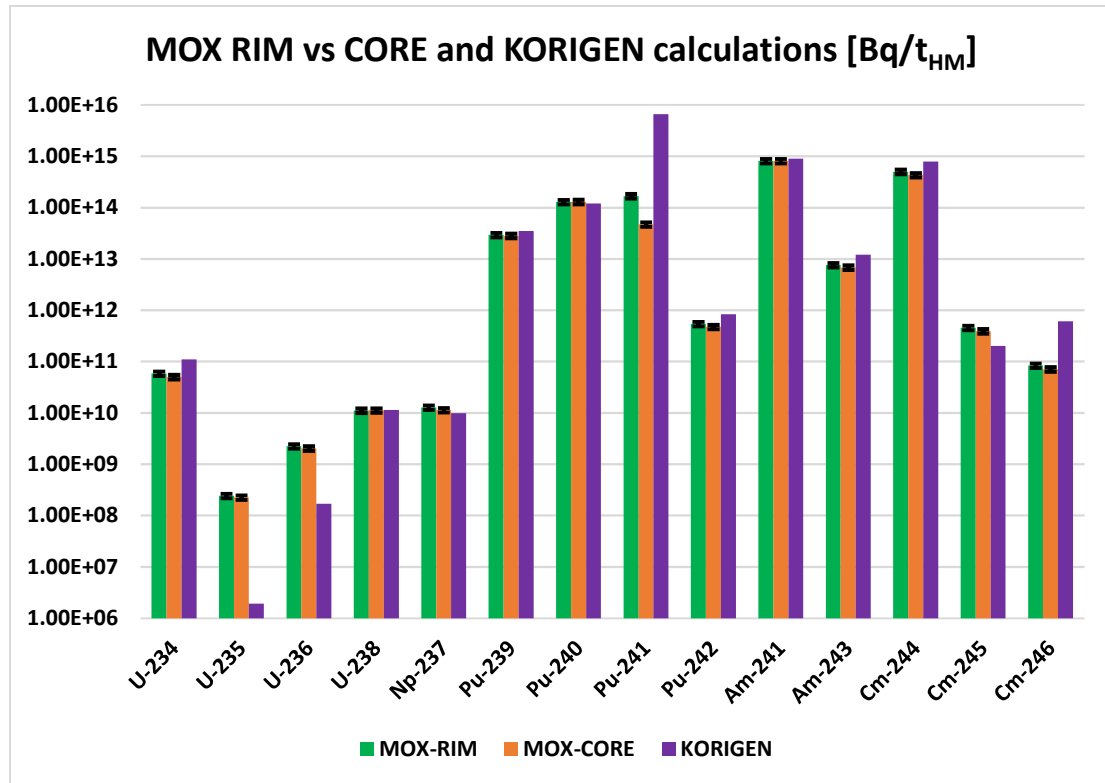
	<b>Kr-isotopes [mol/g<sub>UO<sub>2</sub></sub>]</b>	<b>Xe-isotopes [mol/g<sub>UO<sub>2</sub></sub>]</b>
<b>exp.</b>	3.3(±0.4)×10 <sup>-5</sup>	4.5(±0.3)×10 <sup>-5</sup>
<b>calc.</b>	4.8×10 <sup>-6</sup>	4.8×10 <sup>-5</sup>
<b>ratio (E/C)</b>	6.88±0.81	0.94±0.06

In addition to the inventory analysis of the UO<sub>x</sub> fuel, activities for the MOX fuel were determined likewise and compared to KORIGEN calculations. Figure 5.12 depicts the experimental inventory obtained by acidic digestion of two MOX fragments received from selectively defueling a cut disk of MOX fuel. Actinide inventories of both regions are in good agreement with each other, yet a significant enrichment effect is not observable for the actinides, which might be attributed to the burn-up of 38.0 GWd/t<sub>HM</sub> and thus the lesser evolution of the rim-effect.



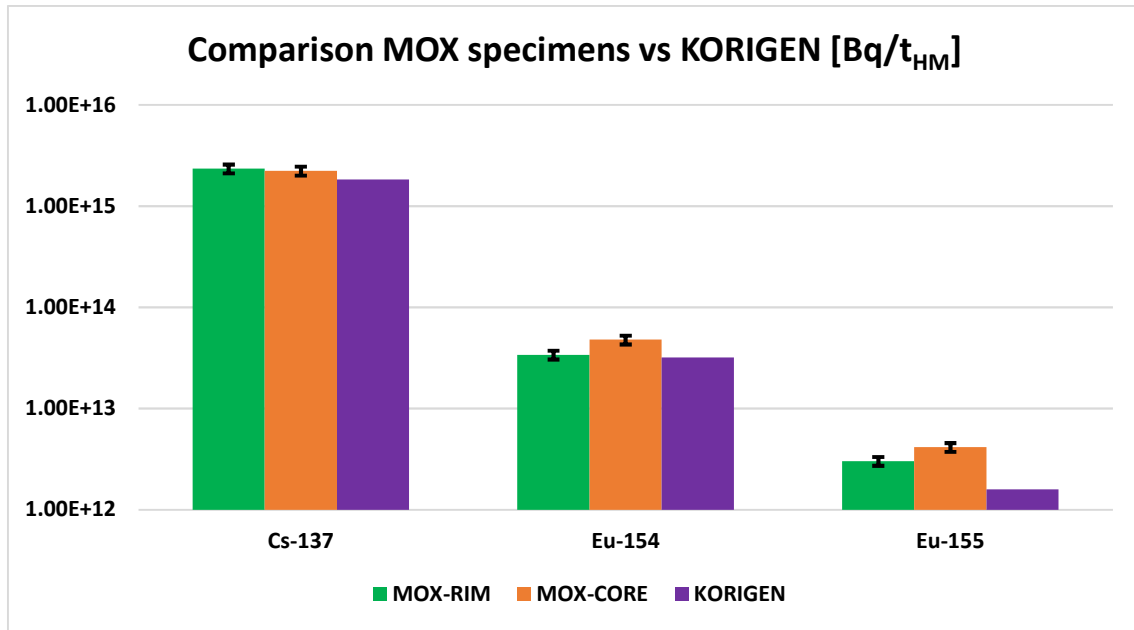
**Figure 5.12:** Actinide inventory [Bq/t<sub>HM</sub>] of a core and rim sample of the MOX fuel specimen.

In figure 5.13 the experimental inventories for both fuel regions are shown with respect to calculations performed with webKORIGEN code adjusted to the reactor and irradiation conditions of the MOX fuel. With exception of the U-235 activity inventory, the results obtained from experimental analysis are in accordance with the expected values obtained from webKORIGEN calculations. A conceivable reason for the differences in U-235 activity between the experimentally derived and calculated data could be that the calculation by MCNP assumes a higher U-235 fission than experimentally observed. The experimentally obtained ratio between U-235 and U-238 of 0.31 % is in agreement with data obtained by former Kraftwerk Union for a 40 GWd/t<sub>HM</sub> MOX fuel with a ratio of 0.33 % [GOLL ET AL., 1988].



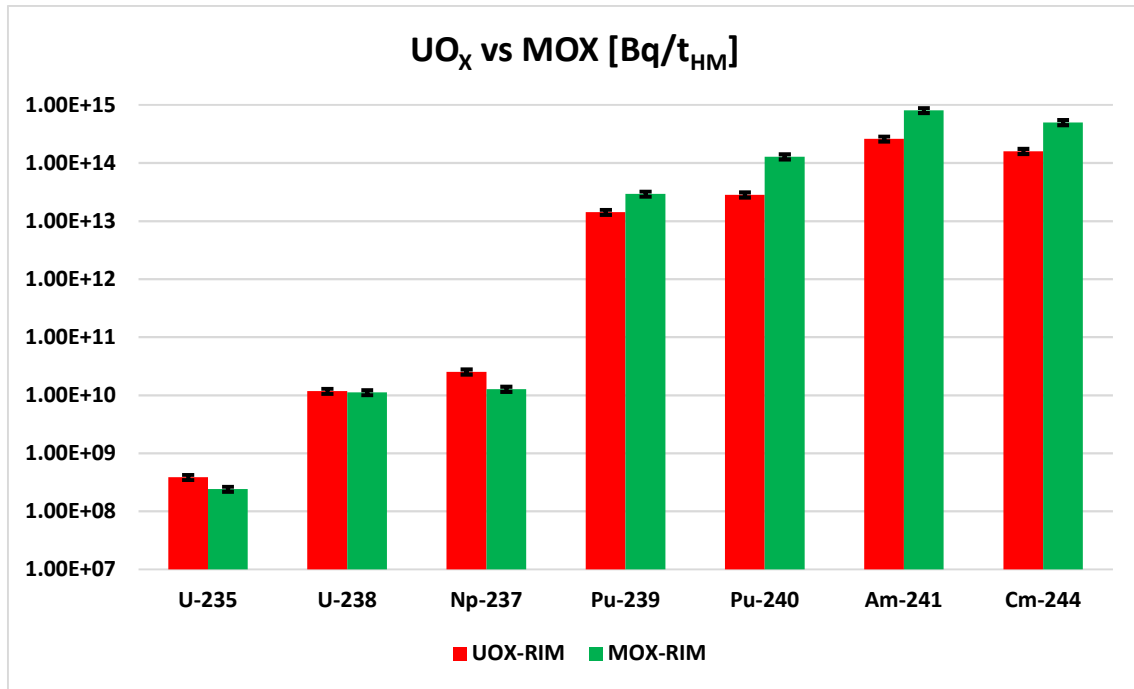
**Figure 5.13:** Comparison of experimental MOX actinide inventories [Bq/t<sub>HM</sub>] to KORIGEN calculations.

Furthermore, for selected fission products the experimentally obtained RN inventory was determined as shown in figure 5.14. For all analysed fission products (Cs-137, Eu-154, Eu-155) the activity is in good agreement to each other as well as to webKORIGEN calculations with no observable enrichment effect of the europium isotopes similar to the high burn-up UO<sub>x</sub> fuel.



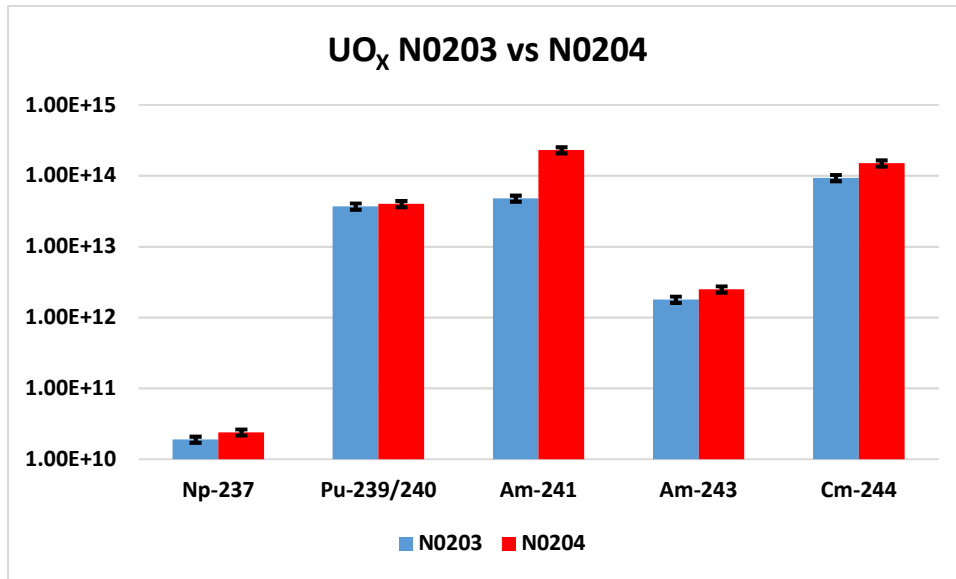
**Figure 5.14:** Selected fission product inventories [Bq/t<sub>HM</sub>] of the MOX fuel specimen and comparison to KORIGEN calculations.

Figure 5.15 shows again for comparison all actinide inventory data for both fuel types, UO<sub>x</sub> and MOX fuel. As already described by e.g. Neeb, a higher amount of minor actinides with the exception of Np-237 can be observed in the MOX fuel specimen, which is attributed to the high initial fissile plutonium concentration in the fuel type [NEEB, 1997]. The U-235 activity in the UO<sub>x</sub> fuel specimen is slightly higher than in the MOX SNF due to an initial enrichment of the respective isotope beforehand.



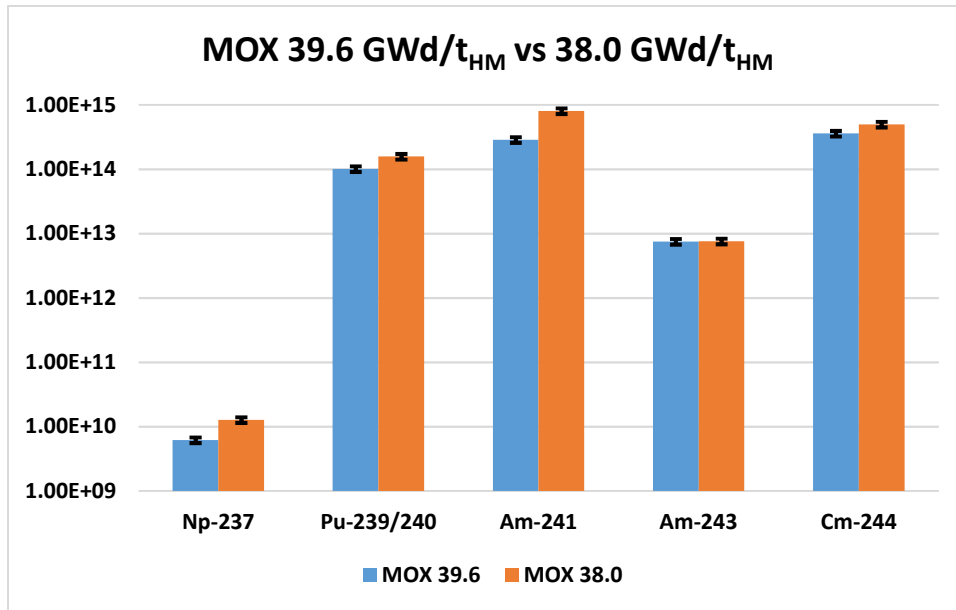
**Figure 5.15:** Actinide inventories [Bq/t<sub>HM</sub>] of the UO<sub>x</sub> and MOX fuel rim specimens compared to each other.

Figure 5.16 depicts a comparison of the obtained overall pellet inventory data for certain actinides within the present work to the actinide inventory derived from previous analyses of the “sister” fuel rod segment N0203 performed by Grambow and co-workers [GRAMBOW *ET AL.*, 1996]. Obtained actinide data by Grambow and colleagues is in good agreement within the analytical uncertainty to the inventory measured during this work with exception of Am-241, which is a decay product of the short-lived plutonium isotope Pu-241 with a half live of only 14.35 years.



**Figure 5.16:** Comparison of actinide inventory [Bq/t<sub>HM</sub>] of the fuel rod segment N0204 (red) examined in the present work and the sister fuel rod segment N0203 (blue) analysed by Grambow and colleagues [GRAMBOW *ET AL.*, 1996].

Moreover, similar to the UO<sub>x</sub> fuel comparison, the MOX fuel actinide inventory was put in contrast to data of a MOX fuel with a burn-up of 39.6 GWd/t<sub>HM</sub> analysed by Loida and colleagues [LOIDA *ET AL.*, 1997]. Loida and co-workers determined the radionuclide inventory of MOX fuel rod 6014, which was irradiated at the PWR Obrigheim under similar conditions and at the same time interval as the examined one in the present work. As depicted in figure 5.17, the inventory data is again in very good agreement to each other with the exception of Am-241 for reasons already stated for the UO<sub>x</sub> fuel segment, i.e. Pu-241 decayed to Am-241.



**Figure 5.17:** Comparison of the actinide inventory [Bq/t<sub>HM</sub>] of the examined MOX fuel rod segment with a burn-up of 38.0 GWd/t<sub>HM</sub> and a MOX fuel rod segment irradiated to a burn-up of 39.6 GWd/t<sub>HM</sub> during the same reactor cycle analysed by Loida and co-workers [LOIDA ET AL., 1997].

### 5.1.5 Conclusions regarding the RN inventory determination of high active waste specimens

In this subsection, RN inventories in different SNF specimens were determined with particular respect to isotopes relevant for safety analyses for final disposal of SNF as well as radionuclides with potential impact on the degradation of SNF assemblies during an inevitable long-term interim storage. With the goal of getting further insights into enrichment effects of minor actinides, fission products or activation products within the fuel-cladding interface layer by analysing cladding specimens with fuel residue upon them as well as fuel fragments from the cladding adjacent area obtained after selectively

defueling SNF pellets. For further comparison of the obtained data, the experimental inventories were compared to expected values derived from MCNP / CINDER or webKORIGEN calculations with respect to the fuel type, irradiation histories and available data on the fuel rods.

In general, a good agreement of the experimental data, either among each other or with calculated results is obtained, proving the robust analytical methods utilised for measurements. For certain isotopes, e.g. Co-60, the experimentally determined activity is significantly lower than expected by MCNP / CINDER calculations, which might result in the overestimation of the precursor impurity within the Zircaloy cladding for Co-60 generation or an uncertainty in the nuclear data cross-section.

For the volatile isotopes Cl-36 and I-129, a separation method was developed for SNF and Zircaloy cladding in order to monitor their occurrence within the spent fuel pellet and to assess their implication on interim storage and final disposal of SNF. Especially for Cl-36 generation during the irradiation of LWR fuel rods, the available data is scarce or solely relying on calculations. The obtained recovery yields of the applied separation technique on either the fuel or cladding specimens show its reliability for the separation of Cl-36 and I-129 from these utter complex matrices. For I-129, the calculated data is very robust and profound, since its generation is solely a result of nuclear fission of plutonium or uranium within the nuclear fuel. The partitioning of iodine within the nuclear fuel pellet though is still afflicted with uncertainties since activation calculations only imply the elevated fissions in the cladding adherent area of the nuclear fuel, yet not the possibility of a temperature driven transport process during reactor operation with subsequent depletion of iodine in the core area and consecutive enrichment in the periphery of the pellet. Therefore, SNF fragments originating from the cladding adherent zone were selected for I-129 analysis showing an enrichment regarding calculated values obtained for the central part of the nuclear fuel pellet.

Contrary to the fission product I-129, Cl-36 is not generated as a result of nuclear fission due to its lower atomic mass. At this, the initial impurity in the material of its main precursor Cl-35 and to some extent K-39 and S-34 is decisive for a profound assessment

of the amount of Cl-36 within the fuel and cladding. Available data in open literature for these precursor isotopes in the nuclear material are unfortunately very deficient and poorly known as many manufacturers yet only provide upper maximum values.

In case of safety analyses regarding cladding degradation effects induced by the halogens or caesium isotopes during interim storage, as well as assessments of RN source terms for long-term safety analyses, precise knowledge on the amount and chemical behaviour of these crucial elements is important as their generation is depending on a large variety of different factors such as fuel type, burn-up, linear power rate or neutron flux.

For further studies, the developed separation technique can be utilised to analyse the Cl-36 content in other irradiated waste specimens as e.g. structural parts of the reactor core or the stainless steel plenum spring holding the fuel stack in place during irradiation. In addition, it is anticipated to analyse Cl-36 release from SNF leaching experiments in order to monitor the release behaviour of Cl-36 in case of container breach in a DGR and put it into contrast to the release behaviour of other mobile radionuclides, such as I-129.

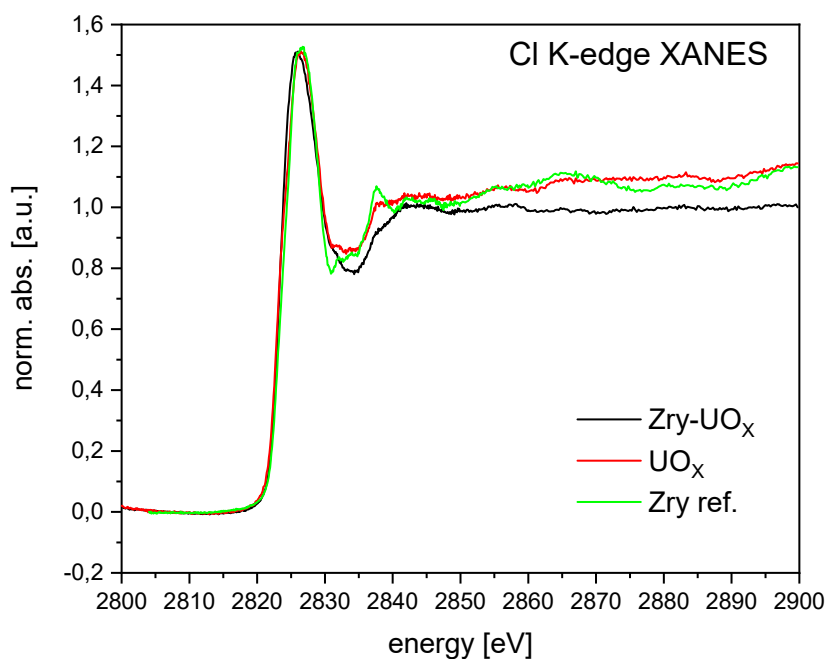
## **5.2 Microscopic and spectroscopic investigations on irradiated $\text{UO}_x$ and MOX fuel and their respective fuel-cladding interfaces**

Complementary to the radiochemical determination of the nuclide inventory within the respective fuel and cladding specimens, microscopic and spectroscopic investigations of the fuel residue on the Zircaloy-4 cladding as well as for the fuel previously in contact with the cladding itself were performed. Therefore, various spectroscopic methods were utilised for the determination and analysis of the pellet-cladding interface.

### **5.2.1 XAS investigations on the interaction layer between fuel and cladding**

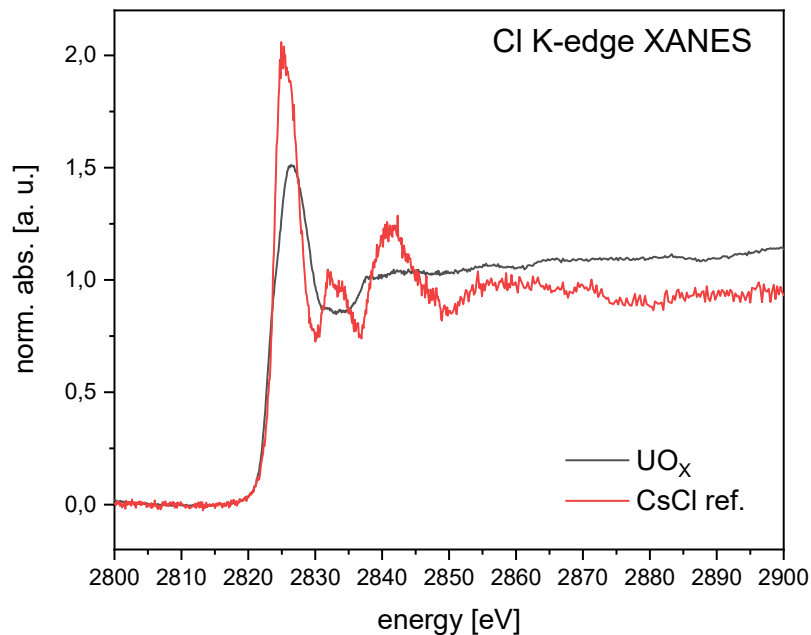
In order to investigate the inventory and the occurrence of Cl and I species in the fuel samples from the pellet periphery as well as in the fuel residue attached to the Zircaloy specimen, Cl and I K-edge measurements were performed together with the respective beamline scientists. All single recorded spectra can be found in figure B.1 and B.2 in the appendix of this thesis (see appendix B).

Figure 5.18 shows recorded normalised Cl K-edge XANES spectra for a fuel fragment and a cladding segment from the high burn-up  $\text{UO}_x$  fuel, as well as an unirradiated reactor-grade Zircaloy-4 specimen.



**Figure 5.18:** Cl K-edge XANES spectra for a fuel fragment from the previously closed gap (red), a Zircaloy cladding segment with fuel residue (black) and an unirradiated Zircaloy-4 specimen (green).

A clear similarity of the individual spectra is obvious for their edge positions. Yet, compared to the unirradiated Zircaloy-4 specimen, the SNF samples feature less characteristic features after the white line, which might result from a “dampening” of the signal due to the  $\text{UO}_x$  matrix or by the formation of another Cl bearing compound throughout the irradiation period of the fuel. In addition, a CsCl reference spectrum was recorded in order to evaluate the formation of a caesium chloride compound similar to the conceivable CsI in case of iodine (see section 2.5). Figure 5.19 shows the recorded CsCl K-edge XANES spectra, which shows little to no similarity to the  $\text{UO}_x$  Cl compound of the fuel.



**Figure 5.19:** Cl K-edge XANES of the fuel fragment (black) in comparison to a CsCl reference (red).

A change in edge structure is depicted regarding the pre-absorption edge of the UO<sub>x</sub> specimen, where a shoulder at 2823.6 eV can be observed. A similar feature was described by Pipon and colleagues during experiments on the thermal diffusion of chlorine in UO<sub>2</sub> [PIPON *ET AL.*, 2006], indicating that chlorine migrates similar to iodine from the pellet centre and gathers at the rim zone. The differences between the edge structures of the irradiated Zircaloy and UO<sub>x</sub> specimen could be explained by the amount of chlorine gathered in the respective zone of the SNF. As Pipon and co-workers stated, in largely chlorine enriched spots, a single peak structure will evolve, whereas in less enriched areas the structure of the spectrum is characterised by a double peak [PIPON *ET AL.*, 2006]. Figure 5.20 compares the spectra highlighting the position of the shoulder at 2823.6 eV.

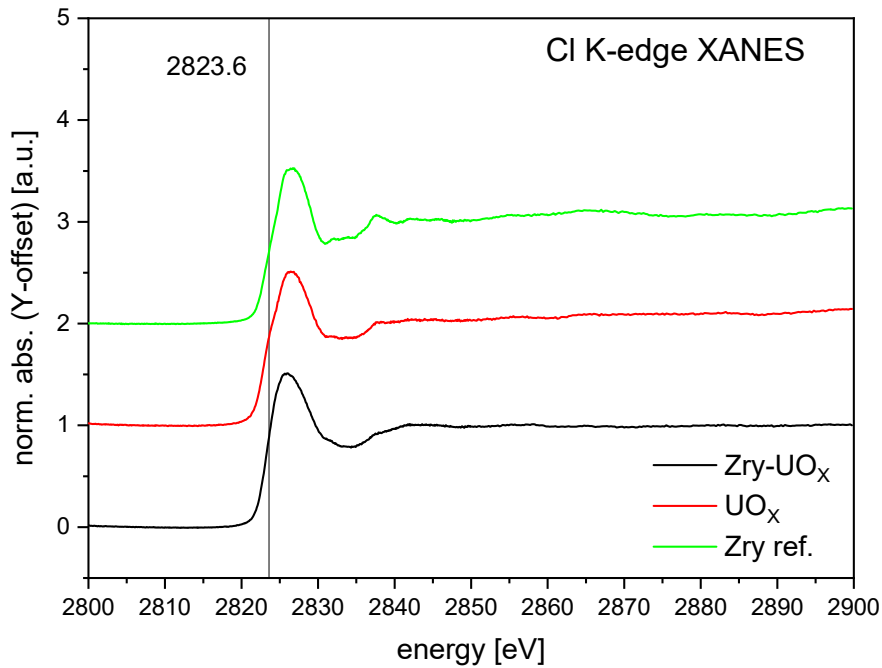


**Figure 5.20:** Cl K-edge XANES spectra with Y-offset. For the UO<sub>x</sub> fuel sample (red), a shoulder can be seen before the edge peak, whereas the Zircaloy specimens (black and green) display a featureless edge jump.

For the Cl K-edge XANES measurement of the MOX fuel fragment as well as for the Zircaloy segment with fuel residue upon the surface, a high amount of ruthenium was observed resulting in an intense L3 peak next to the K-edge chlorine peak as shown in figure 5.21 and figure 5.22. The occurrence of this elevated quantity of ruthenium on both MOX samples is attributed to two conceivable reasons. Pu-239 has a higher fission yield in comparison to U-235 for the respective ruthenium isotopes and as the more prominent explanation, the analysed specimens had a higher quantity of  $\epsilon$ -particles present on the measured spot examined by the incident synchrotron beam.

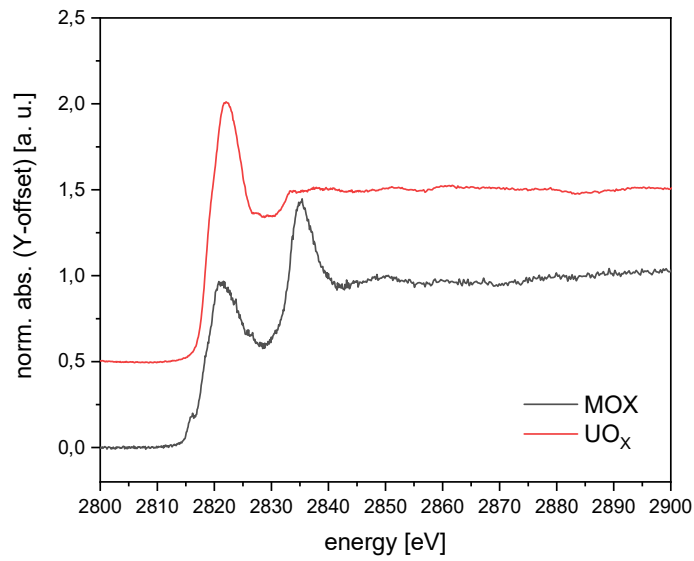


**Figure 5.21:** Cl K-edge XANES spectra of a MOX fuel fragment (black) in comparison to the UO<sub>x</sub> fuel fragment (red). The intense L3 peak of ruthenium at 2835.4 eV is observed within the MOX XANES spectrum indicating the presence of  $\epsilon$ -particle phases.

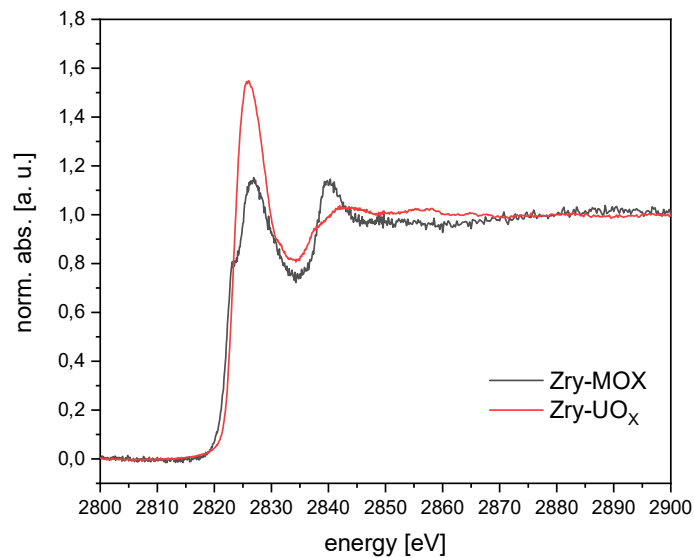


**Figure 5.22:** Cl K-edge XANES spectra of both Zircaloy claddings previously in contact with the respective fuel type.

For I K-edge measurements, the respective samples were transported to the adjacent beamline for actinide science at the KARA synchrotron facility and measured at higher incident energies. Figure 5.23 shows the recorded I K-edge XANES spectra of the MOX fuel fragment and Zircaloy segment in addition to a reference CsI sample.

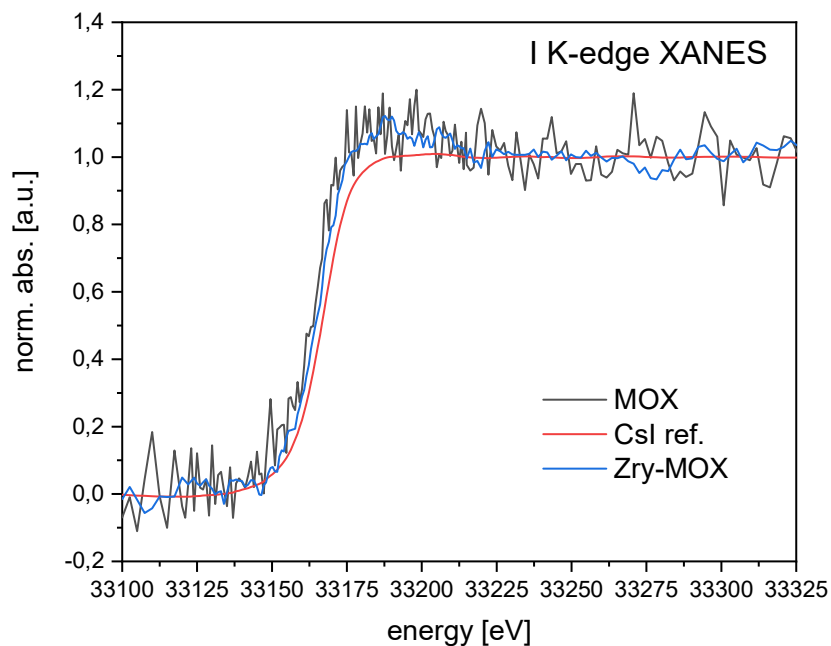


**Figure 5.23:** I K-edge XANES of a MOX fuel fragment (black) and cladding specimen (blue) compared to a CsI reference spectrum (red).

Due to the low amount of generated fission product iodine, the recorded spectra are characterised by a higher signal-to-noise ratio, compared to the reference CsI spectrum. Yet, as predicted in the literature by Cubicciotti and Sanecki as well as Yaggee, Mattas and Neimark [CUBICCIOTTI AND SANECKI, 1978; YAGGEE *ET AL.*, 1980], it is conceivable, that the iodine species formed inside the fuel and adjacent interaction layer, resembles the iodide within the CsI compound. Furthermore, the lower noise level within the Zry-MOX specimen could indicate a higher I content at the pellet-cladding interface than in the actual SNF sample. Figure 5.24 depicts reference spectra recorded by Reed and co-

workers for different iodine species, i.e. iodide, iodate, periodate as well as molecular iodine, indicating that neither  $\text{IO}_3^-$  nor  $\text{IO}_4^-$  is formed within the respective SNF samples, hence both anionic species have characteristic white line features, which are not observable in the displayed iodine spectra in figure 5.23 [REED *ET AL.*, 2002]

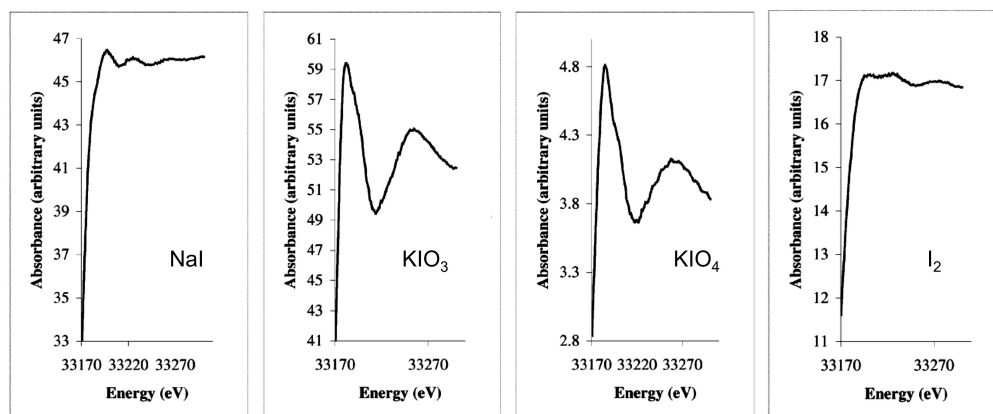


**Figure 5.24:** K-edge XANES spectra of different iodine species measured and published by Reed and colleagues [REED *ET AL.*, 2002].

Figure 5.25 shows both the recorded I K-edge XANES spectrum for the MOX fuel and the  $\text{UO}_x$  fuel in comparison to each other in order to scrutinise whether an iodide or caesium-iodine bearing compound, e.g. CsI is formed at the pellet-cladding interfaces for both fuel types. As depicted, both recorded XANES spectra show similarities to each other, confirming the presence of an iodide species. Especially for the I K-edge XANES measurements of the fuel fragments it must be noted that due to the elevated radioactivity and omnipresent  $\text{UO}_x$  or MOX matrices, the recorded spectra experience a very high noise level, therefore making further examinations by e.g. extended X-ray absorption fine structure (EXAFS) analysis for precise determination of the chemical environment challenging.

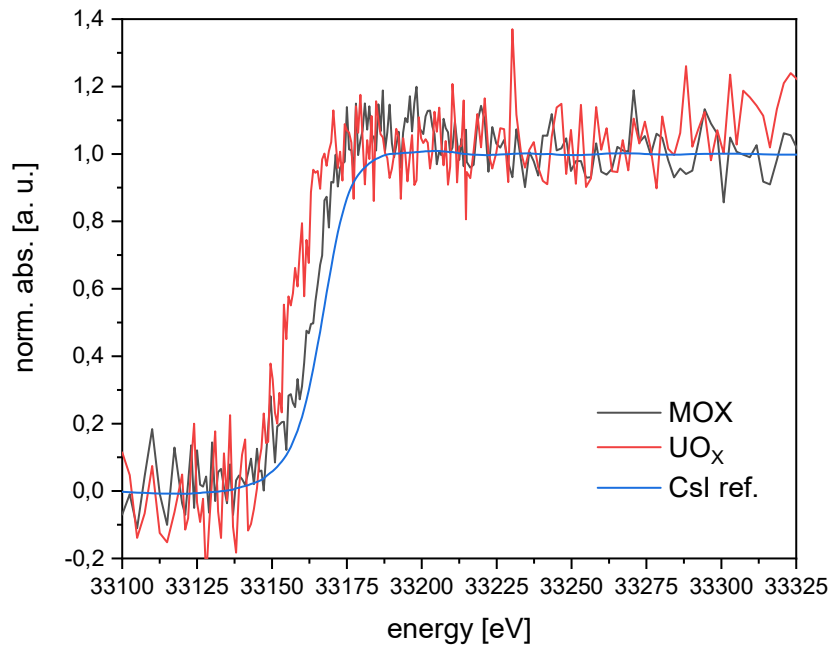


**Figure 5.25:** I K-edge XANES spectra of the CsI reference (blue) and fuel fragments for  $\text{UO}_x$  (red) and MOX (black) SNF in comparison to each other. A shift in the absorption edge between  $\text{UO}_x$  and MOX fuel specimens is visible.

## 5.2.2 SEM-EDS / -WDS analysis of $\text{UO}_x$ and MOX cladding specimens

Figure 5.26 depicts a SEM-EDS analysis of residual  $\text{UO}_x$  fuel upon a previously cut Zircaloy-4 cladding sample. The crystalline precipitate present upon the surface could be identified as a mixed compound of uranium, caesium, oxygen and chlorine. Caesium is mobile during reactor operation and follows the radial thermal gradient in the fuel pellet resulting in an enrichment at the rim area adjacent to the colder cladding being in contact with the coolant [DEGUELDRE *ET AL.*, 2016]. During this vapour transport process, it is expected that initially formed caesium halides (e.g.  $\text{CsCl}$ ,  $\text{CsI}$ ) precipitate at the pellet

## Results and Discussion

periphery. The possible formation of caesium uranates (e.g.  $\text{Cs}_2\text{UO}_4$  or  $\text{Cs}_2\text{U}_4\text{O}_{12}$ ), in conjunction with the corresponding caesium zirconates and molybdates<sup>31</sup> is depending on the local oxygen potential. Götzmann, Matzke as well as Kleykamp predicted the formation of the corresponding caesium uranates due to the increased oxygen potential by oxidation of the fission product molybdenum and the formation of the interaction layer [GÖTZMANN, 1979; KLEYKAMP, 1979; MATZKE, 1995]. It is conceivable that the formed caesium uranates incorporate chlorine into their structure resulting in chlorine-bearing mixed phases of the elements mentioned above. This could be an explanation of the Cl K-edge spectra obtained in the previous sub-section differing from the expected CsCl form.

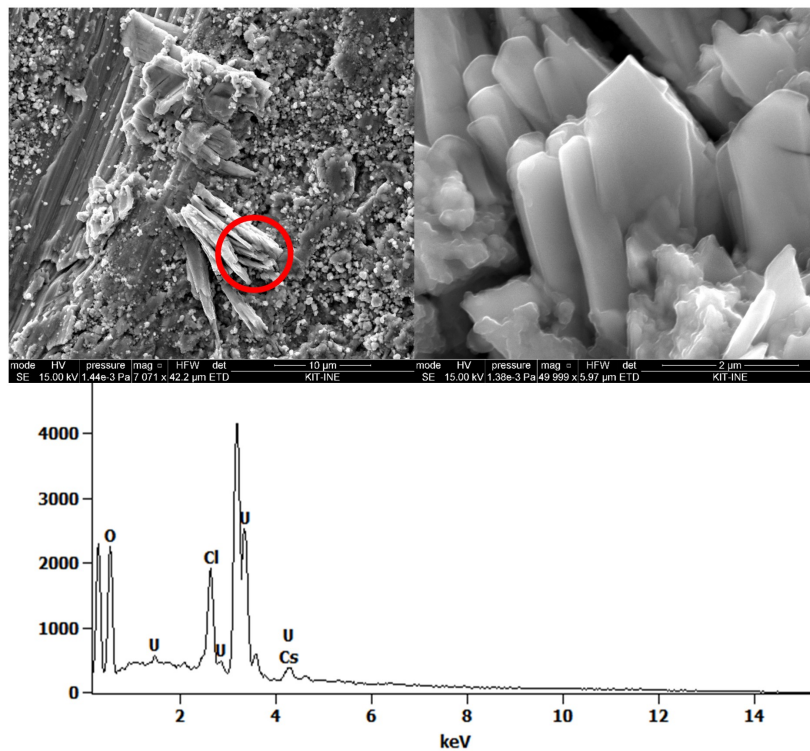


**Figure 5.26:** SEM-EDS analysis of crystalline precipitates on irradiated Zircaloy cladding in contact with spent  $\text{UO}_x$  fuel.

<sup>31</sup> It is assumed, that possible formed caesium molybdates were dissolved during the preparation and washing process of the Zircaloy specimens.

Complementary to the EDS analysis of the Zircaloy-4 cladding in contact with the  $UO_x$  fuel, results for the MOX cladding are shown in figure 5.27 whereas the examined area is indicated by the red rectangle. The depicted figure is shown in Z-contrast mode, displaying heavier elements as bright spots (fuel residue) compared to the darker areas (Zircaloy) visible. Chemical analysis of the examined area reveals a mixed compound of fission products tellurium and caesium together with uranium and zirconium as well as chlorine, which was already seen in the  $UO_x$  cladding specimen. The obtained data would also indicate an uranate / zirconate structure with the respective fission products and chlorine to be present within the interaction layer.

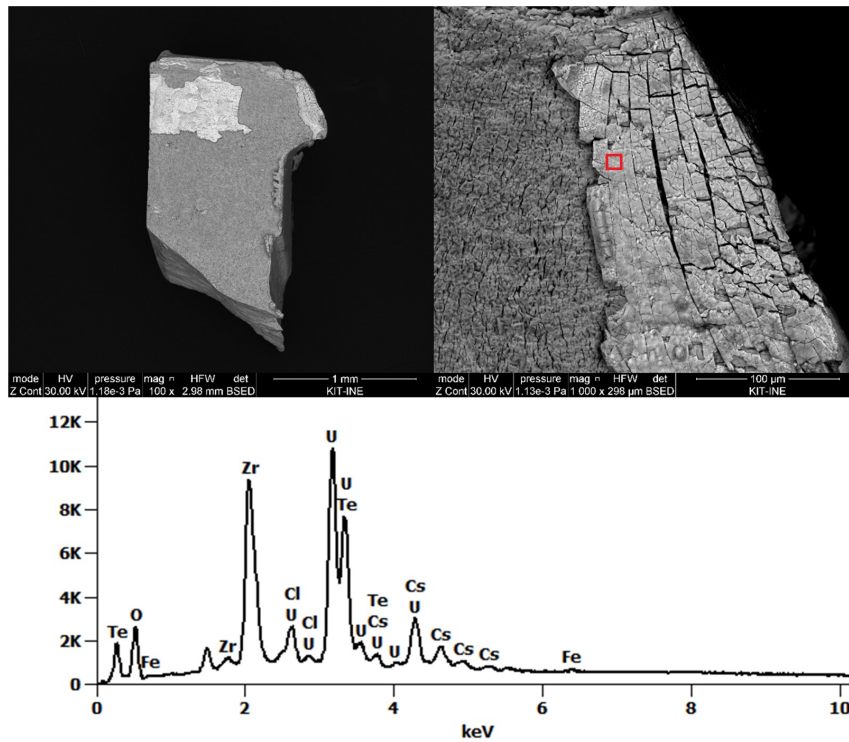


**Figure 5.27:** EDS analysis and SEM pictures of the interaction layer upon the Zircaloy surface for the MOX cladding specimen.

## Results and Discussion

---

Tellurium is suspected to cause cladding attack in its telluride form ( $\text{Cs}_2\text{Te}$ ,  $\text{Cs}_2\text{TeO}_3$ ,  $\text{CdTe}$ , etc.) and is enriched in a similar manner as caesium or iodine due to the radial temperature gradient in the cladding-fuel-system [GÖTZMANN, 1979].

Furthermore, SEM-EDS images and measurements were conducted on an alkaline defueled Zircaloy specimen of the high burn-up  $\text{UO}_x$  fuel in order to investigate the residual fuel-cladding interaction layer upon the surface as depicted in figure 5.28.

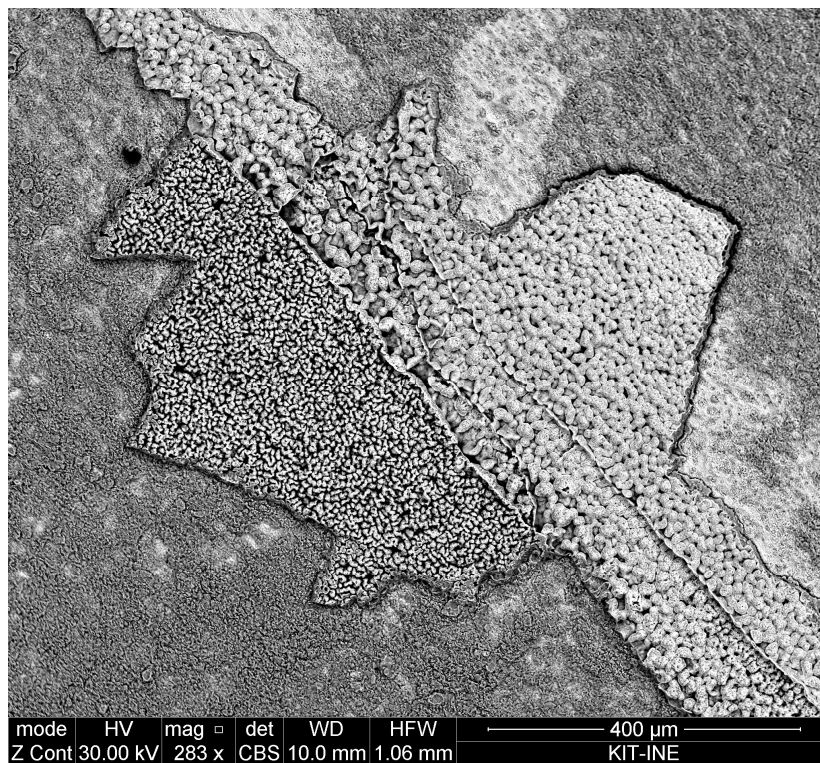


**Figure 5.28:** Zircaloy surface and residual layer on the alkaline defueled high burn-up  $\text{UO}_x$  fuel measured in backscatter-electron mode at an electron acceleration voltage of 30 kV.

Three distinguishable regions can be identified from the shown surface with the initial Zircaloy cladding being oxidised to  $\text{ZrO}_2$ , as well as two fuel layers with different crystallinity. In order to gain information on the composition of the individual areas on the cladding segment, an elemental mapping was performed (see figure 5.29).

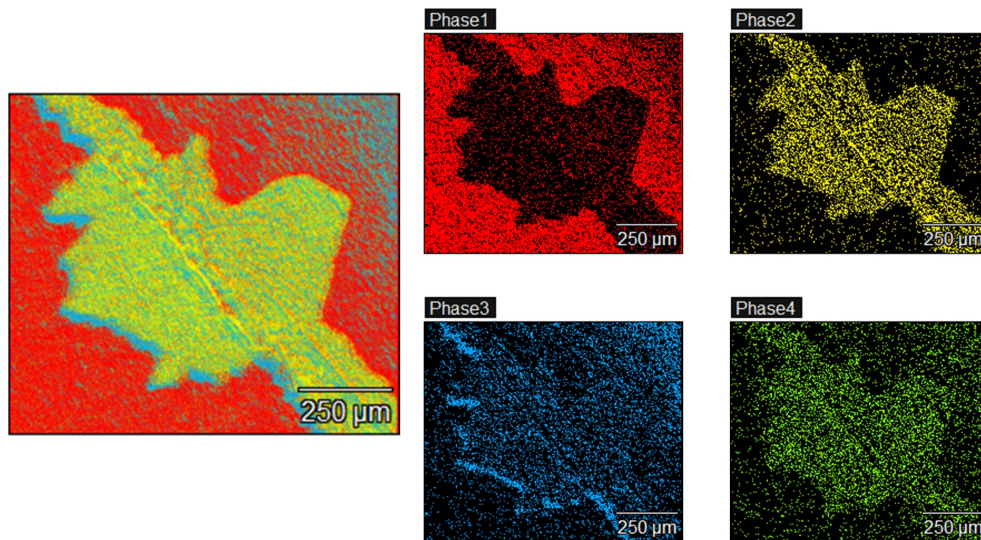


**Figure 5.29:** Elemental mapping of the alkaline defueled high burn-up  $\text{UO}_x$  fuel Zircaloy with a magnification of  $250\ \mu\text{m}$ . Left picture depicts the overall mapping with the Zircaloy in red colour and the fuel residue in blue, green and yellow colour. Pictures on the right side show the different identified areas on the cladding sample with different stoichiometric compositions. Phase 1 depicts the oxidised Zircaloy cladding as  $\text{ZrO}_2$  in red colour. Phase 2 in yellow shows a mixed phase of zirconium and uranium with fission products such as barium, caesium and neodymium. The phase 3 (blue) depicts the Zr content in the fuel residue and phase 4 (green) shows the residual uranium on the surface after defueling.

Four different phases were identified with respect to their elemental composition. The atomic composition of the identified phases with respect to uncertainties is given in table C.1 – C.4 in the appendix section of the present document. Measurements in the yellow coloured, fission-product rich region revealed iodine and chlorine bearing crystalline agglomerates upon the residual interaction layer (see figure 5.30). Chemical analysis of the deposits indicates a crystalline precipitate consisting of barium, tellurium, iodine and chlorine in presence of the residual contaminants uranium, zirconium and oxygen, whereas possible initially present caesium was most likely dissolved during the alkaline defueling process in  $(\text{NH}_4)_2\text{CO}_3$  and  $\text{H}_2\text{O}_2$  (see section 4.3). Atomic composition of the agglomerate is given in table 5.6. The high amount of carbon on the analysed deposit is

## Results and Discussion

due to the preparation process of the SEM sample by carbon sputtering and prior dissolution of the sample in the carbonate rich liquor.

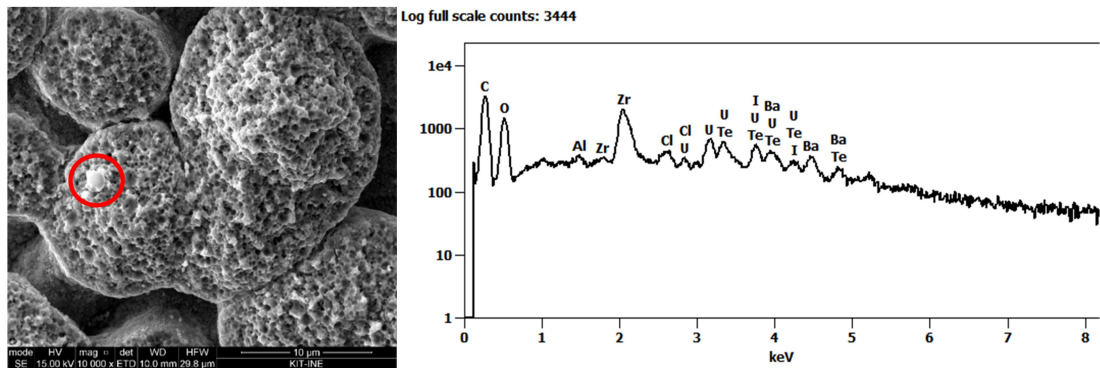
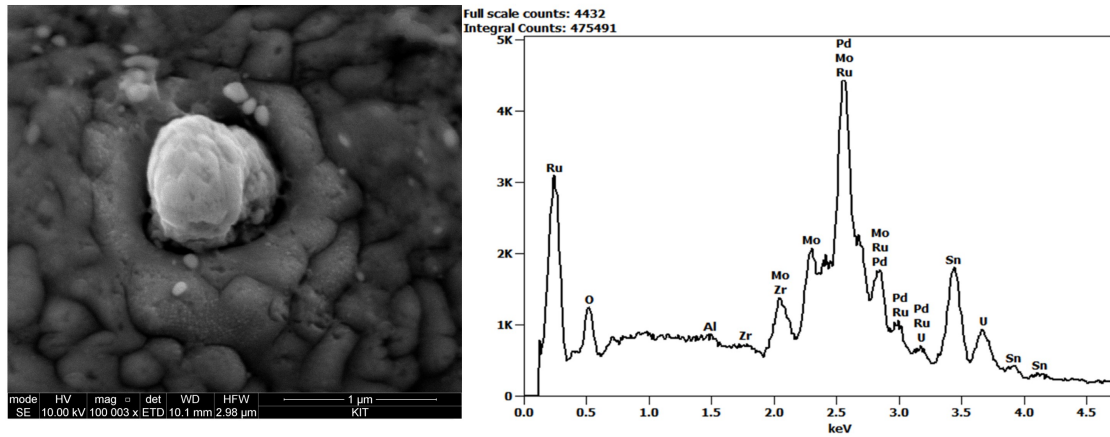


**Figure 5.30:** Deposit of chlorine and iodine bearing crystalline compound on defueled Zircaloy layer indicated by red circle.

**Table 5.6:** Atomic composition and uncertainties in atom % of the chlorine and iodine bearing agglomerate within the interaction layer of the defueled Zircaloy specimen.

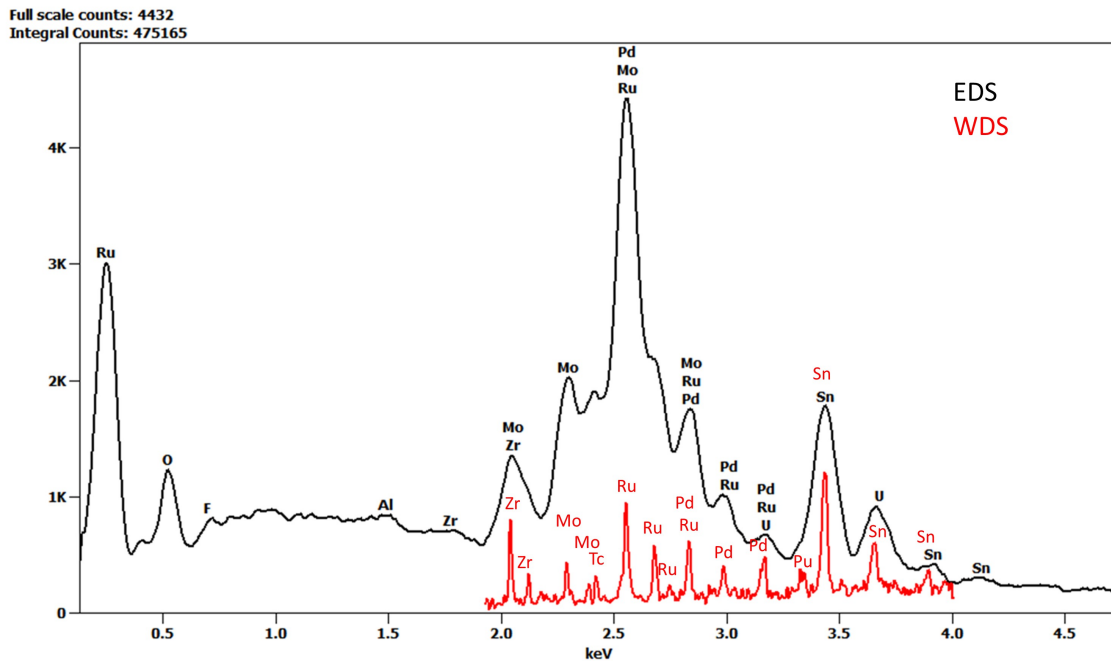
Element	C	O	Cl	Zr	Te	I	Ba	U
atom %	51.1±1.1	34.4±1.4	0.8±0.2	6.0±0.2	2.7±0.5	1.9±0.5	1.2±0.2	1.4±0.1

Complementary to the iodine and chlorine enriched deposits,  $\epsilon$ -particle agglomerates could be identified within the interaction layer as shown in figure 5.31.



**Figure 5.31:** Epsilon particle agglomerate on the interaction layer of the defueled Zircaloy surface.

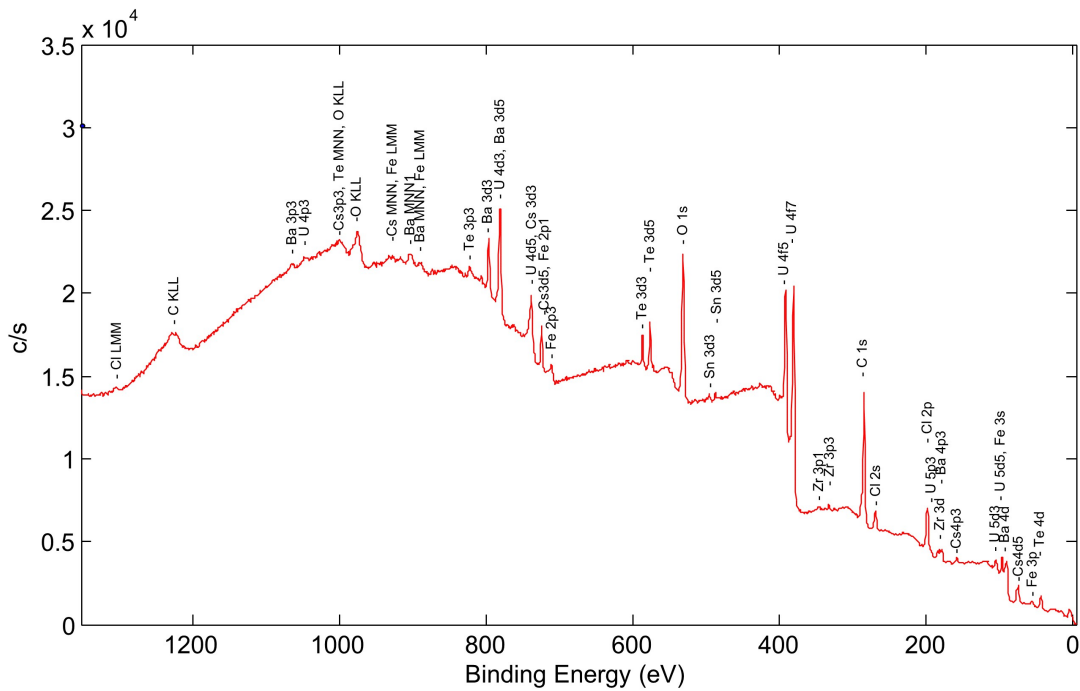
$\epsilon$ -particles consists largely of noble metals, such as Pd and Ru. In a DGR, these metallic  $\epsilon$ -particles may act as a redox catalyst in the event of anoxic corrosion of the SNF surrounding iron cask as described by Cui and colleagues [CUI *ET AL.*, 2010]. For further determination of these particles, a wavelength dispersive X-ray spectroscopic analysis (WDS) was performed resulting in the spectra depicted in figure 5.32. Due to the better discrimination achieved by SEM-WDS, technetium inclusions in the  $\epsilon$ -particles could be detected as expected according to literature [BUCK *ET AL.*, 2015; PELLEGRINI *ET AL.*, 2019].



**Figure 5.32:** Recorded WDS spectrum in comparison to the EDS spectrum. Due to the better discrimination of WDS, a more precise determination of the  $\epsilon$ -particles was achieved.

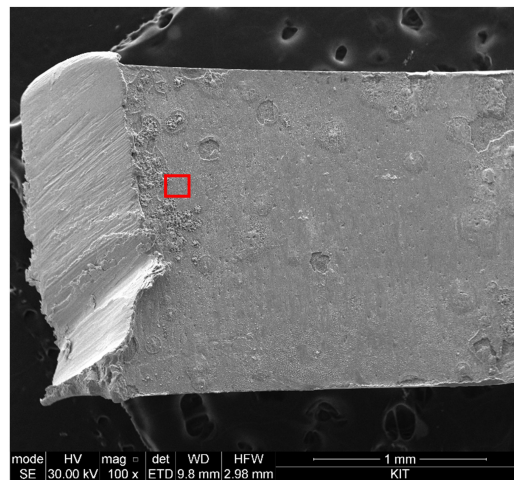
### 5.2.3 XPS surveys on the surface of the interaction layer between fuel and cladding

Figure 5.33 shows the recorded XPS survey spectrum for the Zircaloy cladding segment which has been previously in contact with the high burn-up  $\text{UO}_x$  fuel. As already seen by SEM-EDS measurements, elevated concentrations of chlorine and tellurium are found in the survey spectrum, which might have segregated from the pellet centre to periphery by transport along the temperature gradient of the fuel as described by McFarlane [MCFARLANE, 1996]. Their enrichment at the fuel-cladding interface could play a potential role for SCC in the long-term.



**Figure 5.33:** XPS spectrum of fuel layer on Zircaloy previously in contact with  $\text{UO}_x$  fuel cladding.

Additionally, an XPS survey spectrum for the cladding segment in contact with the MOX fuel was recorded. Figures 5.34 and 5.35 depict the analysed area upon the segment as well as the elemental spectrum. Noteworthy is the elevated amount of cadmium on the surface of the Zircaloy-4 cladding which could be excluded as a contamination from the hot cell as the specimens were treated in an ultrasonic bath prior to analysis. Fission-produced cadmium isotopes, as well as cadmium originating from impurities in fuel and cladding, display another important transgranular cracking / SCC agent affecting the integrity of fuel rod claddings as already described in the review article by Cox in the year 1990 [COX, 1990].



**Figure 5.34:** Examined surface area (indicated by red rectangle) analysed by XPS on Zircaloy segment previously in contact with MOX fuel.

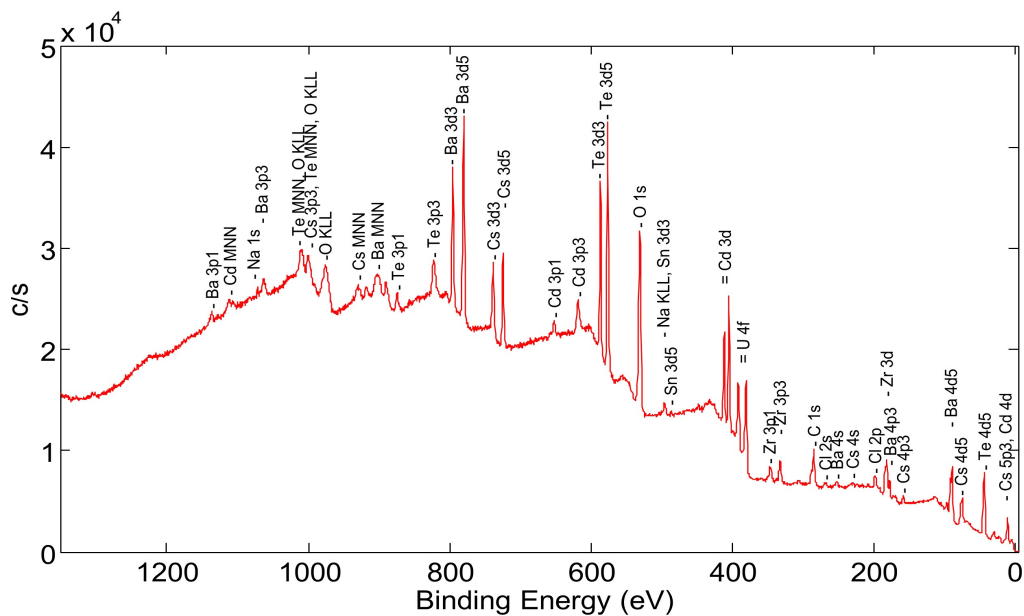


**Figure 5.35:** XPS survey spectrum of Zircaloy surface previously in contact with spent MOX fuel.

Furthermore, narrow scans for the Cl 2p elemental lines as depicted in figure 5.36 were performed for both fuel types. The Cl 2p<sub>3/2</sub> elemental line at 198.3 eV is similar to the reported binding energy of ZrCl<sub>4</sub> (198.3 eV), whilst the Cl 2p<sub>1/2</sub> elemental line at 199.9 eV

is close to the reference binding energy of  $ZrCl_2$  (199.8 eV) or  $CsCl$  (199.9 eV) [HWU *ET AL.*, 1986; KADANO *ET AL.*, 1994]. Zirconium chlorides are conceivable as residual impurities originating from the *Kroll-process* for manufacturing of Zircaloy alloys (see section 3.1).

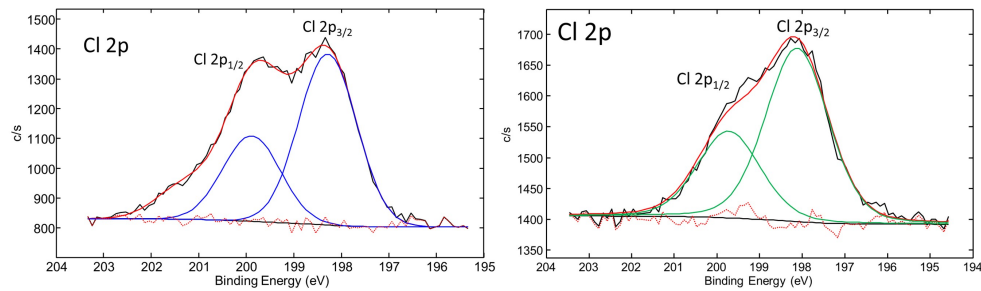


**Figure 5.36:** Narrow scans for the Cl 2p elemental lines for chlorine in the interaction layer upon the Zircaloy for the  $UO_x$  (left) and MOX (right) fuel.

For determination of the uranium redox state, further narrow scans were performed. Figure 5.36 shows the uranium 4f elemental lines determined by XPS for the Zircaloy specimen previously in contact with MOX fuel. As depicted, the redox state of uranium is 4+ with minor signals for U(VI) satellites, which could be the result of an oxidation of uranium during the sample preparation procedure. Next to the uranium 4f elemental lines, cadmium 3d elemental lines are observable likely in the form of metallic cadmium or as an oxide precipitate as stated by Kleykamp [KLEYKAMP, 1985].

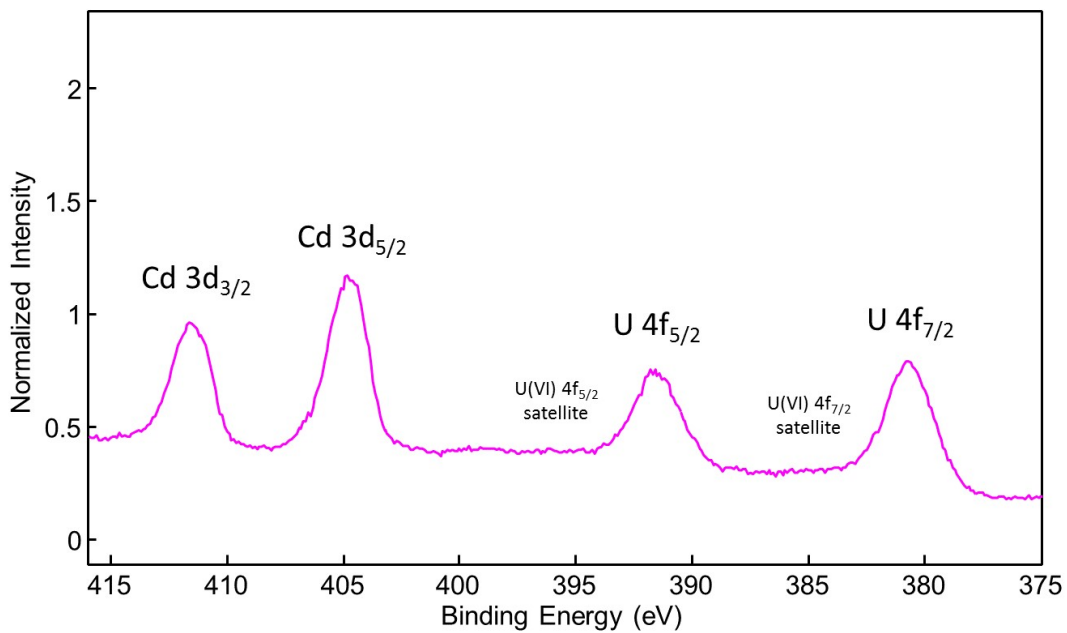


**Figure 5.37:** Narrow scans for the U 4f and Cd 3d elemental lines in the interaction layer upon the Zircaloy for the MOX fuel.

### 5.2.4 Conclusions on microscopic examinations on the fuel-cladding interface and their impact on possible cladding integrity degradation

Within this subsection of the present doctoral thesis, microscopic and spectroscopic investigations on the fuel-cladding interface were performed. Special focus was set on elements such as caesium, chlorine, iodine, tellurium or cadmium and their respective chemical compounds, which possibly could undergo chemical reactions with Zircaloy cladding. The three key elements affecting cladding integrity during reactor operation and beyond are identified as caesium, tellurium and iodine. In conjunction with the changing oxygen potential in the fuel affected by fission of initial uranium or plutonium and

gathering of oxygen by generated fission products as well as the initial O / M ratio itself, the right conditions for cladding attack via a pitting corrosion or SCC process might be met [HOLLECK AND KLEYKAMP, 1970; BALL *ET AL.*, 1989; VISWANATHAN, 2014].

Cadmium and tellurium deposits on the surface of the Zircaloy cladding were identified as shown e.g. in figure 5.35. Dannhäuser and colleagues described the influence of cadmium together with caesium on cladding degrading effects and stated that it is comparable to the SCC process of iodine [DANNHÄUSER *ET AL.*, 1984]. The role of the fission product tellurium on cladding attack mechanisms has already been discussed largely in the past literature, by e.g. Götzmann and colleagues, Pulham and Richards and more recently by Viswanathan [GÖTZMANN *ET AL.*, 1974; PULHAM AND RICHARDS, 1990; VISWANATHAN, 2014]. Since reactions between tellurium and the cladding material do not require a specific oxygen potential, and as proven by recent literature that tellurium occurs together with the  $\epsilon$ -particle phase agglomerated in the fuel, more research is needed on cladding degrading phenomena initiated by this fission product, as additional investigations were out of scope of this thesis [PELLEGRINI *ET AL.*, 2019; CLARK *ET AL.*, 2020].

For some postulated compounds agglomerated at the interface between fuel and cladding, e.g. CsI, the oxygen potential is not able to induce SCC afflicting the cladding integrity due to chemical stability of the compounds [CUBICCIOTTI AND DAVIES, 1976; CUBICCIOTTI AND SANECKI, 1978; KLEYKAMP, 1985]. Yet, regarding the contribution of radiolysis governed by the intense radiation field within the SNF, a dissociation of stable CsI is conceivable [SIDKY, 1998]. At this, an elevated iodine partial pressure would result from the radiolytical degradation of CsI and enable reactions of iodine with the proximal zirconia surface of the cladding tube. The role of chlorine impurities on cladding integrity is still unclear up to now. It is conceivable, regarding the corrosive behaviour of the halides on metallic surfaces, that chlorine contributes to cladding degradation in a similar manner as iodine, yet further experiments are needed to confirm this assumption.

### **5.3 Experimental simulation of cladding corrosion**

The effects of fission and activation product elements on Zircaloy-4 cladding were studied by a model experiment under conditions as they are expected to occur in the cladding tube located in a dry interim storage cask. Compounds such as CsI are expected to have an impact on the integrity and longevity of the cladding during the storage period, especially in case of its prolongation (see section 2.5). In the following subsections the interactions of caesium, iodine and chlorine bearing compounds as well as UO<sub>2</sub> pellets with the Zircaloy-4 cladding are investigated. The experimental layout is described in section 4.7.

#### **5.3.1 Optical examination of non-irradiated Zircaloy after termination of the corrosion experiment**

Figure 5.38 shows the change in superficial structure of a Zircaloy platelet in contact with UO<sub>2</sub> and fission / activation product analogues before and after the heat treatment from 400 °C to ambient temperature. Clearly visible is an evolved reaction zone at the Zircaloy surface, resulting in a black precipitate and a roughening of the previously polished surface for all experiments. Similarly, black precipitates on surfaces of irradiated Zircaloy claddings, composed of uranium, caesium and other fission products, had been described by various authors for post-irradiation examinations of SNF e.g. Götzmann, Viswanathan or Herm [GÖTZMANN, 1979; VISWANATHAN, 2014; HERM, 2015].

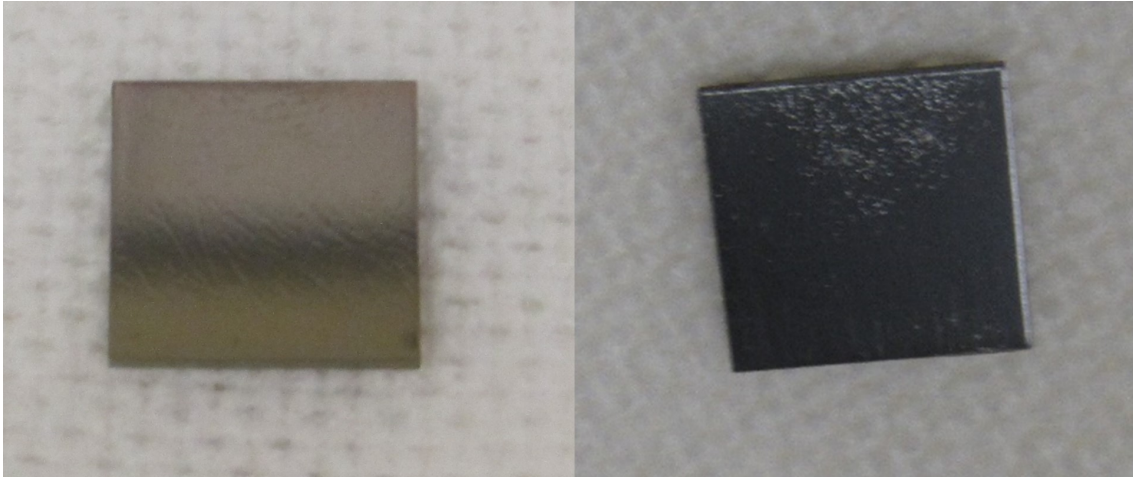


**Figure 5.38:** Comparison by optical examination of non-irradiated Zircaloy platelets before (left) and after termination (right) of the corrosion experiment.

In figure 5.39, an optical examination by video microscope is shown, displaying the reacted surfaces of all Zircaloy-4 specimens used in the experiment in more detail. Clearly visible is the slightly damaged and blackened zirconia surface, indicating reactions between the added  $\text{UO}_2$  and the Zircaloy surface in all samples including the blank experiment.

$\text{ZrO}_2$  covering the Zircaloy surface represents a thermodynamically stable oxide and serves as an additional protective layer of the underlying monoclinic and tetragonal  $\alpha$ - /  $\beta$ - $\text{Zr(O)}$  and Zircaloy layers as described by Bohe and colleagues [BOHE *ET AL.*, 1996]. However, if an initial pitting or the evolution of micro cracks evolve, by e.g. an iodine induced stress corrosion cracking mechanism, the zirconium layers underneath can be attacked rapidly by halogen bearing species, resulting in a corrosion of the zirconium alloy and thus a degradation of the cladding [HOFMANN AND SPINO, 1985; SIDKY, 1998].

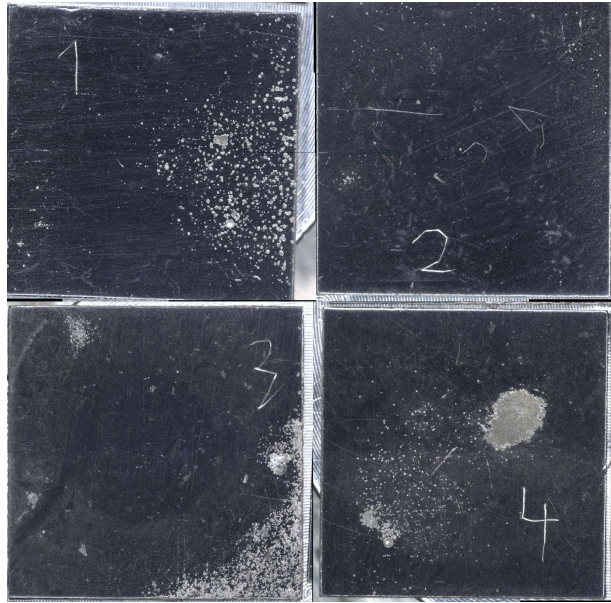


**Figure 5.39:** Optical examination of the utilised non-irradiated Zircaloy platelets after the corrosion experiment.

The temperature range within this experiment was not high enough to ensure a complete volatilisation of the utilised caesium halide salts, hence it is conceivable, that the  $\text{UO}_2$  oxidised the Zircaloy surface and the caesium halides reacted with the oxygen-depleted  $\text{UO}_2$ . For further determination of the corrosion process, analyses with XPS and SEM-EDS were conducted as described in the following subsections 5.3.2 – 5.3.3.



## Results and Discussion

Furthermore, for all Zircaloy platelets in contact with the respective caesium halide salt as well as the  $\text{UO}_2$  pellets, minor amounts of uranium were observable on the surface structure. Remarkably, the uranium compound identified on the surface was in a +VI oxidation state, which might be the result of either trace amounts of oxygen in the applied Ar-atmosphere or an oxidation of uranium due to the washing procedure applied after termination of the experiment, as well as the preparation of the specimens for analysis under oxidic conditions. XPS narrow scans for U 4f orbitals are shown in figure 5.41.

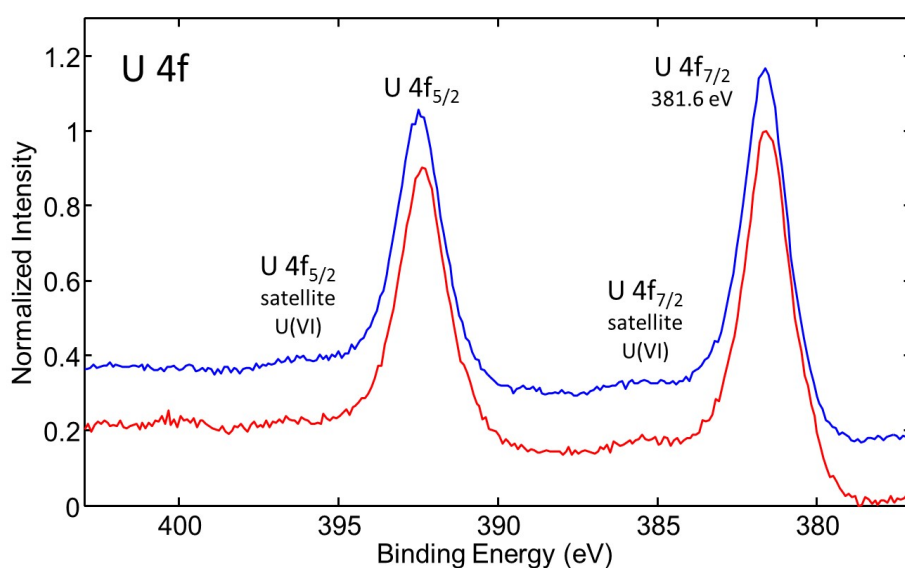


**Figure 5.41:** Narrow scans of uranium 4f orbitals in order to determine the uranium oxidation state in the Zircaloy specimens. The blue line shows the Zircaloy platelet previously in contact with  $\text{UO}_2$  and  $\text{CsI}$ , whereas the specimen in contact with  $\text{UO}_2$  and  $\text{CsCl}$  is depicted by the red line.

Figure 5.42 shows narrow scans performed for iodine 3d lines for the samples with two signals observable at 619.5 eV and 621.0 eV. The peaks show similarity to the reported binding energies of a  $\text{ZrI}_{4-x}$  species as given in the literature by Kaufmann [KAUFMANN, 1988].

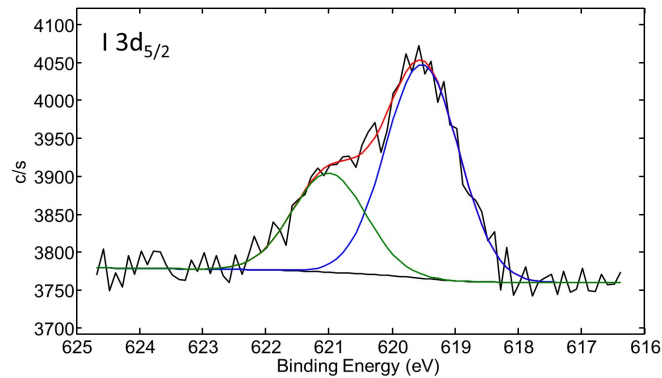


**Figure 5.42:** Iodine 3d narrow scans. The black line represents the spectrum for the Zircaloy specimen, whereas the blue line depicts the iodine bonding state in zirconium iodide compounds and the green line the bonding state for elemental iodine.

In addition to the overall XPS survey, an analysis of chlorine and iodine rich particles upon the surface was performed. Figure 5.43 depicts the recorded spectra and chemical composition of the particles. Similar to the irradiated Zircaloy specimen described in chapter 5.2, halogen rich hot spots were detected upon the surface. These chlorine, iodine and caesium bearing agglomerates could either be residual Cs halide particles still adherent to the surface after treatment in an ultrasonic bath or display a reactive attack front for pitting corrosion on the inner side of the cladding [SIDKY, 1998; PARK *ET AL.*, 2007].



### 5.3.3 SEM-EDS analysis of the non-irradiated Zircaloy after termination of the corrosion experiment

Figure 5.44 shows the SEM picture in secondary electron mode and EDS analysis of the blank specimen, only in contact with the UO<sub>2</sub> pellet. The analysed data indicates an oxidation of the prior polished Zircaloy surface<sup>32</sup> to ZrO<sub>2</sub>, as depicted by the etched surface structure with an atomic Zr : O ratio of  $2.00 \pm 0.3$ .

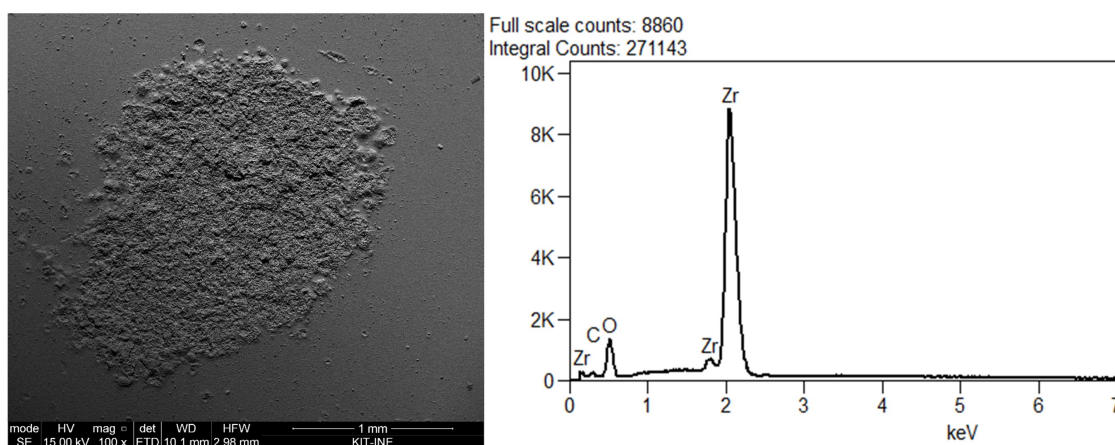


**Figure 5.44:** SEM picture taken in secondary electron mode and EDS analysis of the blank specimen.

On all Zircaloy specimens, regions with deposited uranium dioxide could be identified, not removable by prior cleaning the samples in an ultrasonic bath, similar to the irradiated UO<sub>x</sub> and MOX specimens described in section 5.2.2. Figure 5.45 shows a uranium rich deposits on the zirconia surface exemplarily for the specimen in contact with CsI and UO<sub>2</sub>

<sup>32</sup> An oxidation of the polished surface in the relatively short time period between polishing and transfer of the Zircaloy to the reaction vessels cannot be excluded.

in backscatter electron mode, where heavier elements are displayed in a brighter shade. This adhesive bonding between  $ZrO_2$  and  $UO_2$  was already described by Ciszak and co-workers for irradiated PWR specimens [CISZAK *ET AL.*, 2019].

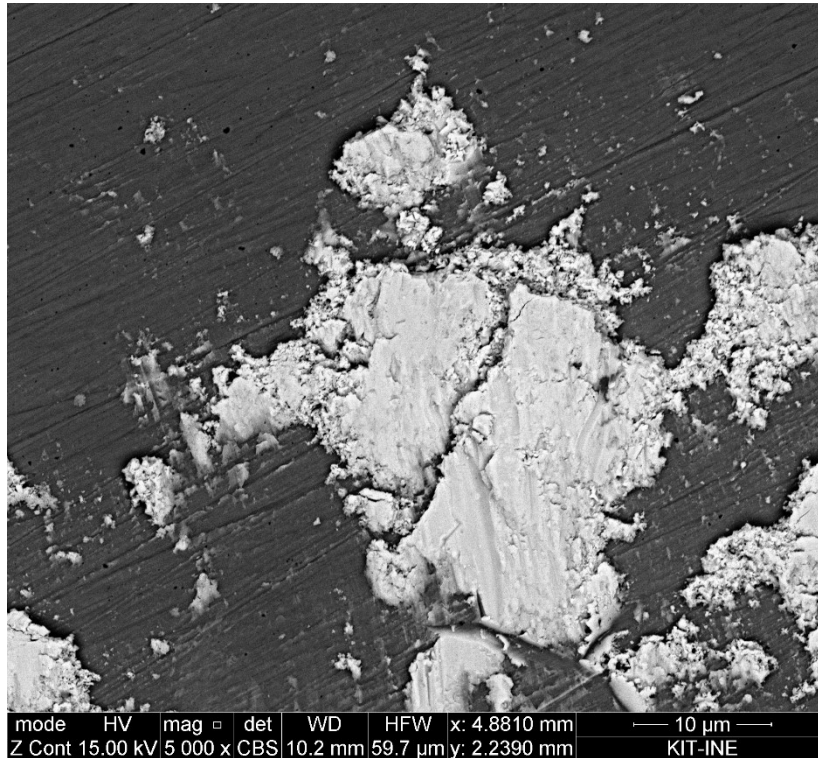


**Figure 5.45:**  $UO_2$  deposits on the zirconia surface observable in all specimens. The SEM picture was taken in backscatter electron mode, where heavier elements are depicted brighter shade.

For the specimen, previously in contact with caesium chloride and the  $UO_2$  pellet, regions on the zirconia surface structure could be identified, indicating pitting corrosion, as shown in figure 5.46. EDS analysis of the damaged surface revealed elevated amounts of chlorine and caesium on the altered bulk structure, leading to the assumption, that either a halogen induced corrosion process or a damaging effect by the  $UO_2$  pellet took place.

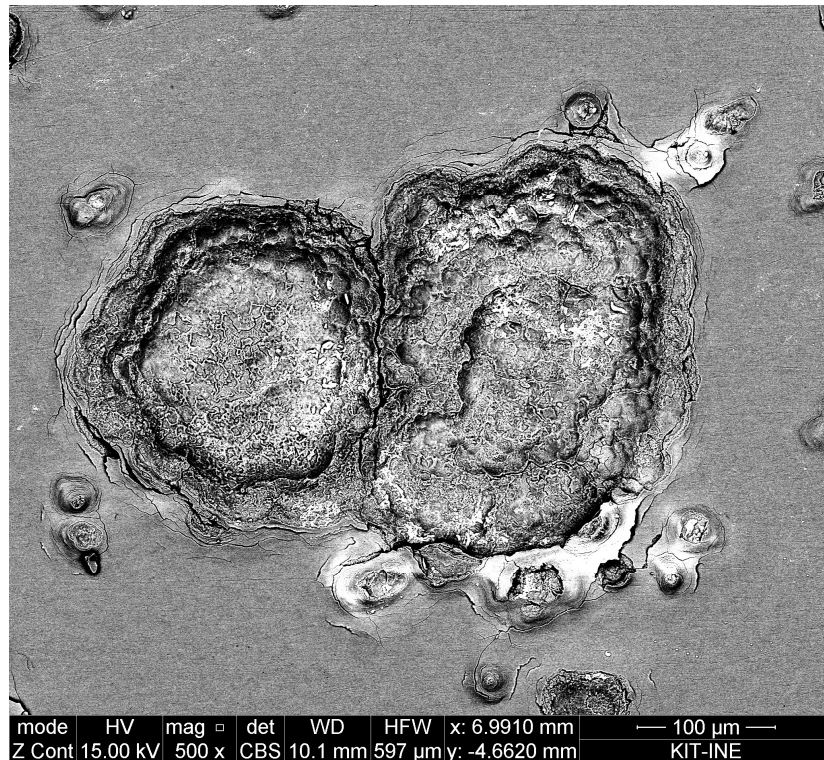


**Figure 5.46:** SEM picture taken in backscatter electron mode of the area on the Zircaloy specimen in contact with CsCl and UO<sub>2</sub>, indicating a pitting corrosion process on the zirconia layer.

Moreover, on the specimen in contact with CsI, crystals could be identified composed of iodine and uranium but without detectable caesium as shown by the SEM-EDS analysis in figure 5.47, which was also described by Cubicciotti and Sanecki, and summarised by Sidky for irradiated LWR cladding specimens [CUBICCIOTTI AND SANECKI, 1978; SIDKY, 1998]. It is assumed, that the residual copper shown in the EDS analysis is an impurity resulting from the copper gasket utilised in the experiment to ensure tightness of the sample vessel.

The deposited iodine bearing crystals were not removable by prior treatment of the sample in an ultrasonic bath, hence it is conceivable that they bonded in a similar way as the uranium inclusions described earlier in this section. Yet, a precise statement on the mechanism of the iodine reaction with uranium compounds and the chlorine interaction

## Results and Discussion

with Zircaloy at much lower temperatures as prevailing under reactor operation conditions is not feasible solely with the analysed data and further studies are required.

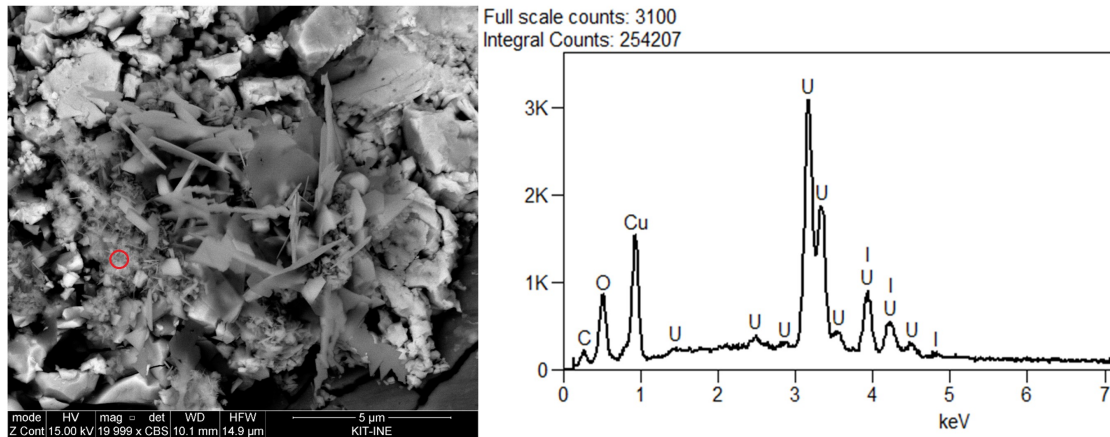


**Figure 5.47:** Crystals on the surface layer rich in iodine and uranium of the specimen previously in contact with CsI and UO<sub>2</sub>. The point of EDS analysis is indicated by the red circle.

As described by Shimada and co-workers, Hofmann and Spino, as well as Sidky, the reactive compound within the fuel-cladding interaction layer responsible for a stress corrosion cracking mechanism is most likely gaseous ZrI<sub>4</sub> at  $T > 400$  °C formed by the thermal and, more governing, radiolytically dissociation of deposited CsI during reactor operation [SHIMADA *ET AL.*, 1983; HOFMANN AND SPINO, 1985; SIDKY, 1998]. Due to the absence of a strong radiation field in this experiment, as it is present during reactor operation as well as during interim storage of the SNF, a clear assumption on the corrosive behaviour of the iodine compound cannot be shown by this type of experiment. For further understanding on the processes occurring on the inner side of the cladding, it is evident, that experiments with irradiated materials are necessary in order to acquire a profound knowledge on the corrosion mechanism.

### 5.3.4 Conclusions from the experimental simulation of cladding corrosion

This subsection of the present Ph.D. thesis dealt with potential reactions of SNF components with Zircaloy investigated in a simulation experiment at temperatures  $\leq 400$  °C. The aims of the performed experiment were to gain insights into cladding degrading processes. The results obtained by this experiment show that even under temperatures much lower than under reactor operation conditions the inner side of the cladding can undergo chemical reactions with Cs-halides inducing pitting corrosion.

Several individual factors and effects are responsible for the degradation of cladding integrity of SNF tubing during interim storage (see sections 2.3 – 2.6). The bonding of the uranium dioxide within the cladding tube as an effect of a gap closure during reactor service had already been described by Ciszak and colleagues [CISZAK *ET AL.*, 2019]. In accordance with their results, all specimens of the experiment simulating dry interim storage conditions show uranium agglomerates, which were present on the cladding surfaces and not removable with ultrasonic treatment. The possible formation of uranates in the peripheral, cladding adherent region would indicate, that caesium is partly bound, which would enable a higher iodine potential within the system, thus leading to an elevated amount of iodine for reaction with the cladding material according to Hofmann and Spino [HOFMANN AND SPINO, 1985]. Yet, an oxidation of uranium within the system is rather unlikely and, as shown by SEM-EDS analysis in the present work, no caesium uranate compound could be identified within the experiment.

Furthermore, a pitting corrosion effect was observed in specimen treated with CsCl next to the UO<sub>2</sub> pellet, indicating that the halide bearing compound reacted with the zirconia surface layer. In general, all free halogens show corrosive features for most metal alloy surfaces, yet to liberate chlorine as a gas from relatively stable CsCl the temperature range within the experiment was not sufficiently high, leading to the assumption, that due to the

uranium dioxide next to the CsCl and zirconium alloy, a reaction was enabled similar to iodine induced phenomena [GÖTZMANN, 1982A].

In case of the iodine bearing caesium salts, a formation of a crystal compound upon the zirconia surface was observed during SEM-EDS measurements composed of uranium and iodine. By XPS analysis of the iodine bearing compound it would be conceivable, that next to the residual bonded uranium described earlier, the iodine could be deposited as a  $ZrI_{4-x}$  species on the surface layer, not removable by ultrasonic washing [KAUFMANN, 1988].

In conclusion, degradation of cladding integrity during interim storage is a complex phenomenon comprised of many individual factors, e.g. hydrogen content and orientation within the cladding after in-reactor service, fission product chemistry on the inner surface, the hardening of the cladding due to radiation as well as the governing radiation field itself, to name a few effects. It is expected, that the interaction of all physical and chemical phenomena is the key role in the degradation process, whereas for single effects, a singular corrosion mechanism is difficult to postulate. Furthermore, another challenging task, is the distinction between cladding degrading phenomena, already occurring during in-reactor service contrary to effects solely taking place during interim storage.

## 6 Summary and conclusions

Within this Ph.D. thesis, analytical and experimental studies as well as calculations were performed in order to obtain further understanding on the occurrence of critical radionuclides in irradiated claddings, spent  $\text{UO}_x$  and spent MOX fuel, which are of relevance for the safety of a SNF repository, as well as cladding degrading chemical phenomena, which might occur during the long-term storage of used nuclear fuel. The outcomes of this work provide significant scientific results for the deeper understanding of this complex waste form and the chemical as well as thermodynamic processes occurring in it, with particular focus on relevant RNs for SNF source terms, such as Cl-36 and I-129. Furthermore, special regard was set to agglomerates found in the interaction layer between the SNF and cladding tube and their possible impact on the cladding integrity during the interim storage of nuclear fuel.

I-129 generated by nuclear fission, as well as the activation product Cl-36 are both relevant isotopes for safety assessments in the context of deep geological disposal of SNF, due to their presumably anionic occurrence within the waste form and thus high mobility within the individual constituents of a repository system. Therefore, a precise and profound analysis on the inventories of these critical radioisotopes within used nuclear fuel next to other isotopes is indispensable. In the course of this work, a radiochemical separation method was developed, providing a reliable and accurate determination of Cl-36 and I-129 present in highly radioactive waste specimens, e.g. irradiated  $\text{UO}_x$  and

## Summary and conclusions

---

MOX fuel, as well as their respective Zircaloy-4 cladding material by use of liquid-liquid extraction and precipitation methodologies.

The distribution of iodine in a nuclear fuel pellet is afflicted with uncertainties, as present calculation codes only rely on nuclear data, e.g. burn-up, neutron flux or linear power rate. Within the present thesis, it was proven, that a temperature driven transport process for iodine from the hot centre of the pellet to the colder cladding adjacent parts is taking place, resulting in an enrichment of iodine at the peripheral location in the SNF pellet. Furthermore, information on the proportion of the Cl-35 impurity in LWR fuel components, as well as the generated amount of Cl-36 during irradiation was derived. At this, the developed separation method offers a reliable and highly selective technique, proven by the obtained recovery yields, for the quantification of both, Cl-36 and I-129, in the examined, highly radioactive specimens, regardless of their complex matrices, excess of other RNs or high dose rate.

Furthermore, determinations of the actinide, fission and activation product inventories of selected isotopes were performed in order to prove the reliability and accuracy of the experimental and analytical techniques applied within this study. Experimental results were compared to values obtained by MCNP / CINDER and webKORIGEN calculations, which are with the exception of a few isotopes (e.g. U-235 and Co-60), in good agreement to each other within the analytical uncertainty. In addition, the inventories of spent high burn-up  $UO_x$  and MOX fuel were compared to each other in order to establish reliable data on the difference between both fuel types needed for future repository safety investigations. The obtained results contribute to improving the knowledge of the inventory of SNF and the distribution of RNs therein, as especially for isotopes with long half-live and high mobility within a repository system such as I-129 and Cl-36, the existing data on their generated amount during reactor operation and latter release and retention behaviour is scarce.

Furthermore, this Ph.D. thesis gives details on the distribution of elements within the interaction layer between SNF and cladding of irradiated LWR  $UO_x$  and MOX fuel. At this, the focus was set on phenomena of possible chemically influenced, cladding

degrading processes by deposited elements segregated during reactor operation from the pellet to the inner surface of the cladding tube, as well as on potential differences regarding the fuel type and irradiation history, e.g. burn-up or linear power rate. The findings obtained in the present thesis during the analysis of SNF and cladding specimens reveal the existence of mixed phases at the fuel-cladding interface, which could tentatively contribute to the weakening of the cladding. It is most likely, that these mixed phases, consisting of fission-produced iodine, caesium and tellurium as well as the impurity within fuel and cladding, chlorine, formed during reactor operation. It is, however, unclear whether such reactions with the Zircaloy cladding, accompanied by the formation of mixed U-Zr-O-Cl-I phases, continue during interim storage conditions. For the first time to the knowledge of the author, synchrotron radiation based techniques were applied in order to study the occurrence of chlorine and iodine by means of K-edge XANES analysis on actual SNF (UO<sub>x</sub> and MOX) and Zircaloy cladding specimens. From the data obtained, iodine is presumably present in form of CsI. For chlorine, it is evident, that in order to derive information on its oxidation state, further research is needed, regarding the chemical form and behaviour within the fuel-cladding system. The obtained XANES spectra within the present work are, to some extent, noisy and interferences, based on the SNF matrices, cannot be excluded. Nevertheless, from the results obtained within this part of the present work, it is shown that the actual situation within the fuel-cladding interface is much more complicated, than assumed in thermodynamic calculations.

In addition to actual SNF cladding specimens, this Ph.D. thesis addressed the behaviour of fission and activation product compounds within the fuel-cladding system by means of a simulated model experiment. From the results of the experiment it was evident, that halogens, i.e. chlorine and iodine, react with the Zircaloy cladding material and UO<sub>2</sub> in a temperature range < 400 °C, as it is expected under interim storage conditions, and during a relatively short time period. The identified phases, formed upon the cladding material are similar to agglomerates found on actual, irradiated specimens. Furthermore, zirconium iodide species were found in addition to iodine species associated to uranium dioxide.

## Summary and conclusions

---

Results obtained by this experiment indicate, that iodine has a relatively high reactivity, even at the low temperatures within the experiment, and thus has the potential to induce a pitting corrosion process. However, the integrity of used fuel claddings is depending on various factors, which are all, to some extent, intertwined with each other regarding possible degradation processes of the Zircaloy tubes. The results of the experiments performed within this work are contributing to the deeper understanding of the chemical processes, still proceeding within the fuel-cladding system in a transport and storage cask, after in-reactor service. Nevertheless, the experimental conditions are not fully reflecting the real situation under interim storage conditions, therefore highlighting the necessity of further research on this topic.

# Appendix

## Appendix A

**Table A.1:** Experimentally determined activation product inventory for all samples.

RN	UO <sub>x</sub> -RIM [Bq/t <sub>HM</sub> ]	UO <sub>x</sub> -CORE [Bq/t <sub>HM</sub> ]	MOX-RIM [Bq/t <sub>HM</sub> ]	MOX-CORE [Bq/t <sub>HM</sub> ]	Zry-UO <sub>x</sub> [Bq/t <sub>HM</sub> ]	Zry-MOX [Bq/t <sub>HM</sub> ]
Cl-36	6.0(±0.9)E+08	3.6(±0.5)E+08	4.5(±0.7)E+08	5.8(±0.9)E+08	6.3(±0.3)E+08	5.3(±0.2)E+08
Co-60	bdl	bdl	bdl	bdl	5.4(±0.5)E+10	2.7(±0.3)E+10
Sb-125	bdl	bdl	bdl	bdl	5.3(±0.5)E+10	5.3(±0.5)E+10

bdl: below detection limit

**Table A.2:** Experimentally determined fission product inventory for all samples.

RN	UO <sub>x</sub> -RIM [Bq/t <sub>HM</sub> ]	UO <sub>x</sub> -CORE [Bq/t <sub>HM</sub> ]	MOX-RIM [Bq/t <sub>HM</sub> ]	MOX-CORE [Bq/t <sub>HM</sub> ]	Zry-UO <sub>x</sub> [Bq/t <sub>HM</sub> ]	Zry-MOX [Bq/t <sub>HM</sub> ]
Sr-90	2.3(±0.2)E+15	nd	nd	nd	1.4(±0.2)E+13	nd
I-129	2.4(±0.3)E+09	nd	2.2(±0.4)E+09	nd	bdl	bdl
Cs-137	3.3(±0.3)E+15	2.6(±0.3)E+15	2.3(±0.2)E+15	2.2(±0.2)E+15	9.6(±0.5)E+12	1.0(±0.3)E+14
Eu-154	3.3(±0.3)E+13	3.6(±0.4)E+13	3.4(±0.3)E+13	4.8(±0.5)E+13	1.1(±0.1)E+10	1.6(±0.2)E+11
Eu-155	3.8(±0.4)E+12	4.1(±0.4)E+12	3.0(±0.3)E+12	4.1(±0.4)E+12	bdl	1.8(±0.2)E+10

bdl: below detection limit; nd: not determined

**Table A.3:** Experimentally determined actinide inventory for all samples.

	<b>UO<sub>x</sub>-RIM</b>	<b>UO<sub>x</sub>-CORE</b>	<b>MOX-RIM</b>	<b>MOX-CORE</b>	<b>Zry-UO<sub>x</sub></b>	<b>Zry-MOX</b>
<b>actinide</b>	<b>[Bq/thm]</b>	<b>[Bq/thm]</b>	<b>[Bq/thm]</b>	<b>[Bq/thm]</b>	<b>[Bq/thm]</b>	<b>[Bq/thm]</b>
<b>U-234</b>	6.2(±0.6)E+10	5.6(±0.6)E+10	5.8(±0.6)E+10	5.0(±0.5)E+10	bdl	bdl
<b>U-235</b>	3.9(±0.4)E+08	3.5(±0.4)E+08	2.4(±0.2)E+08	2.3(±0.2)E+08	1.9(±0.2)E+05	3.2(±0.3)E+05
<b>U-236</b>	1.5(±0.2)E+10	1.4(±0.1)E+10	2.2(±0.2)E+09	2.0(±0.2)E+09	6.0(±1.4)E+06	4.0(±0.9)E+06
<b>U-238</b>	1.2(±0.1)E+10	1.2(±0.1)E+10	1.1(±0.1)E+10	1.1(±0.1)E+10	5.0(±0.5)E+06	1.6(±0.1)E+07
<b>Np-237</b>	2.5(±0.3)E+10	2.4(±0.2)E+10	1.3(±0.1)E+10	1.1(±0.1)E+10	1.3(±0.2)E+07	2.5(±0.3)E+07
<b>Pu-239</b>	1.4(±0.1)E+13	1.3(±0.1)E+13	2.9(±0.3)E+13	2.8(±0.3)E+13	2.6(±0.3)E+10	1.2(±0.1)E+11
<b>Pu-240</b>	2.8(±0.3)E+13	2.6(±0.3)E+13	1.3(±0.1)E+14	1.3(±0.1)E+14	6.4(±1.0)E+10	1.6(±0.2)E+11
<b>Pu-241</b>	5.7(±0.6)E+13	1.1(±0.5)E+13	1.7(±0.2)E+14	4.7(±1.4)E+13	1.1(±0.1)E+11	4.4(±0.5)E+11
<b>Pu-242</b>	1.8(±0.2)E+11	1.7(±0.2)E+11	5.4(±0.5)E+11	4.7(±0.5)E+11	4.4(±0.9)E+08	1.5(±0.2)E+09
<b>Am-241</b>	2.6(±0.3)E+14	2.3(±0.2)E+14	1.2(±0.1)E+15	8.1(±0.8)E+14	1.8(±0.1)E+11	1.7(±0.2)E+12
<b>Am-243</b>	2.5(±0.3)E+12	2.5(±0.3)E+12	7.6(±0.8)E+12	6.8(±0.7)E+12	2.5(±1.3)E+09	1.8(±0.6)E+10
<b>Am-244</b>	1.6(±0.2)E+14	1.5(±0.2)E+14	5.0(±0.5)E+14	4.3(±0.4)E+14	1.9(±0.1)E+13	1.0(±0.1)E+12
<b>Am-245</b>	8.7(±0.9)E+10	8.4(±0.9)E+10	4.5(±0.5)E+11	3.9(±0.4)E+11	bdl	bdl
<b>Am-246</b>	2.7(±0.3)E+10	2.9(±0.8)E+10	8.3(±0.9)E+10	7.1(±1.3)E+10	bdl	bdl

bdl: below detection limit

**Table A.4:** Experimentally determined total inventory of selected fission products for both fuel types assuming 100  $\mu\text{m}$  of RIM area.

<b>RN</b>	<b>UO<sub>x</sub> [Bq/t<sub>HM</sub>]</b>	<b>MOX [Bq/t<sub>HM</sub>]</b>
<b>Cs-137</b>	2.6( $\pm$ 0.3)E+15	2.2( $\pm$ 0.2)E+15
<b>Eu-154</b>	3.6( $\pm$ 0.4)E+13	4.8( $\pm$ 0.5)E+13
<b>Eu-155</b>	4.1( $\pm$ 0.4)E+12	4.1( $\pm$ 0.4)E+12

**Table A.5:** Experimentally determined total inventory of selected actinides for both fuel types assuming 100  $\mu\text{m}$  of RIM area.

<b>RN</b>	<b>UO<sub>x</sub> [Bq/t<sub>HM</sub>]</b>	<b>MOX [Bq/t<sub>HM</sub>]</b>
<b>U-234</b>	5.6( $\pm$ 0.6)E+10	5.0( $\pm$ 0.5)E+10
<b>U-235</b>	3.5( $\pm$ 0.4)E+08	2.3( $\pm$ 0.2)E+08
<b>U-236</b>	1.4( $\pm$ 0.1)E+10	2.0( $\pm$ 0.2)E+09
<b>U-238</b>	1.2( $\pm$ 0.1)E+10	1.1( $\pm$ 0.1)E+10
<b>Np-237</b>	2.4( $\pm$ 0.2)E+10	1.1( $\pm$ 0.1)E+10
<b>Pu-239</b>	1.3( $\pm$ 0.1)E+13	2.8( $\pm$ 0.3)E+13
<b>Pu-240</b>	2.6( $\pm$ 0.3)E+13	1.3( $\pm$ 0.1)E+14
<b>Pu-241</b>	1.2( $\pm$ 0.5)E+13	4.8( $\pm$ 1.4)E+13
<b>Pu-242</b>	1.7( $\pm$ 0.2)E+11	4.7( $\pm$ 0.5)E+11
<b>Am-241</b>	2.3( $\pm$ 0.2)E+14	8.1( $\pm$ 0.8)E+14
<b>Am-243</b>	2.5( $\pm$ 0.3)E+12	6.8( $\pm$ 0.7)E+12
<b>Cm-244</b>	1.5( $\pm$ 0.2)E+14	4.3( $\pm$ 0.4)E+14
<b>Cm-245</b>	8.4( $\pm$ 0.9)E+10	3.9( $\pm$ 0.4)E+11
<b>Cm-246</b>	2.9( $\pm$ 0.8)E+10	7.1( $\pm$ 1.3)E+10

## Appendix

**Table A.6:** Calculated actinide inventory of various regions within the UO<sub>x</sub> fuel pellet as well as values obtained for KORIGEN calculations of the MOX fuel.

RN	MCNP-CORE [Bq/tHM]	MCNP-RIM [Bq/tHM]	MCNP-CLAD [Bq/tHM]	KORIGEN-MOX [Bq/tHM]
U-234	5.8E+10	5.5E+10	8.7E+04	1.1E+11
U-235	4.5E+08	3.3E+08	1.2E+02	1.9E+06
U-236	1.2E+10	1.1E+10	7.9E+03	1.7E+08
U-238	1.2E+10	9.6E+09	3.3E+04	1.1E+10
Np-237	2.0E+10	2.0E+10	4.0E+04	9.9E+09
Pu-239	1.5E+13	3.2E+13	2.3E+08	3.5E+13
Pu-240	2.0E+13	3.6E+13	2.4E+08	1.2E+14
Pu-241	2.1E+15	3.6E+15	2.9E+10	6.6E+15
Pu-242	1.5E+11	3.7E+11	4.7E+06	8.3E+11
Am-241	1.8E+14	4.2E+14	3.4E+09	8.9E+14
Am-243	1.8E+12	4.8E+12	7.4E+07	1.2E+13
Cm-244	1.5E+14	3.9E+14	7.5E+09	7.8E+14
Cm-245	6.2E+10	1.7E+11	3.0E+06	2.0E+11
Cm-246	1.5E+10	4.4E+10	1.2E+06	6.1E+11

**Table A.7:** Calculated fission product inventory of various regions within the UO<sub>x</sub> fuel as well as values obtained for KORIGEN calculations of the MOX fuel.

RN	MCNP-CORE [Bq/tHM]	MCNP-RIM [Bq/tHM]	MCNP-CLAD [Bq/tHM]	KORIGEN-MOX [Bq/tHM]
Sr-90	1.7E+15	2.0E+15	2.2E+10	5.5E+14
I-129	1.6E+09	2.7E+09	2.6E+04	1.6E+09
Cs-137	2.8E+15	4.2E+15	3.5E+10	1.8E+15
Eu-154	3.5E+13	5.7E+13	5.2E+08	3.2E+13
Eu-155	1.9E+12	3.3E+12	3.2E+07	1.6E+12

## Appendix B

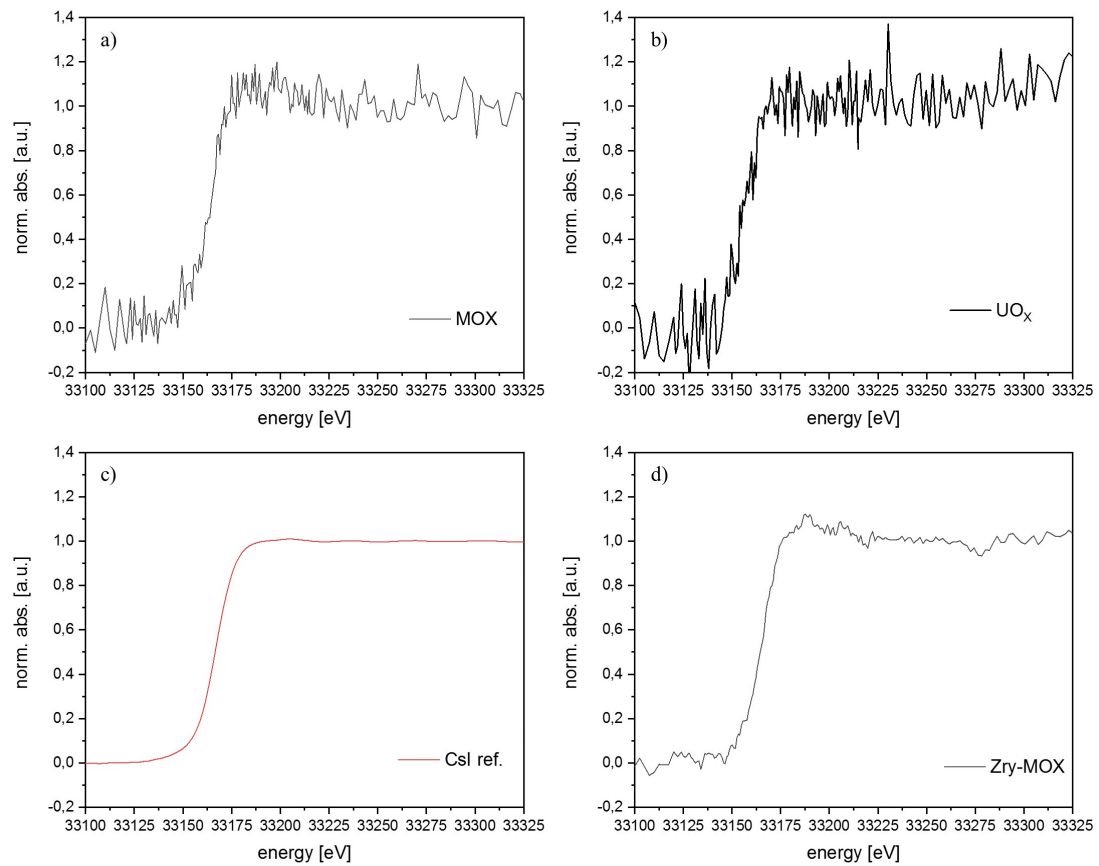


**Figure B.1:** I K-edge XANES spectra of the examined specimens. a) and b) show the I K-edge XANES spectra of the two different SNF fragments previously in contact with the cladding. Spectrum c) shows the CsI reference material and spectrum d) the Zircaloy specimen segmented from the spent MOX fuel.

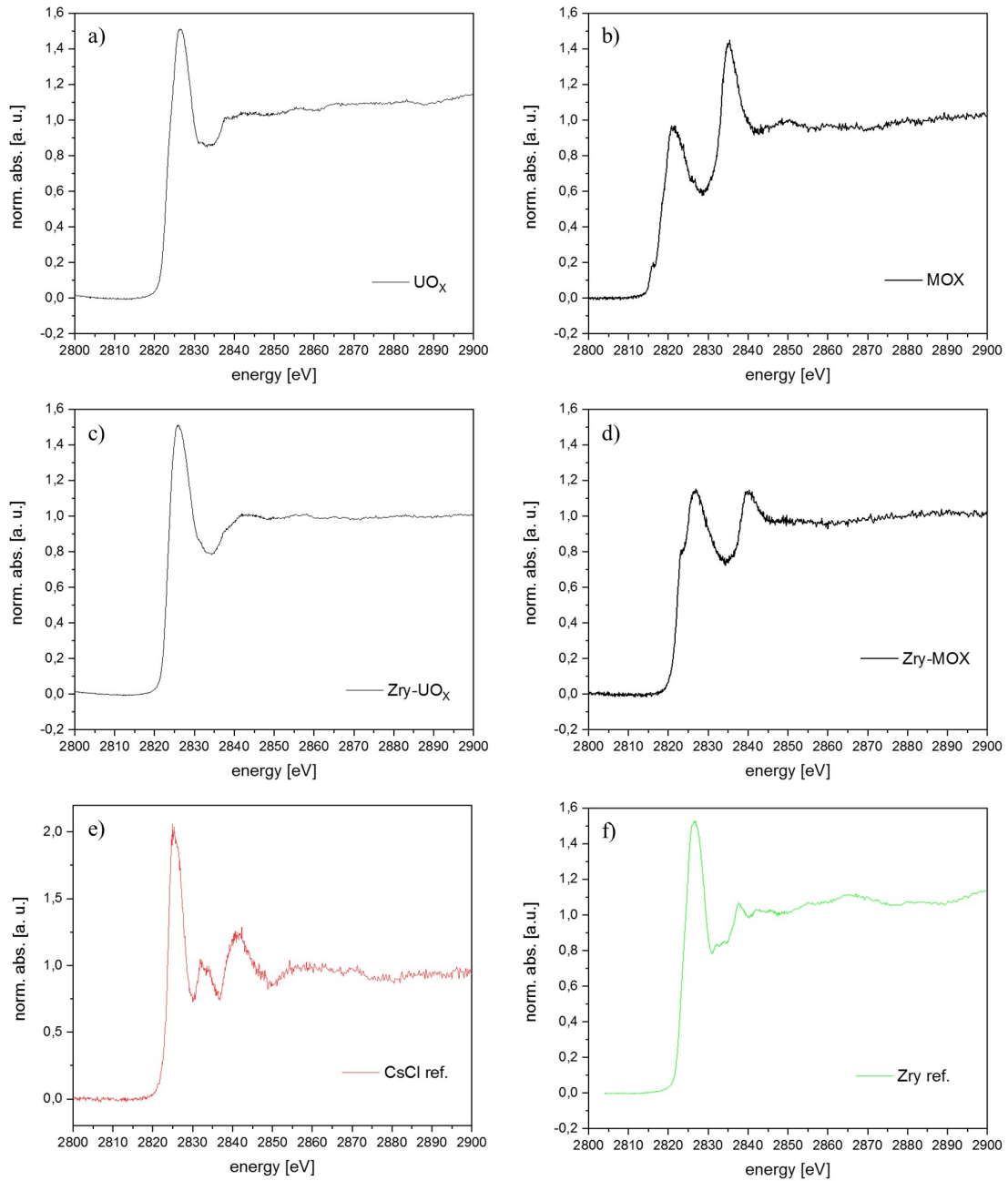


**Figure B.2:** Recorded Cl K-edge XANES spectra. Spectra a) and b) depict the examined fuel fragments previously in contact with their respective cladding. The appertaining cladding specimen XANES spectra are shown in c) and d). Spectrum e) shows the measured CsCl reference material and spectrum f) the reactor grade, non-irradiated cladding.

Appendix C

**Table C.1:** Atomic composition and uncertainties in atom % of phase 1 (red) of the alkaline defueled high burn-up UO<sub>x</sub> fuel Zircaloy specimen.

Element	C	O	Al	Fe	Zr	Sn
atom %	28.8±0.9	46.8±1.3	0.3±0.0	0.1±0.0	23.6.3±0.6	0.3±0.0

**Table C.2:** Atomic composition and uncertainties in atom % of phase 2 (yellow) of the alkaline defueled high burn-up UO<sub>x</sub> fuel Zircaloy specimen.

Element	C	O	Si	Zr	Cs	Ba	Nd	U
atom %	25.9±0.8	55.0±1.4	0.2±0.1	15.3±0.7	0.2±0.1	0.3±0.1	0.2±0.0	2.9±0.3

**Table C.3:** Atomic composition and uncertainties in atom % of phase 3 (blue) of the alkaline defueled high burn-up UO<sub>x</sub> fuel Zircaloy specimen.

Element	C	O	Al	Zr
atom %	17.8±1.1	25.8±1.2	1.1±0.0	55.2±1.5

**Table C.4:** Atomic composition and uncertainties in atom % of phase 4 (green) of the alkaline defueled high burn-up UO<sub>x</sub> fuel Zircaloy specimen.

Element	C	O	Al	Zr	Nd	U
atom %	24.3±1.0	30.6±1.6	2.2±0.2	29.2±1.5	0.3±0.1	13.4±1.0

## References

AIMOZ, L., TAVIOT-GUÉHO, C., CHURAKOV, S. V., CHUKALINA, M., DÄHN, R., CURTI, E., BORDET, P. AND VESPA, M. (2012) ‘Anion and cation order in iodide-bearing Mg/Zn-Al layered double hydroxides’, *Journal of Physical Chemistry C*, 116, pp. 5460–5475.

AIMOZ, L., WIELAND, E., TAVIOT-GUÉHO, C., DÄHN, R., VESPA, M. AND CHURAKOV, S. V. (2012) ‘Structural insight into iodide uptake by AFm phases’, *Environmental Science and Technology*, 46, pp. 3874–3881.

AIMOZ, L., KULIK, D. A., WIELAND, E., CURTI, E., LOTHENBACH, B. AND MÄDER, U. (2012) ‘Thermodynamics of AFm-(I 2, SO 4) solid solution and of its end-members in aqueous media’, *Applied Geochemistry*, 27, pp. 2117–2129.

AITCHISON, I. AND DAVIES, P. H. (1993) ‘Role of microsegregation in fracture of cold-worked Zr-2.5Nb pressure tubes’, *Journal of Nuclear Materials*, 203, pp. 206–220.

BAILLY, H., MÉNESSIER, D. AND PRUNIER, C. (1999) *The nuclear fuel of pressurized water reactors and fast reactors: design and behaviour*. Paris: Lavoisier Publishing.

BALL, R. G. J., BURNS, W. G., HENSHAW, J., MIGNANELLI, M. A. AND POTTER, P. E. (1989) ‘The chemical constitution of the fuel-clad gap in oxide fuel pins for nuclear reactors’, *Journal of Nuclear Materials*, 167, pp. 191–204.

BENCZE, J. (2017) *Interim Storage of Spent Nuclear Fuel in Paks MVDS Facility*. Paks,

Hungary.

BGR (2007) *Endlagerung radioaktiver Abfälle in Deutschland - Untersuchung und Bewertung von Regionen mit potenziell geeigneten Wirtsgesteinsformationen*, Bundesgesellschaft für Geowissenschaften und Rohstoffe. Hannover / Berlin, Germany.

BOHE, A. E., ANDRADE GAMBOA, J. J., LOPASSO, E. M. AND PASQUEVICH, D. M. (1996) 'Zirconium recovery from zircaloy shavings', *Journal of Materials Science*, 31, pp. 3469–3474.

BONANO, E. J., KALININA, E. A. AND SWIFT, P. N. (2018) 'The Need for Integrating the Back End of the Nuclear Fuel Cycle in the United States of America', *MRS Advances*, 3, pp. 991–1003.

BROWN, F. J., PALMER, J. D. AND WOOD, P. (1999) 'Derivation of a radionuclide inventory for irradiated graphite-chlorine-36 Inventory determination', in *Proceedings of IAEA Technical Committee Meeting*. Manchester, UK, pp. 143–152.

BRUNO, J. AND EWING, R. C. (2006) 'Spent nuclear fuel', *Elements*, 2, pp. 343–349.

BUCK, E. C., MAUSOLF, E. J., MCNAMARA, B. K., SODERQUIST, C. Z. AND SCHWANTES, J. M. (2015) 'Nanostructure of metallic particles in light water reactor used nuclear fuel', *Journal of Nuclear Materials*, 461, pp. 236–243.

BUNDESGESETZBLATT (2011) *Dreizehntes Gesetz zur Änderung des Atomgesetzes*. Available at: <http://www.bgbl.de>.

BURNS, W. G., CORDFUNKE, E. H. F., JOHNSON, P. A. V., POTTER, P. E., PRINS, G. AND RAND, M. H. (1985) 'Chemistry of the fuel-clad gap of a PWR rod', in *Fuel Rod Internal Chemistry and Fission Products Behaviour*. Karlsruhe, Germany, pp. 35–42.

BUSBY, C. C., TUCKER, R. P. AND MCCAULEY, J. E. (1975) 'Halogen stress corrosion cracking of zircaloy-4 tubing', *Journal of Nuclear Materials*, 55, pp. 64–82.

## References

---

BYTWERK, D. AND HIGLEY, K. (2009) 'Cl-36 transfer to ryegrass and consequences for environmental modeling', *Radioprotection*, 44, pp. 695–699.

CARUSO, S. (2016) 'Estimation of the radionuclide inventory in LWR spent fuel assembly structural materials for long-term safety analysis', *EPJ Nuclear Sciences & Technologies*, 2.

CASSETTE, P., CHARTIER, F., ISNARD, H., FRÉCHOU, C., LASZAK, I., DEGROS, J. P., BÉ, M. M., LÉPY, M. C. AND TARTES, I. (2010) 'Determination of  $^{93}\text{Zr}$  decay scheme and half-life', *Applied Radiation and Isotopes*, 68, pp. 122–130.

CATLOW, S. A., TROYER, G. L., HANSEN, D. R. AND JONES, R. A. (2005) 'Half-life measurement of  $^{126}\text{Sn}$  isolated from Hanford nuclear defense waste', *Journal of Radioanalytical and Nuclear Chemistry*, 263, pp. 599–603.

CHADWICK, M. B., HERMAN, M., OBLOŽINSKÝ, P., DUNN, M. E., DANON, Y., YOUNG, P. G., *ET AL.* (2011) 'ENDF/B-VII.1 nuclear data for science and technology: Cross sections, covariances, fission product yields and decay data', *Nuclear Data Sheets*, 112, pp. 2887–2996.

CHOUBEY, R. AND PULS, M. P. (1994) 'Crack initiation at long radial hydrides in Zr-2.5nb pressure tube material at elevated temperatures', *Metallurgical and Materials Transactions A*, 25, pp. 993–1004.

CHU, H. C., WU, S. K., CHIEN, K. F. AND KUO, R. C. (2007) 'Effect of radial hydrides on the axial and hoop mechanical properties of Zircaloy-4 cladding', *Journal of Nuclear Materials*, 362, pp. 93–103.

CISZAK, C., MERMOUX, M., MIRO, S., GUTIERREZ, G., LEPRETRE, F., POPA, I., HANIFI, K., ZACHARIE-AUBRUN, I., FAYETTE, L. AND CHEVALIER, S. (2017) 'Micro-Raman analysis of the fuel-cladding interface in a high burnup PWR fuel rod', *Journal of Nuclear Materials*, 495, pp. 392–404.

- CISZAK, C., DESGRANGES, L., GARCIA, P., SABATHIER, C., FAYETTE, L. AND CHEVALIER, S. (2019) 'On the origins and the evolution of the fuel-cladding bonding phenomenon in PWR fuel rods', *Journal of Nuclear Materials*, 520, pp. 110–120.
- CLARENS, F., GIMÉNEZ, J., DE PABLO, J., CASAS, I., ROVIRA, M., DIES, J., QUIÑONES, J. AND MARTÍNEZ-ESPARZA, A. (2005) 'Influence of  $\beta$  radiation on UO<sub>2</sub> dissolution at different pH values', *Radiochimica Acta*, 93, pp. 533–538.
- CLARK, R. A., CONROY, M. A., LACH, T. G., BUCK, E. C., PELLEGRINI, K. L., MCNAMARA, B. K. AND SCHWANTES, J. M. (2020) 'Distribution of metallic fission-product particles in the cladding liner of spent nuclear fuel', *npj Materials Degradation*, 4, pp. 1–9.
- COLEMAN, C. AND AMBLER, J. (1977) 'Susceptibility of Zirconium Alloys to Delayed Hydrogen Cracking', in *Zirconium in the Nuclear Industry, ASTM STP 633*. United States, pp. 589–607.
- COLLE, C., KASHPAROV, V., ZVARICH, S., YOSCHENKO, V., LEVCHUK, S. AND LUNDIN, S. (2005) 'Fate of long-lived radioactive halogens, (<sup>36</sup>Cl, <sup>129</sup>I), in agricultural ecosystems: Field investigations', *Radioprotection*, 40, pp. 329–334.
- COX, B. (1990) 'Pellet-clad interaction (PCI) failures of zirconium alloy fuel cladding - A review', *Journal of Nuclear Materials*, 172, pp. 249–292.
- CUBICCIOTTI, D. AND DAVIES, J. H. (1976) 'The Release of Iodine from Iodide Salts by Gamma Radiolysis', *Nuclear Science and Engineering*, 60, pp. 314–319.
- CUBICCIOTTI, D. AND SANECKI, J. E. (1978) 'Characterization of deposits on inside surfaces of LWR cladding', *Journal of Nuclear Materials*, 78, pp. 96–111.
- CUI, D., LOW, J., RONDINELLA, V. V. AND SPAHIU, K. (2010) 'Hydrogen catalytic effects of nanostructured alloy particles in spent fuel on radionuclide immobilization', *Applied Catalysis B: Environmental*, 94, pp. 173–178.

## References

---

CUI, D., LOW, J. AND SPAHIU, K. (2011) 'Environmental behaviors of spent nuclear fuel and canister materials', *Energy Environ. Sci.*, 4, pp. 2537–2545.

DANNHÄUSER, G., ATRENS, A. AND BÄRO, G. (1984) 'Stress-corrosion cracking of Zircaloy-4 cladding tubes Part 2. Cs/Cd mixtures and fractography', *Journal of Nuclear Materials*, 126, pp. 103–110.

DAUM, R. S., MAJUMDAR, S., LIU, Y. AND BILLONE, M. C. (2006) 'Radial-hydride Embrittlement of High-burnup Zircaloy-4 Fuel Cladding', *Journal of Nuclear Science and Technology*, 43, pp. 1054–1067.

DEGUELDRE, C., BERTSCH, J. AND MARTIN, M. (2016) 'Post irradiation examination of nuclear fuel: Toward a complete analysis', *Progress in Nuclear Energy*, 92, pp. 242–253.

DEWAYNE CECIL, L. AND VOGT, S. (1997) 'Identification of bomb-produced chlorine-36 in mid-latitude glacial ice of North America', *Nuclear Instruments and Methods in Physics Research, Section B: Beam Interactions with Materials and Atoms*, 123, pp. 287–289.

DROSTE, B. AND KOWALEWSKY, H. (1987) 'Sicherheit bei der Gefahrgutlagerung - Die sicherheitstechnische Begutachtung von Transportbehältern zur trockenen Zwischenlagerung abgebrannter Brennelemente', *Technische Überwachung*, pp. 3–8. Available at: <http://www.bvg.de/index.php/de/125316/name/Sicherheit+bei+der+U-Bahn.html>.

ELLINGER, A., GEUPEL, S., GEWEHR, K., GMAL, B., HANNSTEIN, V., HUMMELSHEIM, K., KILGER, R., WAGNER, M., SCHMIDT, G. AND SPIETH-ACHTNICH, A. (2010) *GRS-A-3597: Sicherheitstechnische Aspekte der langfristigen Zwischenlagerung von bestrahlten Brennelementen und verglastem HAW*.

ESK (2015) *Diskussionspapier zur verlängerten Zwischenlagerung bestrahlter Brennelemente und sonstiger Wärme entwickelnder radioaktiver Abfälle*. Bonn,

Germany.

EUROPEAN UNION (2011) *Radioactive waste and spent fuel management directive - L 199/48, Official Journal of the European Union.*

EVANS, J. C., LEPEL, E. L., SANDERS, R. W., WILKERSON, C. L., SILKER, W., THOMAS, C. W., ABEL, K. H. AND ROBERTSON, D. R. (1984) *Long-lived activation products in reactor materials, Nureg/Cr-3474.* Richland, USA.

EWING, R. C. (2008) 'Nuclear fuel cycle: Environmental impact', *MRS Bulletin*, 33, pp. 338–340.

EWING, R. C. (2015) 'Long-term storage of spent nuclear fuel', *Nature Materials*, 14, pp. 252–257.

EWING, R. C., WEBER, W. J. AND CLINARD, F. W. (1995) 'Radiation effects in nuclear waste forms for high-level radioactive waste', *Progress in Nuclear Energy*, 29, pp. 63–127.

FANGHÄNEL, T., RONDINELLA, V. V., GLATZ, J. P., WISS, T., WEGEN, D. H., GOUDER, T., CARBOL, P., SERRANO-PURROY, D. AND PAPAIOANNOU, D. (2013) 'Reducing uncertainties affecting the assessment of the long-term corrosion behavior of spent nuclear fuel', *Inorganic Chemistry*, 52, pp. 3491–3509.

FEE, D. C. AND JOHNSON, C. E. (1981) 'Fuel-cladding chemical interaction in uranium-plutonium oxide fast reactor fuel pins', *Journal of Nuclear Materials*, 96, pp. 80–104.

GECKEIS, H., DEGERING, D., GOERTZEN, A., GEYER, F. W. AND DRESSLER, P. (1995) *FZKA 5650: Langzeitsicherheit nuklearer Endlager - Radiochemische Analytik von Proben aus Brennstoffauslaugungsexperimenten.* Karlsruhe, Germany.

GECKEIS, H., METZ, V., GONZÁLEZ-ROBLES, E., LOIDA, A., BUBE, C. AND KIENZLER, B. (2012) 'Radionuclide behaviour in the near-field of a geological repository for spent

## References

---

nuclear fuel', *Radiochimica Acta*, 100, pp. 699–713.

GIBS, V., DIENST, W. AND GÖTZMANN, O. (1982) 'Kriechverhalten von Cr-Ni-Stahl unter Halogen- und Chalkogen-Einwirkung bei hohen Temperaturen', *Werkstoffe und Korrosion*, 33, pp. 533–541.

GILBERT, E. R., CUNNINGHAM, M. E., SIMONEN, E. P., ALLEMANN, R. T., LEVY, S. AND HAZELTON, R. F. (1987) *Control of Degradation of Spent LWR Fuel During Dry Storage in an Inert Atmosphere*. Richland, USA.

GOLL, W., SCHLEMMER, F., DEWES, P., FISCHER, G., PORSCH, D., SONTHEIMER, F. AND WÜRTZ, R. (1988) *Abschlussbericht Förderungsvorhaben BMFT AtT 7685/8: Qualifikation von leicht löslichem Mischoxid-Brennstoff*. Erlangen, Germany.

GONZÁLEZ-ROBLES, E., METZ, V., WEGEN, D. H., HERM, M., PAPAIOANNOU, D., BOHNERT, E., GREYTER, R., MÜLLER, N., NASYROW, R., DE WEERD, W., WISS, T. AND KIENZLER, B. (2016) 'Determination of fission gas release of spent nuclear fuel in puncturing test and in leaching experiments under anoxic conditions', *Journal of Nuclear Materials*, 479, pp. 67–75.

GONZÁLEZ-ROBLES, E., HERM, M., MÜLLER, N., BOHNERT, E. AND METZ, V. (2018) 'Description of leaching experiments with KIT's MOX irradiated fuel', in *1st Annual Meeting Proceedings of the Collaborative Project 'Modern Spent Fuel Dissolution and Chemistry in Failed Container Conditions'*, pp. 29–32.

GÖTZMANN, O. (1979) 'A thermodynamic model for the attack behaviour in stainless steel clad oxide fuel pins', *Journal of Nuclear Materials*, 84, pp. 39–54.

GÖTZMANN, O. (1982a) 'Die Bedeutung der Brennstoff-Verunreinigungen für das Brennstabverhalten', *Journal of Nuclear Materials*, 53, pp. 301–308.

GÖTZMANN, O. (1982b) 'Thermochemical evaluation of PCI failures in LWR fuel pins',

*Journal of Nuclear Materials*, 107, pp. 185–195.

GÖTZMANN, O. AND HEUVEL, H. J. (1979) ‘Einfluss von Verunreinigungen auf die Hüllinnenkorrosion von stahlumhüllten oxidischen Brennstäben’, *Journal of Nuclear Materials*, 81, pp. 231–219.

GÖTZMANN, O., HOFMANN, P. AND THÜMMLER, F. (1974) ‘Attack upon the cladding of oxide fuel pins by fuel and fission products’, *Journal of Nuclear Materials*, 52, pp. 33–50.

GRAMBOW, B., LOIDA, A., DRESSLER, P., GECKEIS, H., GAGO, J., CASAS, I., DE PABLO, J., GIMÉNEZ, J. AND TORRERO, M. E. (1996) *FZKA 5702: Long-Term Safety of Radioactive Waste Disposal: Chemical Reaction of Fabricated and High Burnup Spent UO<sub>2</sub> Fuel with Saline Brines*. Karlsruhe, Germany.

GRAMBOW, B., LOIDA, A., MARTINEZ-ESPARZA, A., DIAZ-AROCAS, P., DE PABLO, J., PAUL, J.-L., MARX, G., GLATZ, J. P., LEMMENS, K., OLLILA, K. AND CHRISTENSEN, H. (2000) *FZKA 6420: Long-Term Safety of Radioactive Waste Disposal: Source Term for Performance Assessment of Spent Fuel as a Waste Form*. Karlsruhe, Germany.

GRAMBOW, B. (2008) ‘Mobile fission and activation products in nuclear waste disposal’, *Journal of Contaminant Hydrology*, 102, pp. 180–186.

GRAMBOW, B., FERRY, C., CASAS, I., BRUNO, J., QUINONES, J. AND JOHNSON, L. (2011) ‘Spent fuel waste disposal: Analyses of model uncertainty in the MICADO project’, *Energy Procedia*, 7, pp. 487–494.

GUENTHER, R. J., BLAHNIK, D. E., CAMPBELL, T. K., JENQUIN, U. P., MENDEL, J. E. AND THORNHILL, C. K. (1988) *Characterization of Spent Fuel Approved Testing Material-ATM-106*. Richland, USA.

HÄKKINEN, S. (2019) *Impurities in LWR fuel and structural materials*. VTT, Finland.

## References

---

HE, M., KEECH, P. G., BROCKOWSKI, M. E., NOËL, J. J. AND SHOESMITH, D. W. (2007) 'Characterization of the influence of fission product doping on the anodic reactivity of uranium dioxide', *Canadian Journal of Chemistry*, 85, pp. 702–713.

HERM, M. (2015) *Study on the effect of speciation on radionuclide mobilization – C-14 speciation in irradiated Zircaloy-4 cladding and nitrate / chloride interaction with An (III)/Ln (III)*. Karlsruhe Institute of Technology.

HERM, M., DAGAN, R., GONZÁLEZ-ROBLES, E., MÜLLER, N. AND METZ, V. (2018) 'Comparison of calculated and measured radionuclide inventory of a Zircaloy-4 cladding tube plenum section', *MRS Advances*, 3, pp. 1031–1037.

HERM, M. (2021) *Personal communication*.

HOFMANN, P. AND SPINO, J. (1983) 'Chemical aspects of iodine-induced stress corrosion cracking failure of zircaloy-4 tubing above 500°C', *Journal of Nuclear Materials*, 114, pp. 50–65.

HOFMANN, P. AND SPINO, J. (1985) 'Conditions under which CsI can cause SCC failure of Zircaloy tubing', 127, pp. 205–220.

HOLLECK, H. AND KLEYKAMP, H. (1970) *KFK 1181: Zur Stöchiometrieverschiebung in einem oxidischen Brennelement bei hohem Abbrand*. Karlsruhe, Germany.

HOU, X. (2018) 'Liquid scintillation counting for determination of radionuclides in environmental and nuclear application', *Journal of Radioanalytical and Nuclear Chemistry*, 318, pp. 1597–1628.

HOU, X., ØSTERGAARD, L. F. AND NIELSEN, S. P. (2007) 'Determination of <sup>36</sup>Cl in nuclear waste from reactor decommissioning', *Analytical Chemistry*, 79, pp. 3126–3134.

HUMMEL, W. (2017) *Chemistry of selected dose-relevant radionuclides, NAGRA Technical Report 17-05*. Villingen, Switzerland.

HWU, S., VON WINBUSH, S., ZIEBARTH, R. P., FORD, J. E. AND CORBETT, J. D. (1986) 'Synthesis and Structure of Double-Metal-Layered Scandium, Yttrium, and Zirconium', *Inorganic Chemistry*, pp. 283–287.

IAEA (1998) *Durability of spent nuclear fuels and facility components in wet storage*, IAEA-TECDOC-1012.

IAEA (1999) *Survey of wet and dry spent fuel storage*, IAEA-TECDOC-1100.

IAEA (2003) *Spent fuel performance assessment and research*, IAEA-TECDOC-1343.

IAEA (2012) *Spent Fuel Performance Assessment and Research - Final Report of a Coordinated Research Project (SPAR-II)*. Available at: [http://www-pub.iaea.org/MTCD/Publications/PDF/TE\\_1680\\_web.pdf](http://www-pub.iaea.org/MTCD/Publications/PDF/TE_1680_web.pdf).

IAEA (2014) *Behaviour of Spent Power Reactor Fuel during Storage, Extracts from the final reports of coordinated research projects on behaviour of spent assemblies in storage (BEFAST I-III) and spent fuel performance assessment and research (SPAR 1-111) - 1981-2019*. Available at: <http://www-ns.iaea.org/standards/>.

IAEA (2018) *Status and Trends in Spent Fuel and Radioactive Waste Management*, IAEA Nuclear Energy Series No. NW-T-1.14.

IBPT (2016) *The KIT institute for Beam Physics and Technology*. Available online: [www.ibpt.kit.edu/](http://www.ibpt.kit.edu/).

JEGOU, C., GENNISSON, M., PEUGET, S., DESGRANGES, L., GUIMBRETIERE, G., MAGNIN, M., TALIP, Z. AND SIMON, P. (2015) 'Raman micro-spectroscopy of UO<sub>x</sub> and MOX spent nuclear fuel characterization and oxidation resistance of the high burn-up structure', *Journal of Nuclear Materials*, 458, pp. 343–349.

JOHNSON, L., POINSSOT, C., FERRY, C. AND LOVERA, P. (2004) *Estimates of the Instant Release Fraction for UO<sub>2</sub> and MOX Fuel at t=0*, NAGRA Technical Report 04-08.

## References

---

Wettingen, Switzerland.

JOHNSON, L. H. AND TAIT, J. C. (1997) *Release of segregated nuclides from spent fuel*, SKB Technical Report 97-18. Pinawa, Canada.

JÖRG, G., BÜHNEMANN, R., HOLLAS, S., KIVEL, N., KOSSERT, K., VAN WINCKEL, S. AND GOSTOMSKI, C. L. V. (2010) 'Preparation of radiochemically pure  $^{79}\text{Se}$  and highly precise determination of its half-life', *Applied Radiation and Isotopes*, 68, pp. 2339–2351.

KADANO, K., KINUGAWA, K. AND TANAKA, H. (1994) 'X-ray photoelectron spectroscopy of  $\text{ZnCl}_2$  based glasses', *Physics and Chemistry of Glasses*, 35, pp. 59–64.

KAUFMANN, R. (1988) *Oberflächenanalytische Untersuchungen zum thermischen Verhalten von passivierten Zircaloy-4 Oberflächen und Reaktionsverhalten von Iod an Zircaloy-4 Oberflächen*. Technische Hochschule Karlsruhe.

KERNKRAFTWERK GÖSGEN (2010) *Technik und Betrieb - Technische Hauptdaten*.

KIM, K. T. (2010) 'UO<sub>2</sub>/Zry-4 chemical interaction layers for intact and leak PWR fuel rods', *Journal of Nuclear Materials*, 404, pp. 128–137.

KLEYKAMP, H. (1979) 'The chemical state of LWR high-power rods under irradiation', *Journal of Nuclear Materials*, 84, pp. 23–25.

KLEYKAMP, H., PASCHOAL, J., PEJSA, R. AND THOMMLER, F. (1985) 'Composition and structure of fission product precipitates in irradiated oxide fuels', *Journal of Nuclear Materials*, 130, pp. 426–433.

KLEYKAMP, H. (1985) 'The chemical state of the fission products in oxide fuels', *Journal of Nuclear Materials*, 131, pp. 221–246.

KLEYKAMP, H. (1989) 'Constitution and thermodynamics of the Mo-Ru, Mo-Pd, Ru-Pd and Mo-Ru-Pd systems', *Journal of Nuclear Materials*, 167, pp. 49–63.

- KLEYKAMP, H. (2004) 'Post-irradiation studies on LWR-MOX fuel fabricated by the optimized co-milling process', *Journal of Nuclear Materials*, 324, pp. 198–202.
- KNAAB, H., GARTNER, M. AND SONTHEIMER, F. (1987) 'KWU's Experimental Basis for Power Ramping and Cycling Performance of LWR Fuel', in *Proceedings of the IAEA Meeting on Pellet-Cladding Interaction and Load-following Behaviour of Water Reactor Fuel*. Lyon, France.
- KONASHI, K., YATO, T. AND KANEKO, H. (1983) 'Radiation effect on partial pressure of fission product iodine', *Journal of Nuclear Materials*, 116, pp. 86–93.
- KONINGS, R. J. M., WISS, T. AND BENEŠ, O. (2015) 'Predicting material release during a nuclear reactor accident', *Nature Materials*, 14, pp. 247–252.
- LOIDA, A., GRAMBOW, B., KARSTEN, G. AND DRESSLER, P. (1997) 'Radionuclide Release From Spent MOX Fuel', *MRS Online Proceedings Library*, 506, pp. 923–924.
- LYSELL, C. AND SCHRIRE, D. (1990) 'Fission Product Distribution at Different Power Levels', in *Proceedings of the IAEA Technical Committee Meeting on Fuel Performance at High Burnup for Water Reactors*. Nyköping, Sweden.
- MAGILL, J., DREHER, R. AND SÓTI, Z. (2018) *Chart of the Nuclides 10th edition*. Karlsruhe, Germany: JRC-Karlsruhe.
- MARTIN, J. E., MARCINOWSKI, F. AND COOK, S. K. (1990) 'Optimization of neutron activation analyses of <sup>129</sup>I in low-level radioactive waste samples', *International Journal of Radiation Applications and Instrumentation. Part A*, 41, pp. 727–731.
- MATZKE, H. (1995) 'Oxygen potential measurements in high burnup LWR UO<sub>2</sub> fuel', *Journal of Nuclear Materials*, 223, pp. 1–5.
- McFARLANE, J. (1996) 'Fission Product Tellurium Chemistry from Fuel to Containment', in *Proceedings on the OECD CSNI Workshop on the Chemistry of Iodine in Reactor*

## References

---

*Safety*. Würenlingen, Switzerland, pp. 563–585.

METZ, V., GONZÁLEZ-ROBLES, E., MÜLLER, N., BOHNERT, E., HERM, M., LAGOS, M., KIENZLER, B., SERRANO-PURROY, D., COLLE, J. Y., BENEŠ, O., NAISSE, F., WISS, T., KONINGS, R. J. M., WEGEN, D. H., PAPAIOANNOU, D., GREYTER, R., NASYROW, R., RONDINELLA, V. V., GLATZ, J.-P., CURTIUS, H., MÜSKES, H. W., LIKE, N., BOSBACH, D., GÜNTHER-LEOPOLD, I., CURTI, E., ZUMBIEHL, A. F., LINDER, H. P., GOVERS, K., VERWERFT, M., VAN RENTERGHEM, W., LEMMENS, K., MENNECART, T., CACHOIR, C., ADRIAENSEN, L., DOBNEY, A., GYSEMANS, M., VANDENBORRE, J., TRABOULSI, A., BLAIN, G., BARBET, J., FATTAHI, M., PASTOR, R. S., SLONSKI, E., HÓZER, Z. AND ROTH, O. (2013) *Characterisation of spent nuclear fuel samples and description of methodologies and tools to be applied in FIRST-Nuclides*.

NEEB, K.-H. (1997) *The Radiochemistry of Nuclear Power Plants with Light Water Reactors*. Berlin: Walter de Gruyter.

NICHOLS, A. L., ALDAMA, D. L. AND VERPELLI, M. (2008) *Handbook of Nuclear Data for Safeguards: Database Extensions*. Vienna: IAEA.

NIKULINA, A. V. AND MALGIN, A. G. (2008) ‘Impurities and their effect on the structure and properties of zirconium parts in nuclear reactors’, *Atomic Energy*, 105, pp. 328–339.

NUCLEONICA GMBH (2011) *Nucleonica Nuclear Science Portal (www.nucleonica.com)*, Version 3.0.11.KORIGEN code, <http://www.nucleonica.net/Application/Korigen.aspx>.

OECD-NEA (2006) *Advanced Nuclear Fuel Cycles and Radioactive Waste Management*. Paris: OECD Publishing.

OHSE, R. W. AND SCHECHTER, M. (1972) *The Role of Caesium in Chemical Interaction of Austenitic Stainless Steels with Uranium Plutonium Oxide Fuels*, EUR 4893 e. Karlsruhe, Germany.

OLANDER, D. (2009) 'Nuclear fuels - Present and future', *Journal of Nuclear Materials*, 389, pp. 1–22.

OLANDER, D. R. (1982) 'Chemical aspects of pellet-cladding interaction in light-water-reactor fuel elements', *Transactions of the American Nuclear Society*, 41, pp. 270–271.

PAN, Z., WANG, N. AND HE, Z. (2010) 'Measurements of elastic modulus in Zr alloys for CANDU applications', in *11th International Conference on CANDU fuel*, pp. 17–20. Available at: [http://www.media.cns-snc.ca/uploads/event\\_data/candu\\_fuel\\_2010/proceedings\\_updates/Measurements\\_of\\_elastic\\_modulus\\_in\\_Zr\\_alloys\\_for\\_CANDU\\_applications\\_-\\_Pan.pdf](http://www.media.cns-snc.ca/uploads/event_data/candu_fuel_2010/proceedings_updates/Measurements_of_elastic_modulus_in_Zr_alloys_for_CANDU_applications_-_Pan.pdf).

PARK, S. Y., KIM, J. H., CHOI, B. K. AND JEONG, Y. H. (2007) 'Crack initiation and propagation behavior of zirconium cladding under an environment of iodine-induced stress corrosion', *Metals and Materials International*, 13, pp. 155–163.

PEEHS, M., MANZEL, R., SCHWEIGHOFER, W., HAAS, W., HAAS, E. AND WÜRTZ, R. (1981) 'On the behaviour of cesium and iodine in light water reactor fuel rods', *Journal of Nuclear Materials*, 97, pp. 157–164.

PELLEGRINI, K. L., SODERQUIST, C. Z., SHEN, S. D., KROGSTAD, E. J., PALMER, C. J., GERREZ, K. R., BUCK, E. C., LACH, T. G., SCHWANTES, J. M. AND CLARK, R. A. (2019) 'Chemical and Isotopic Characterization of Noble Metal Phase from Commercial UO<sub>2</sub> Fuel', *Analytical chemistry*, 91, pp. 6522–6529.

PELOWITZ, D., GOORLEY, T., JAMES, M., BOOTH, T., BROWN, F., BULL, J., COX, L., DURKEE, J., ELSON, J., FENSIN, M., FORSTER, R., HENDRICKS, J., HUGHES, H., JOHNS, R., KIEDROWSKI, B., MARTZ, R., MASHNIK, S., MCKINNEY, G., PRAEL, R. AND ZUKAITIS, T. (2013) *MCNP6 User's Manual. Version 1.0* Los Alamos National Laboratories LA-CP-13-00634. Los Alamos National Laboratory.

PIPON, Y., TOULHOAT, N., MONCOFFRE, N., JAFFRÉZIC, H., GAVARINI, S., MARTIN, P.,

## References

---

RAIMBAULT, L. AND SCHEIDEGGER, A. M. (2006) 'Thermal diffusion of chlorine in uranium dioxide', *Radiochimica Acta*, 94, pp. 705–711.

PLATTE, T., FINCK, N., MANGOLD, S., POLLY, R. AND GECKEIS, H. (2021) 'Retention of Iodide and Chloride by Formation of a Green Rust Solid Solution GR-C11- xIx: A Multiscale Approach', *Inorganic Chemistry*, 60, pp. 10585–10595.

POINSSOT, C., TOULHOAT, P., GRAS, J. M. AND VITORGE, P. (2002) 'Long term evolution of spent nuclear fuel in long term storage or geological disposal. New findings from the French PRECCI RandD program and implications for the definition of the RN source term in geological repository', *Journal of Nuclear Science and Technology*, 39, pp. 473–476.

POINSSOT, C., FERRY, C., KELM, M., GRAMBOW, B., MARTÍNEZ, A., JOHNSON, L., ANDRIAMBOLOLONA, Z., BRUNO, J., CACHOIR, C., CAVEDON, J. M., CHRISTENSEN, H., CORBEL, C., JEGOU, C., LEMMENS, K., LOIDA, A., LOVERA, P., MISERQUE, F., DE PABLO, J., A., P., QUIÑONES, J., RONDINELLA, V., SPAHIU, K. AND WEGEN, D. H. (2004) *Spent Fuel Stability Under Repository Conditions, Final Report of the EC 5th Framework Program SFS*.

POINTEAU, I., COREAU, N. AND REILLER, P. E. (2008) 'Uptake of anionic radionuclides onto degraded cement pastes and competing effect of organic ligands', *Radiochimica Acta*, 96, pp. 367–374.

PULHAM, R. J. AND RICHARDS, M. W. (1990) 'Chemical reactions of caesium, tellurium and oxygen with fast breeder reactor cladding alloys. Part IV - The corrosion of ferritic steels', *Journal of Nuclear Materials*, 172, pp. 304–313.

PULHAM, R. J., RICHARDS, M. W. AND KENNARD, D. R. (1995) 'Chemical reactions of Zircaloy-4 and zirconium with (i) dicaesium telluride, Cs<sub>2</sub>Te, (ii) caesium tellurite, Cs<sub>2</sub>TeO<sub>3</sub>, and (iii) tellurium, under different oxygen potentials', *Journal of Nuclear*

*Materials*, 223, pp. 277–285.

QIN, W., SZPUNAR, J. A. AND KOZINSKI, J. (2015) ‘Hydride-induced degradation of zirconium alloys: A criterion for complete ductile-to-brittle transition and its dependence on microstructure’, *Proceedings of the Royal Society A*, 471.

RAVEL, B. AND NEWVILLE, M. (2005) ‘ATHENA, ARTEMIS, HEPHAESTUS: data analysis for X-ray absorption spectroscopy IFEFFIT’, *Journal of Synchrotron Radiation*, 12, pp. 537–541.

REED, W. A., MAY, I., LIVENS, F. R., CHARNOCK, J. M., JEAPES, A. P., GRESLEY, M., MITCHELL, R. M. AND KNIGHT, P. (2002) ‘XANES fingerprinting of iodine species in solution and speciation of iodine in spent solvent from nuclear fuel reprocessing’, *Journal of Analytical Atomic Spectrometry*, 17, pp. 541–543.

REITHMEIER, H., LAZAREV, V., RÜHM, W., SCHWIKOWSKI, M., GÄGGELER, H. W. AND NOLTE, E. (2006) ‘Estimate of European<sup>129</sup>I releases supported by<sup>129</sup>I analysis in an alpine ice core’, *Environmental Science and Technology*, 40, pp. 5891–5896.

RIGBY, D. B. (2010) *Evaluation of the Technical Basis for Extended Dry Storage and Transportation of Used Nuclear Fuel*, United States Nuclear Waste Technical Review Board.

RILEY, B. J., VIENNA, J. D., STRACHAN, D. M., MCCLOY, J. S. AND JERDEN, J. L. (2016) ‘Materials and processes for the effective capture and immobilization of radioiodine: A review’, *Journal of Nuclear Materials*, 470, pp. 307–326.

RONDINELLA, V. V., FANGHÄNEL, T., GLATZ, J. P., WISS, T., WEGEN, D. H., GOUDER, T., CARBOL, P., SERRANO-PURROY, D. AND PAPAIOANNOU, D. (2013) ‘Reducing uncertainties affecting the assessment of the long-term corrosion behavior of spent nuclear fuel’, *Inorganic Chemistry*, 52, pp. 3491–3509.

## References

---

RONDINELLA, V. V. AND WISS, T. (2010) ‘The high burn-up structure in nuclear fuel’, *Materials Today*, 13, pp. 24–32.

ROTHE, J., ALTMAIER, M., DAGAN, R., DARDENNE, K., FELLHAUER, D., GAONA, X., CORRALES, E. G. R., HERM, M., KVASHNINA, K. O., METZ, V., PIDCHENKO, I., SCHILD, D., VITOVA, T. AND GECKEIS, H. (2019) ‘Fifteen years of radionuclide research at the KIT synchrotron source in the context of the nuclear waste disposal safety case’, *Geosciences (Switzerland)*, 9, pp. 1–22.

ROWOLD, F., HUMMELSHEIM, K. AND STUKE, M. (2018) ‘Open questions on the road to reliable predictions of cladding integrity’, *Kerntechnik*, 83, pp. 484–487.

RUDLING, P., STRASSER, A. AND GARZAROLLI, F. (2007) *Welding of Zirconium Alloys, Welding International*.

SCHNEIDER-EICKHOFF, R. (2021) ‘Forschungsaktivitäten der BGZ auf dem Gebiet Transport- und Lagerbehälter Forschungsaktivitäten der BGZ auf dem Gebiet Transport- und Lagerbehälter’, in *Fachworkshop Zwischenlagerung 2021*. Berlin, Germany.

SHEPPARD, S. C., JOHNSON, L. H., GOODWIN, B. W., TAIT, J. C., WUSCHKE, D. M. AND DAVISON, C. C. (1996) ‘Chlorine-36 in nuclear waste disposal-1. Assessment results for used fuel with comparison to  $^{129}\text{I}$  and  $^{14}\text{C}$ ’, *Waste Management*, 16, pp. 607–614.

SHIMADA, S., MATSUURA, T. AND NAGAI, M. (1983) ‘Stress corrosion cracking of zircaloy-2 by metal iodides’, *Journal of Nuclear Science and Technology*, 20, pp. 593–602.

SIDKY, P. S. (1998) ‘Iodine stress corrosion cracking of Zircaloy reactor cladding: Iodine chemistry (a review)’, *Journal of Nuclear Materials*, 256, pp. 1–17.

SKB (2006) *Long-term safety for KBS-3 repositories at Forsmark and Laxemar – a first evaluation: Main Report of the SR-Can project, Technical Report 06-09*. Stockholm,

Sweden.

SODERQUIST, C. AND HANSON, B. (2010) ‘Dissolution of spent nuclear fuel in carbonate-peroxide solution’, *Journal of Nuclear Materials*, 396, pp. 159–162.

SODERQUIST, C. Z., JOHNSEN, A. M., MCNAMARA, B. K., HANSON, B. D., CHENAULT, J. W., CARSON, K. J. AND PEPPER, S. M. (2011) ‘Dissolution of irradiated commercial UO<sub>2</sub> fuels in ammonium carbonate and hydrogen Peroxide’, *Industrial and Engineering Chemistry Research*, 50, pp. 1813–1818.

SOLÉ, V. A., PAPILLON, E., COTTE, M., WALTER, P. AND SUSINI, J. (2007) ‘A multiplatform code for the analysis of energy-dispersive X-ray fluorescence spectra’, *Spectrochimica Acta - Part B Atomic Spectroscopy*, 62, pp. 63–68.

SONNENBURG, H.-G. AND BOLDT, F. (2017) *Brennstabverhalten im Normalbetrieb, bei Störfällen und bei Langzeitlagerung*.

SPAHIU, K., EKEROTH, E., GRANFORS, M. AND SCHILD, D. (2020) ‘The effect of temperature and fuel surface area on spent nuclear fuel dissolution kinetics under H<sub>2</sub> atmosphere’, *Journal of Nuclear Materials*, 531, p. 151981.

SPYKMAN, G. (2018) ‘Dry storage of spent nuclear fuel and high active waste in Germany—Current situation and technical aspects on inventories integrity for a prolonged storage time’, *Nuclear Engineering and Technology*, 50, pp. 313–317.

STRATTON, W. R., BOTTA, F., HOFER, R., LEDERGERBER, G., INGOLD, F., OTT, C., REINDL, J., ZWICKY, H. U., BODMER, R. AND SCHLEMMER, F. (1991) ‘A comparative irradiation test of UO<sub>2</sub> sphere-pac and pellet fuel in the Goesgen PWR.’, in *Int. Topical Meeting on LWR Fuel Performance “Fuel for the 90’s”*. Avignon, France, pp. 174–183.

STUKE, M., BOLDT, F., KAUFHOLZ, P., PÉRIDIS, M. AND SONNENBURG, H. G. (2018) ‘Research activities at GRS on fuel rod behaviour during extended dry storage’,

## References

---

*Kerntechnik*, 83, pp. 476–483.

TAIT, J. C., CORNET, R. J. J., CHANT, L. A., JIROVEC, J., MCCONNELL, J. AND WILKIN, D. L. (1997) ‘Determination of Cl Impurities and 36 Cl Instant Release from Used Candu Fuels’, *MRS Proceedings*, 465, p. 503.

TAIT, J. C. AND THEAKER, J. R. (1996) *Light Element Radionuclides in Used Fuel and Their Potential Contribution to Postclosure Safety Assessment*, AECL-11431.

THEAKER, J. R., CHOUBEY, R., MOAN, G. D., ALDRIDGE, S. A., DAVIS, L., GRAHAM, R. A. AND COLEMAN, C. E. (1994) ‘Fabrication of Zr-2.5Nb Pressure Tubes to Minimise the Harmful Effects of Trace Elements’, in *Tenth International Symposium on Zirconium in the Nuclear Industry*. Baltimore, USA.

TOSCH, L. (2010) *Kontamination von Nord- und Ostsee mit langlebigem Iod-129 und anderen anthropogenen Radionukliden*. Gottfried Wilhelm Leibniz Universität Hannover.

VISWANATHAN, R. (2014) ‘Fuel clad chemical interactions in fast reactor MOX fuels’, *Journal of Nuclear Materials*, 444, pp. 101–111.

WALKER, C. T., BREMIER, S., PORTIER, S., HASNAOUI, R. AND GOLL, W. (2009) ‘SIMS analysis of an UO<sub>2</sub> fuel irradiated at low temperature to 65 MWd/kgHM’, *Journal of Nuclear Materials*, 393, pp. 212–223.

WIELAND, E. (2014) *Sorption Data Base for the Cementitious Near Field of L/ILW and ILW Repositories for Provisional Safety Analyses for SGT-E2*, NAGRA Technical Report 14-08. Villingen, Switzerland.

WILSON, W. B., COWELL, S. T., ENGLAND, T. R., HAYES, A. C. AND MOLLER, P. (2008) ‘“A Manual for CINDER’90 Version 07.4 Codes and Data” Los Alamos National Laboratory LA-UR-07-8412’.

WOLFF, D., VÖLZKE, H., WILLE, F. AND DROSTE, B. (2013) 'Extended Storage after Long-term Storage', in *Proceedings of the 17th International Symposium on the Packaging and Transportation of Radioactive Materials*. San Francisco, USA.

YAGGEE, F. L., MATTAS, R. F. AND NEIMARK, L. A. (1980) *Characterization of Irradiated Zircalloys: Susceptibility to Stress Corrosion Cracking, NP-1557*.

ZIEGLER, A. AND ALLELEIN, H.-J. (2013) *Reaktortechnik, Reaktortechnik*. Berlin: Springer Verlag.

